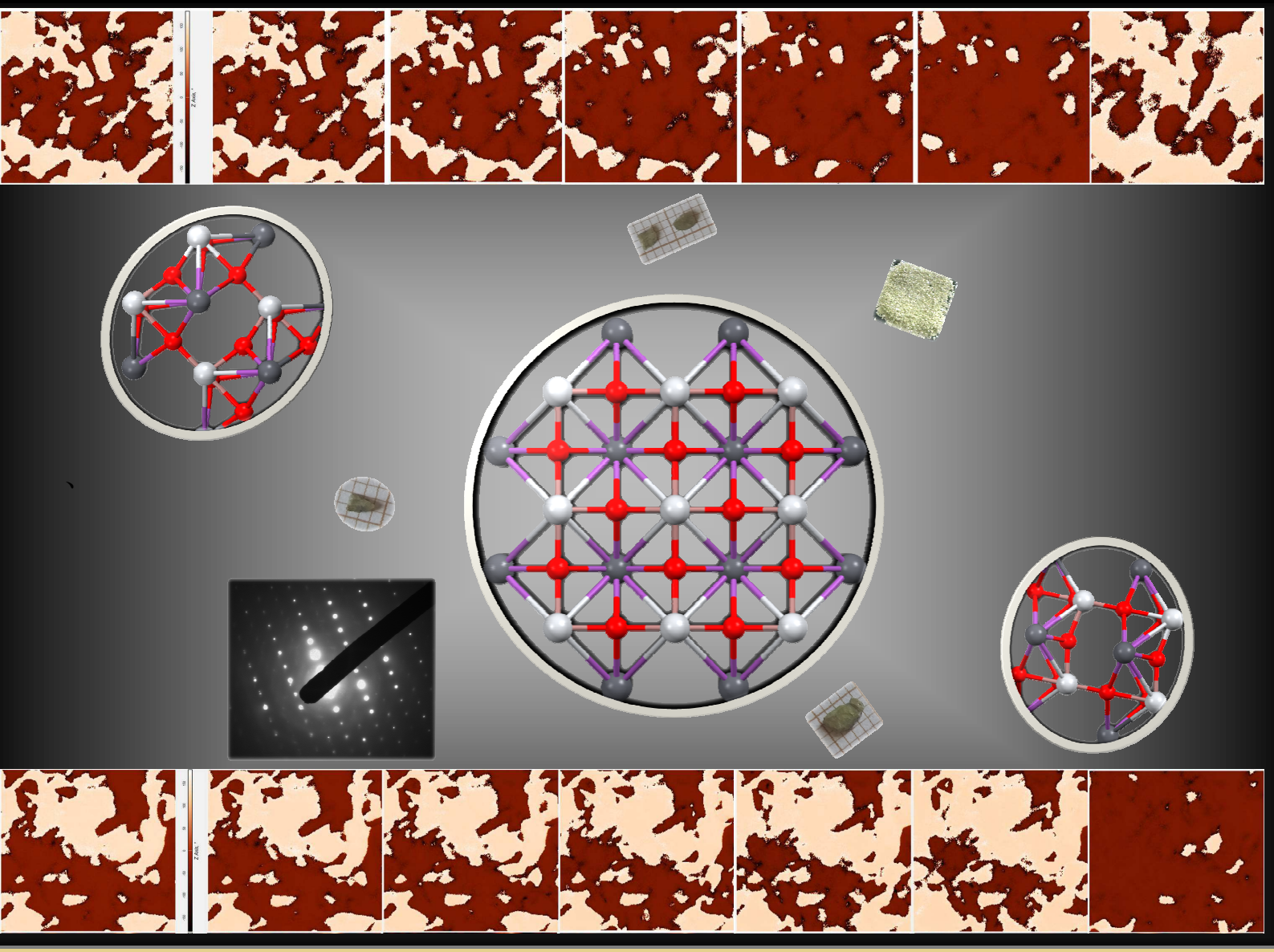

Lan Xu

Novel Ferroelectric Bi*Me*O_3-$PbTiO_3$ Single Crystals with a High Curie Temperature

PhD Thesis in Physics branch of Condensed Matter Physics, supervised by Doctor Jingzhong Xiao and Full Professor José António de Carvalho Paixão and submitted to the Faculty of Sciences and Technology of the University of Coimbra

January/2016

· U C ·

Universidade de Coimbra

University of Coimbra

Faculty of Science and Technology

Department of Physics

Novel Ferroelectric Bi*Me*O_3-$PbTiO_3$ Single Crystals with a High Curie Temperature

PhD Thesis in Physics branch of Condensed Matter Physics submitted to the Faculty of Sciences and Technology of the University of Coimbra

Supervisor:

Doctor Jingzhong Xiao

Full Professor José António de Carvalho Paixão

Lan Xu

2016.01

Acknowledgements

I would like to express my sincere gratitude to all those who helped me during the research and writing of this thesis.

Foremost, I would like to appreciate my supervisor Doctor Jingzhong Xiao for giving me the opportunity and support to challenge this research project. He taught me to be hopeful, patient and persistent towards my research.

My deep appreciation and high tribute should also go to my co-supervisor Professor José António de Carvalho Paixão. He patiently helped me to modify this thesis again and again and provided his instructive advice and useful suggestions. His extraordinary knowledge and responsibility are impressive.

I am grateful to both Professor Maria Margarida Ramalho Ribeiro da Costa and Associate Professor João Manuel de Sá Campos Gil for valuable suggestions of this thesis. Specifically, Professor Maria Margarida Ramalho Ribeiro da Costa kindly and patiently kept helping me in the academic life.

My thanks would go also to Doctor Vladimir Khomchenko for the instruction of PFM measurement, Assistant Professor Vítor Hugo Nunes Rodrigues for XRD measurement, Assistant Professor Manuela Ramos Marques da Silva, Doctor Pedro Sidónio Pereira da Silva, Master Marta Sofia da Costa Henriques and all the other tutors and teachers.

Finally, I would deeply thank my beloved parents with their unconditional love for supporting and encouraging me to do what I want to do.

This work was supported by the Portuguese Fundação para a Ciência e a Tecnologia (FCT) project of PTDC/FIS/116146/2009 and acknowledged to TAIL-UC facility funded under QREN-Mais Centro project ICT_2009_02_012_1890.

Abstract

This thesis presents an experimental research on the growth and the physical properties of high Curie temperature Bi*Me*O_3-$PbTiO_3$ single crystals, mainly focused on their structural features, thermodynamics, ferroelectric phase transition, morphology and microstructure, domain structure and local switching characteristics. The high Curie temperature perovskite materials are particularly suited for high temperature environments, including space exploration and automotive industry.

Tetragonal xBiInO$_3$-(1-x)PbTiO$_3$ (BIPT) single crystals were grown from a high-temperature self-flux solution in which Pb_3O_4 and Bi_2O_3 are utilized as a complex flux. Based on the Rietveld refinement of X-ray powder diffraction data, the relationship between their structure and ferroelectric and piezoelectric properties was analysed. The as-grown 0.3BiInO$_3$-0.7PbTiO$_3$ (BIPT03), 0.4BiInO$_3$-0.6PbTiO$_3$ (BIPT04) and 0.5BiInO$_3$-0.5PbTiO$_3$ (BIPT05) single crystals exhibit high Curie temperatures around 555 ^{o}C. The addition of Bi/In was shown to increase the Curie temperature (T_c) of the parent ferroelectric PbTiO$_3$ (490 ^{o}C).

The dielectric, ferroelectric and piezoelectric properties of BIPT single crystals were investigated. The ferroelectric-paraelectric phase transition in BIPT03 was studied using high-temperature X-ray diffraction (XRD) and differential scanning calorimetry (DSC). We have undertaken the XRD study at different temperatures to obtain direct structural information about the phase transition from the ferroelectric to the paraelectric phase. DSC was used to characterize the thermodynamics of this transition. A detailed study of the compound BIPT03 showed “temperature hysteresis”, implying that the transition is of first order, with a coexistence of paraelectric and ferroelectric phases in a range of temperatures.

Fourier Transform Infra-Red Spectroscopy (FTIR) was used to characterize the lattice vibrational modes (TiO and PbO modes). XRD and selective area electron diffraction (SAED) were employed to characterize the phase composition and crystal structure; scanning electron microscopy (SEM) was used to observe the morphology

of the grown crystals. The observed SAED images and XRD rocking curves indicated that the crystals had a good quality.

The static domain structures and local switching properties of relaxor ferroelectric BIPT04 single crystals at (010) crystal orientations and BIPT03 single crystals at (110) crystal orientations where studied using piezoresponse force microscopy (PFM). PFM domain imaging shows that the (010) face of BIPT04 single crystals and the (110) face of BIPT03 single crystals exhibit a labyrinth-like surface domain pattern. Phase and amplitude PFM imaging under different bias voltages were used to study the domain behavior under external polarization. It revealed that bias voltage can effectively control the domain orientation. Piezoresponse hysteresis loops on the (010) face of BIPT04 single crystals enabled to measure local domain switching characteristics, such as the coercive voltage. Comparing with after poling applying ±25 V on the (010) face of BIPT04 single crystals, the coercive voltage was found to be smaller before poling. For BIPT04 single crystals, the domain area grows and the coercive voltage reduces as the thickness of the (010) face decreases.

Tetragonal single crystals $0.3BiAlO_3$-$0.7PbTiO_3$ with Curie temperature of 466^oC were also successfully grown and characterized. However, the $0.2BiYbO_3$-$0.8PbTiO_3$ (BYPT) and $0.37Bi(Sc_{0.5}Yb_{0.5})O_3$-$0.63PbTiO_3$ (BSYPT) single crystals could not be obtained as pure samples. Other crystals were obtained during the work of this thesis including (Pb_xBi_{3-x}) (Ti_yYb_{5-y}) O_{12} single crystals that crystallize in the garnet structure with space group $Ia\bar{3}d$ and those of BSYPT with inclusions of an impurity phase.

Keywords: Single Crystal Growth; Perovskites; Ferroelectric materials; High Curie Temperature

Resumo

Nesta tese é apresentada a investigação experimental realizada tendo em vista o crescimento de cristais ferroeléctricos com elevada temperatura de Curie da família Bi*Me*O_3-$PbTiO_3$ e caraterização das suas propriedades físicas focada nas propriedades estruturais, termodinâmicas, estudo da transição de fase ferroeléctrica, morfologia e microestutura, estrutura de domínios e propriedades de inversão "switching". As perovesquites com alta temperatura de Curie são materiais particularmente indicados para aplicações em ambientes de temperatura elevada, tais como as aplicações aeronáuticas e na indústria automóvel.

Efetuámos o crescimento de monocristais tetragonais com a composição xBiInO$_3$-(1-x)PbTiO$_3$ usando o método de solução de auto-fluxo, onde os óxidos Pb_3O_4 and Bi_2O_3 serviram como um fluxo complexo. O refinamento de Rietveld dos dados de difração de RX em pó foi usado para relacionar a estrutura com as propriedades ferroeléctricas e piezoeléctricas. Os monocristaisobtidos e analisados tais como foram sintetizados, sem outros tratamentos, de 0.3BiInO$_3$-0.7PbTiO$_3$ (BIPT03), 0.4BiInO$_3$-0.6PbTiO$_3$ (BIPT04) e 0.5BiInO$_3$-0.5PbTiO$_3$ (BIPT05) possuem temperaturas de Curie próximas de 555 ^{o}C. Assim, a adição deBi/Inaumenta a temperatura de Curie do composto de base PbTiO$_3$ (T_c = 490 ^{o}C).

As propriedades dielétricas, ferro e piezoeléctricas dos monocristais BIPT foram investigadas. A transição de fase ferroeléctrica-paraeléctrica foi estudada no composto BIPT03 por difração de RX a alta temperatura e por calorimetria de varrimento diferencial (DSC). Os estudos de RX a temperatura variável permitiram obter informação sobre a transição estrutural associada à transição da fase ferroeléctrica para a paramagnética. A técnica DSC permitiu caracterizar termodinamicamente a transição.

Um estudo detalhado do composto BIPT03 mostrou a existência de histerese térmica, implicando que a transição de fase é de 1ª ordem, com coexistência das fases ferroeléctrica e paraeléctrica num intervalo de temperaturas.

Espectroscopia de Infravermelho por transformadas de Fourier (FTIR) foi usada para caracterizar os modos vabriacionais da rede (TiO e PbO). Difração de RX (XRD), espectroscopia de fluorescência de RX (XRF), espectroscopia de RX com análise dispersiva em energia (EDS) e difração de electrões em área selecionada (SAED) permitiram uma caracterização detalhada da estrutura e composição das fases. Microscopia electrónica de varrimento (SEM) foi usada para observar a morfologia dos cristais. As imagens de SAED e os perfis das reflexões de Bragg dos monocristais demonstram que estes são de boa qualidade.

As estruturas estáticas dos domínios e as propriedades de inversão ("switching") dos monocristaisBIPT04 com orientação (010) e dos cristais BIPT03 com orientação (110) foram estudadas por microscopia de força de piezorespostaatómica (PFM). A imagem dos domínios da face (010) dos cristais de BIPT04 e da face (110) dos cristais BIPT03 exibem um padrão de domínios "labiríntico". As imagens PFM em contraste de fase e de amplitude obtidas aplicando várias tensões de polarização permitiram estudar a evolução da estrutura de domínios em função da polarização externa. As curvas de histerese da piezoresposta da face (010) dos mocristais de BIPT04 permitiram medir as características de inversão da polarização espontânea como a tensão coerciva. Efetuando a comparação com a situação após a aplicação de uma tensão de "poling" de ±25 V na face (010) dos cristais de BIPT04, verificou-se que a tensão coerciva é menor depois do "poling". Para os cristais de BIPT04, verificou-se que os tamanho dos domínios aumenta e que a tensão coerciva diminui à medida que a espessura da face (010) é reduzida.

Cristais tetragonais de composição $0.3BiAlO_3$-$0.7PbTiO_3$ com temperatura de Curie de 466 ^oC foram crescidos com sucesso e caracterizados. Infelizmente, as tentativas para crescer cristais puros de $0.2BiYbO_3$-$0.8PbTiO_3$ (BYPT) e $0.37Bi(Sc_{0.5}Yb_{0.5})O_3$-$0.63PbTiO_3$ (BSYPT) não foram bem sucedidas. Outros cristais que foram obtidos no decurso da tese incluem $(Pb_xBi_{3-x})(Ti_yYb_{5-y})O_{12}$ que cristaliza numa estrutura de granada com grupo espacial $Ia\overline{3}d$ e também de BSYPT, este último com inclusões de uma fase de impureza.

Palavras Chave: crescimento de monocristais; perovesquites; materiais ferroeléctricos; materiais com temperatura de Curie elevada.

Contents

List of Figures

List of Tables

Chapter 1

Introduction

Scientific interest on ferroelectric materials research has considerably focused on the development of ABO_3-type perovskite ferro/piezoelectric materials with a high Curie temperature (T_c) and excellent dielectric, piezoelectric and mechanical properties, either in the form of ceramics, thin films or single crystals, making them candidates for applications in high temperature environments, including space exploration and automotive industry. Ferroelectric $Pb(Zn_{1/3}Nb_{2/3})O_3$-$PbTiO_3$ (PZNT) and $Pb(Mg_{1/3}Nb_{2/3})O_3$-$PbTiO_3$ (PMNT) crystals[1], have attracted extraordinary interest for their ultrahigh piezoelectric coefficients (d_{33} > 2500 pC/N) and electromechanical coupling factors (k_{33} > 90%), which make them considerably promising in electronic industries. However, one evident demerit is the low Curie temperature (for PZNT and PMNT, T_c ~ 140-170 ^oC), that limits their further use in higher temperature environments. Nowadays, the actuators and sensors used for automotive and aerospace industries demand materials with higher Curie temperature than currently available. Specifically, under-hood automotive applications including the internal vibration sensor and the actuator for the fuel modulation must meet the requirement of an operation temperature as high as 300 ^oC. Also, aerospace and aircraft industries demand systems to function at temperatures even higher than 500^oC.[2] In view of these requirements, we need to develop high Curie temperature ferro/piezoelectric materials.

The Bi*Me*O_3 systems with low perovskite tolerance factors[i] have been predicted to have Curie temperatures higher than those of widely used ferroelectric $PbZrO_3$-$PbTiO_3$ (PZT). This forecast is derived from Morphotropic Phase Boundary (MPB) [ii] systems, as there is a link between the perovskite tolerance factor and the Curie temperature, proposed by Richard E. Eitel *et al.*. The Curie temperatures of the MPB solid solution (1-*x*)ABO_3-*x*$PbTiO_3$ with different end members ABO_3 are shown as a function of end member tolerance factors, in Table 1.1 and Fig. 1.1. In spite of the data scatter, it is clear that the MPB Curie temperature increases with reducing tolerance factor in the case of tolerance factor below 1. Fig. 1.1 shows that among the solid solutions of Bi*Me*O_3-$PbTiO_3$ perovskites, the end members $BiScO_3$, $BiInO_3$ and $BiYbO_3$ have the relatively low tolerance factors of 0.907, 0.884 and 0.857. From empirical analysis, one would predict that the corresponding MPB Curie temperatures of $BiScO_3$-$PbTiO_3$ (BSPT), $BiInO_3$-$PbTiO_3$ (BIPT) and $BiYbO_3$-$PbTiO_3$ (BYPT) would be respectively 450 ^oC, 550 ^oC and 650 ^oC, significantly greater than PZT (386^oC) and $PbTiO_3$ (490 ^oC) itself.[3]

Table 1.1 The $PbTiO_3$-based MPB solid solutions with different end members ABO_3, their MPB Curie temperature and end member tolerance factors are listed.[3]

Abbreviation	End member of solid solution (1-*x*)ABO_3+*x*$PbTiO_3$	End member tolerance factor (*t*)	MPB Curie temperature (^oC)
PMW	$Pb(Mg,W)O_3$	0.993	60
PMT	$Pb(Mg,Ta)O_3$	0.989	80
PNN	$Pb(Ni,Nb)O_3$	0.994	130
PFN	$Pb(Fe,Nb)O_3$	1.001	140
PMN	$Pb(Mg,Nb)O_3$	0.989	160
PMnN	$Pb(Mn,Nb)O_3$	0.973	187
PZnN	$Pb(Zn,Nb)O_3$	0.986	190
PST	$Pb(Sc,Ta)O_3$	0.977	205
PSn	$PbSnO_3$	0.978	220

[i] Tolerance factor: see section 2.4.
[ii] Morphotropic Phase Boundary (MPB): see section 2.5.

PCN	$Pb(Co,Nb)O_3$	0.985	250
PSN	$Pb(Sc,Nb)O_3$	0.977	260
PCW	$Pb(Co,W)O_3$	0.987	310
PIN	$Pb(In,Nb)O_3$	0.965	320
PH	$PbHfO_3$	0.969	340
NBT	$(Na,Bi)TiO_3$	0.977	350
PYN	$Pb(Yb,Nb)O_3$	0.951	360
PZ	$PbZrO_3$	0.964	385
BS	$BiScO_3$	0.907	450
BI	$BiInO_3$	0.884	~550
BY	$BiYbO_3$	0.857	~650

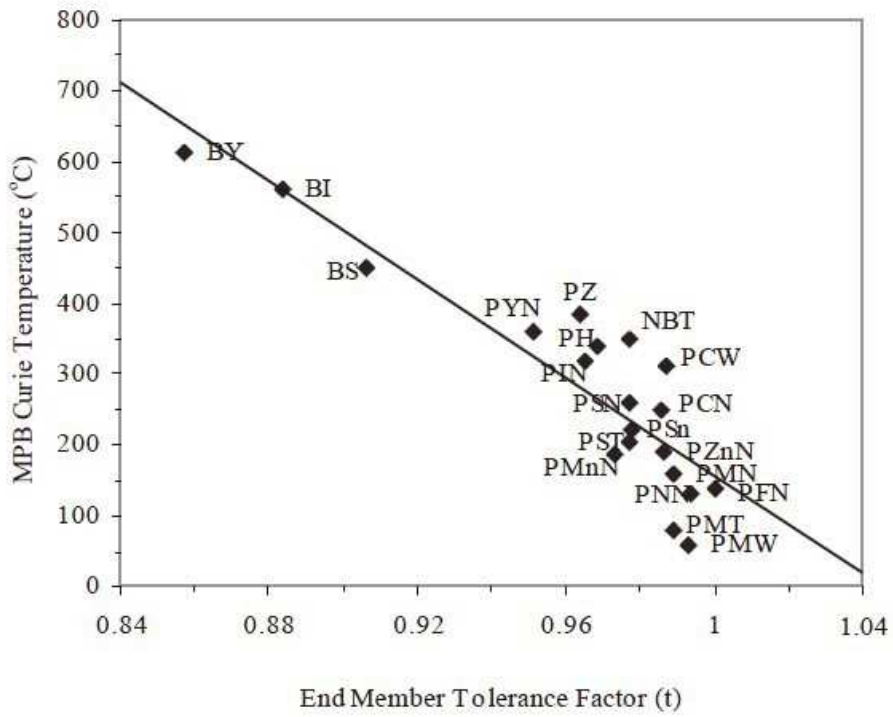

Fig. 1.1 MPB Curie temperature as a function of end member tolerance factor for the solid solutions of $PbTiO_3$ with alternative end members on the basis of Table 1.[3]

In ceramic, thin film and single crystal forms, the BSPT systems with a high Curie temperature of 450 °C exhibit excellent ferro/piezoelectrical properties (piezoelectric coefficient d_{33} = 460 pC/N and planar coupling coefficient k_p = 0.56) comparable to lead based ferroelectrics, driving research on these systems very hot. The phase diagram, domain structure, dielectric spectrum and piezoelectric properties have been investigated on BSPT systems.[4][5][6][7][8] However, the market application of BSPT is extremely limited by the high cost of Sc_2O_3, so looking for non-scandium perovskites is important. In fact, there are many possible compositions of Bi*Me*O_3–$PbTiO_3$, because the *Me* atom occupying the 'B' site of Bi*Me*O_3 can be chosen between several elements. In current literature, many Bi*Me*O_3–$PbTiO_3$ piezoelectric ceramics have been explored and their piezoelectric and associated properties at MPB are shown in Table 1.2. It is found that most of Bi*Me*O_3–$PbTiO_3$ compositions exhibit a relatively high Curie temperature, and yet, most of known Bi*Me*O_3–$PbTiO_3$ families, except BSPT, have low piezoelectric properties. An enhanced piezoelectric effect appears to develop at the expense of lower Curie temperature.[9]

Table 1.2 The dielectric, piezoelectric, electromechanical and related properties of the reported Bi*Me*O_3-$PbTiO_3$ piezoelectric ceramics near their MPB compositions.[9]

Compound	MPB (mol% PT)	T_c (°C)	d_{33} (pC/N)	k_p	tanδ	E_c (kV/mm)	c/a
$0.36BiScO_3$-$0.64PbTiO_3$	64	450	460	0.56	0.027	2.0	1.023
$0.45Bi(Sc_{1/2}Fe_{1/2})O_3$ -$0.55PbTiO_3$	55	440	298	0.49	0.033	2.2	1.021
$0.51Bi(Ni_{1/2}Ti_{1/2})O_3$ -$0.49PbTiO_3$	49	400	260	…	…	3.8	1.018
$0.63Bi(Mg_{1/2}Ti_{1/2})O_3$ -$0.37PbTiO_3$	37	478	225	…	0.063	5.0	1.034
$0.60(Bi_{0.9}La_{0.1})(Fe_{0.95}Ga_{0.05})O_3$ -$0.40(Pb_{0.9}Ba_{0.1})TiO_3$	40	386	186	0.37	0.04	2.8	1.030
$0.38Bi(Mg_{3/4}W_{1/4})O_3$ -$0.62PbTiO_3$	62	220	150	…	0.046	4.2	1.002

$0.35Bi(Ni_{2/3}Nb_{1/3})O_3$ -0.65$PbTiO_3$	65	273	140	0.22	0.11	2.8	
$0.4Bi(Sc_{3/4}Ga_{1/4})O_3$ -0.6$PbTiO_3$	60	477	124	…	0.05	3.9	1.027
$0.33(Bi_{0.7}La_{0.3})(Zn_{0.15}Mg_{0.35}Ti_{0.5})O_3-0.67PbTiO_3$	…	300	94	…	…	4.7	1.030

In some special applications (as outer space exploration), the devices need to work under temperatures much higher than those in the range where PZT and BSPT are stable. Thus it is necessary to develop piezoelectric materials with higher T_c. Promising, novel alternatives for substituting BSPT are based on $BiAlO_3$-$PbTiO_3$ (BAPT) (T_c ~ 480 ^oC[10]), $BiInO_3$-$PbTiO_3$ (BIPT) (T_c ~ 550 ^oC[11]) or $BiYbO_3$-$PbTiO_3$ (BYPT) (T_c ~ 650 ^oC[12]).

The $BiAlO_3$ ceramics with a Curie temperature above 520 ^oC were synthesized by a high-pressure method, exhibiting a piezoelectric coefficient of 28 pC/N and a remnant polarization of 9.5 $\mu C/cm^2$.[13] However, the applications of $BiAlO_3$ are highly restricted by its poor thermal stability and high-pressure synthesis method. Hence, using conventional solid-state synthesis, the $BiAlO_3$-$PbTiO_3$ ceramics have been studied focusing on their structures and phase transition behaviors.[14] Additionally, Guanghe Wu *et al*[15] investigated the structure and electrical properties of a $BiAlO_3$-$PbTiO_3$ thin film which has a high dielectric constant of 384 and a high remanent polarization of 58 $\mu C/cm^2$.

Both BIPT and BYPT have shown to be difficult to get in the pure perovskite structure using a solid reaction method. The perovskite $BiInO_3$ with few impurities has been synthesized under high pressure and temperature (6 GPa and 1273 K) similarly to the $BiAlO_3$ ceramics and its structure and vibrational properties have been studied.[16] The pure tetragonal perovskite BIPT ceramics with a Curie temperature of 582 ^oC have been synthesized using mixed oxide and sol-gel methods. [11] Niobium-modified BIPT ceramics with a Curie temperature of 542 ^oC exhibit good piezoelectric coefficients with d_{33} of 60 pC/N and d_{15} of 85 pC/N.[17] Dielectric,

ferroelectric and piezoelectric properties of BIPT thin films with a Curie temperature above 550 ^{o}C have been investigated, showing a permittivity of 650, a coercive field of 73 KV/cm and a remanent polarization of 22 μC/cm^2.[18]

Although Gao Feng *et al*[12] obtained BYPT ceramics that proved to work in piezoelectric applications at temperatures as high as 550 ^{o}C, they are not pure phases, coexisting with the pyrochlore phase $Yb_2Ti_2O_7$. BYPT ceramics doped with $BaTiO_3$ with d_{33} of 34 pC/N and T_c of 505 ^{o}C were still coexisting with the pyrochlore phase $Yb_2Ti_2O_7$.[19] The presence of the $Yb_2Ti_2O_7$ pyrochlore phase has a detrimental influence on the properties of BYPT, so pure BYPT is suggested to have higher Curie temperature and better piezoelectric properties. But until now, in comparison with BSPT, there is no report on the single crystal growth of BAPT, BIPT or BYPT compounds. Only density-functional theory calculations suggested that the MPB of BIPT would be at 0.33BI-0.67PT, and the MPB of BYPT would be at 0.3BY-0.7PT.[20] However, the MPB has not yet been experimentally studied in detail.

Therefore, the poor perovskite stability and low tolerance factors of BAPT, BIPT or BYPT, make the conventional solid state synthesis quite difficult. It is well known that perovskite can be formed by a route of flux method to grow single crystals. To overcome the bad effect of poor perovskite stability during the crystal growth, an effective approach includes the selection of the best flux compounds [21] and the introduction of a fraction of BSPT into BIPT or BYPT to help increasing the structural stability.

In comparison with the ceramics and thin films, BAPT, BIPT or BYPT crystals not only achieve the maximum ferro/piezoelectric responses, but also will become ideal candidates for exploring the intrinsic structural nature and physical origin of the high Curie temperature (T_c) and other physical properties. The present study of BAPT, BIPT and BYPT ferroelectrics addresses such questions as how to overcome their poor phase stability to obtain the pure perovskite phases and grow single crystals, and the structural origin of the high T_c. These issues are essential not only in the domain of applications but also for understanding the basic physical properties of these materials. This is needed to develop new materials, and also to further understand ferroelectrics. To solve these problems, this work includes single crystal growth and a crystal structural study of BAPT, BIPT and BYPT. Our main focus is centred on obtaining the promising BIPT single crystals for high temperature applications and on the detailed study their crystal structures, as well as local and macroscopic

ferro/piezoelectric properties.

This thesis is organized as follows:

This thesis is divided into six chapters.

Chapter 1 presents the motivation for the development of perovskite piezo/ferroelectric materials with high Curie temperature (Bi*Me*O_3-$PbTiO_3$ systems).

Chapter 2 presents a general background review of piezoelectricity and ferroelectricity in perovskite materials.

Chapter 3 presents concise experimental techniques, including the flux method for growing single crystal growth, X-ray diffraction, differential scanning calorimetry, Fourier transform infrared spectrometry, electron microscopy and piezoresponse force microscopy.

Chapter 4 is dedicated to the $BiInO_3$-$PbTiO_3$ single crystals. This is the most important section of this thesis. High Curie ferroelectric crystals of $0.3BiInO_3$-$0.7PbTiO_3$, $0.4BiInO_3$-$0.6PbTiO_3$ and $0.5BiInO_3$-$0.5PbTiO_3$ were successfully grown. A thorough structural study was performed by XRD and FTIR. The morphology of the crystallites and microstructure of BIPT were described from SEM and SAED imaging. The BIPT single crystals have a high Curie temperature above 550 ^{o}C as indicated by the DSC measurements that also revealed that the ferroelectric transition is first order. The local ferro/piezoelectric properties of BIPT were studied and the macroscopic dielectric, ferroelectric and piezoelectric properties were investigated.

Chapter 5 explores other high Curie temperature ferroelectric single crystals: $BiAlO_3$-$PbTiO_3$, $0.2BiYbO_3$-$0.8PbTiO_3$ and $0.37Bi(Sc_{0.5}Yb_{0.5})O_3$-$0.63PbTiO_3$. The $BiAlO_3$-$PbTiO_3$ single crystals with Curie temperature of 466 ^{o}C were successfully grown and their structure was refined by the Rietveld method using XRD. An attempt was also made to grow single crystals of $0.2BiYbO_3$-$0.8PbTiO_3$ and

$0.37Bi(Sc_{0.5}Yb_{0.5})O_3$ -$0.63PbTiO_3$, but unfortunately, the pure tetragonal phases were not obtained. The $0.37Bi(Sc_{0.5}Yb_{0.5})O_3$-$0.63PbTiO_3$ with an impurity phase was obtained.

Chapter 6 presents the main results and conclusions obtained in this thesis.

Chapter 2

Background on piezo/ferroelectricity in perovskite materials

2.1 Ferroelectric materials

Ferroelectric materials exhibit a spontaneous electric polarization which can be reversed by an external electric field. The crystallographic space group must be polar, therefore the unit cell cannot have a centre of symmetry and the crystal point group should belong to one of the 10 polar classes: 1, 2, *m*, *mm*2, 4, 4*mm*, 3, 3*m*, 6, 6*mm*.

These 10 polar space groups also accommodate the so-called pyroelectric materials, whose polarization varies, in principle, with temperature:

$$\Delta\vec{p} = \vec{r}\Delta T \,, \tag{2-1}$$

where $\vec{r}$ is the vector of the pyroelectric coefficients. A subclass of pyroelectric materials are the so-called the ferroelectric materials which must fulfill three conditions:

1) The material must undergo or tend to a phase transition from a polar to a non-polar structure with increasing temperature;
2) The polar phase must exhibit a spontaneous polarization;

3) The spontaneous polarization can be reversed by an external electrical field.

A typical ferroelectric material has hysteresis loops arising from the domains which are regions with parallel dipole moments. In the absence of an applied electric field, the macroscopic polarization of the specimen is zero due to an average of values of many domains. This condition, known as a multidomain state represents usually the lowest energy state.

A change of the polarization of ferroelectric materials can be achieved by applying an external electric field. At a high electric field, domains gradually grow and discontinuously switch to the direction of the electric field, leading to the change of polarization. The polarization tends to be a non-linear function of the external field. However, at low electric field, the polarization depends linearly on the applied field. In such regime, the electric displacement vector $\vec{D}$ and the electric field $\vec{E}$ are related by

$$D_i = \varepsilon_{ij} E_j , \tag{2-2}$$

where ε_{ij} is the 2-rank dielectric tensor. Fig. 2.1 shows the outline of the ferroelectric hysteresis loop traced by an alternating voltage applied to the material. At the highest fields, the domains are aligned with the applied field, so that the polarization tends to the saturation condition. If the applied field gradually reduces to zero from the saturation condition, some domains still keep their former arrangements, producing a remanent polarization. When the applied field is reversed, the polarization decreases and reverses orientation, until the saturation of polarization is obtained again. The applied field which nullifies the polarization is called the coercive field; it depends on the magnitude and frequency of the alternating voltage. The curve traced by the polarization in an alternating cycle of the electric field is the hysteresis loop. The area under the hysteresis loop gives the dielectric energy loss in the process. Thus, the material response to an applied electric field depends both on its electrical history and the applied field.[22]

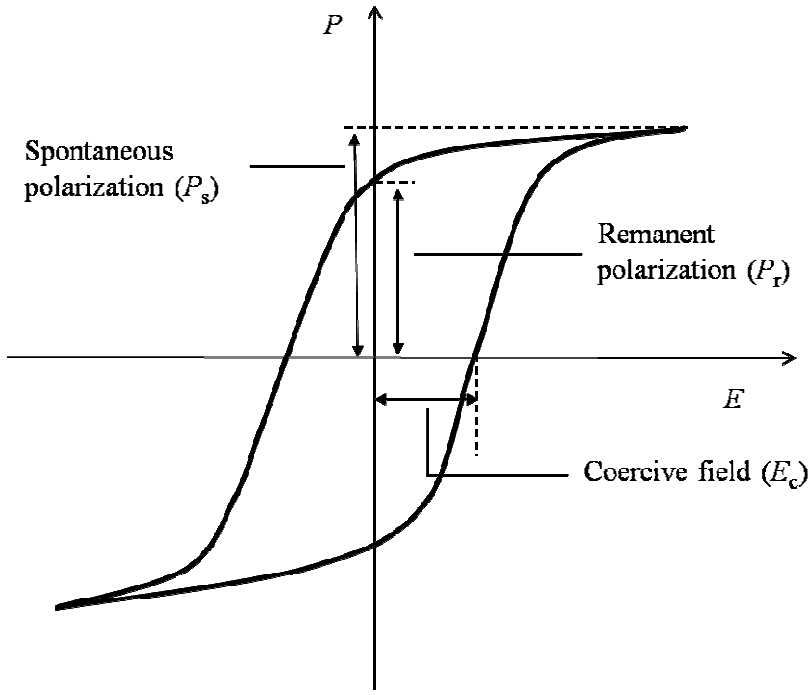

Fig. 2.1 The hysteresis loop of ferroelectric materials.

2.2 Piezoelectricity

Piezoelectricity describes a linear interaction between electrical and mechanical states in non-centroymmetric crystalline materials. There are two different piezoelectric effects: the direct piezoelectric effect and the reverse piezoelectric effect. The direct piezoelectric effect is the phenomenon where polarization of the material is generated from a mechanical stress, shown in Fig. 2.2 (a). The polarization P thus generated is proportional to the stress T as

$$P = d\ T\ . \tag{2-3}$$

The converse effect is the mechanical movement generated by an external electric field applied to the material shown in Fig. 2.2 (b). The strain S is proportional to the applied electric field E,

$$S = d\ E\ . \tag{2-4}$$

The constant d is the piezoelectric coefficient of the material. It can be proven from

thermodynamics that the piezoelectric coefficient is the same for the direct and converse effects. The above description is, however, a simplified picture as the constitutive equations should be written in tensor form.

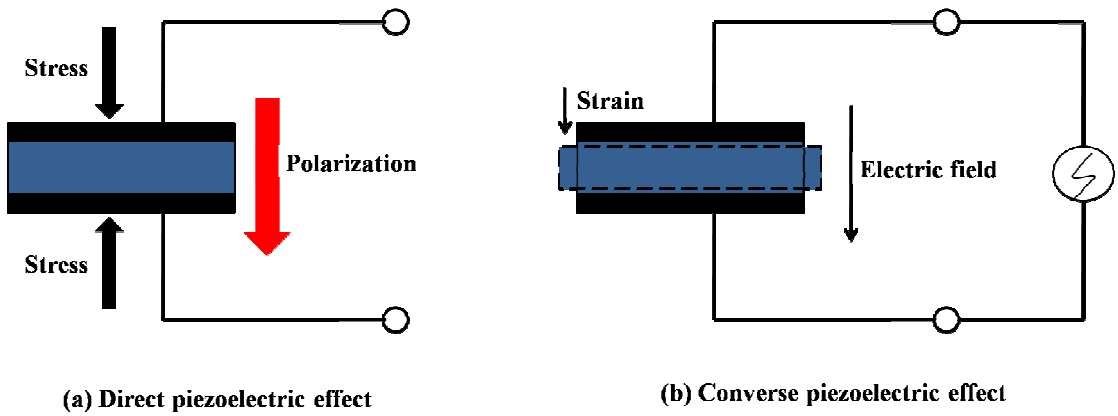

Fig. 2.2 Macroscopic piezoelectric effects.

Actually, the piezoelectric behavior can be described as a cross coupling relationship between the elastic mechanical stress T and strain S, and electric displacement vector $\vec{D}$ and electric field $\vec{E}$. On the basis of the linear theory of piezoelectricity[23], the tensor notation is employed to identify the coupling between the electrical and mechanical coefficients, defined as:

$$S_{ij} = s^{E}_{ijkl} T_{kl} + d_{kij} E_k \tag{2-5}$$

$$D_i = d_{ikl} T_{kl} + \varepsilon^{T}_{ik} E_k \,. \tag{2-6}$$

Generally, $\vec{D}$ and $\vec{E}$ are vectors (1-rank Cartesian tensor) and permittivity ε is 2-rank Cartesian tensor. In principle, strain and stress are also 2-rank tensors; s is 4-rank tensor and d is 3-rank piezoelectric tensor. Sometimes, it is convenient to introduce a compressed matrix notation instead of the tensor notation for the description of piezoelectricity easily. According to Table 2.1, the notation p or q take the place of ij or kl, where the values of p, q are 1, 2, 3, 4, 5, 6 and the values of i, j, k,

l are 1, 2, 3 in this matrix notation. The indexes *i*, *k*, *p*, *q* refer to different directions with respect to the material coordinate system, as shown in Fig. 2.3. The equations (2-5) and (2-6) can be written in this compact notation as:

$$S_p = s_{pq}^E T_q + d_{pk} E_k \tag{2-7}$$

$$D_i = d_{iq} T_q + \varepsilon_{ik}^T E_k \tag{2-8}$$

where s_{pq}^E is the elastic compliance tensor at constant electric field, ε_{ik}^T is dielectric constant tensor under constant stress, d_{pk} is piezoelectric constant tensor, S_p is the mechanical strain in *p* direction, D_i is electric displacement in *i* direction, T_q is mechanical stress in *q* direction, and E_k is the electric field in *k* direction.

Table 2.1 Matrix notation[23]

ij or *kl*	*p* or *q*
11	1
22	2
33	3
23 or 32	4
31 or 13	5
12 or 21	6

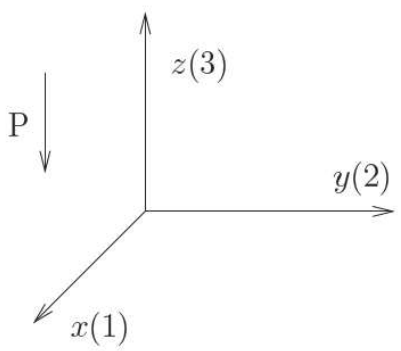

#	Axis
1	x
2	y
3	z
4	Shear around x
5	Shear around y
6	Shear around z

Fig. 2.3 Axis nomenclature for compact matrix notation.[24]

Equations (2-7) and (2-8) can be written in matrix form as:

$$\begin{bmatrix} S_1 \\ S_2 \\ S_3 \\ S_4 \\ S_5 \\ S_6 \end{bmatrix} = \begin{bmatrix} s_{11}^E & s_{12}^E & s_{13}^E & s_{14}^E & s_{15}^E & s_{16}^E \\ s_{21}^E & s_{22}^E & s_{23}^E & s_{24}^E & s_{25}^E & s_{26}^E \\ s_{31}^E & s_{32}^E & s_{33}^E & s_{34}^E & s_{35}^E & s_{36}^E \\ s_{41}^E & s_{42}^E & s_{43}^E & s_{44}^E & s_{45}^E & s_{46}^E \\ s_{51}^E & s_{52}^E & s_{53}^E & s_{54}^E & s_{55}^E & s_{56}^E \\ s_{61}^E & s_{62}^E & s_{63}^E & s_{64}^E & s_{65}^E & s_{66}^E \end{bmatrix} \begin{bmatrix} T_1 \\ T_2 \\ T_3 \\ T_4 \\ T_5 \\ T_6 \end{bmatrix} + \begin{bmatrix} d_{11} & d_{21} & d_{31} \\ d_{12} & d_{22} & d_{32} \\ d_{13} & d_{23} & d_{33} \\ d_{14} & d_{24} & d_{34} \\ d_{15} & d_{25} & d_{35} \\ d_{16} & d_{26} & d_{36} \end{bmatrix} \begin{bmatrix} E_1 \\ E_2 \\ E_3 \end{bmatrix} \tag{2-9}$$

and

$$\begin{bmatrix} D_1 \\ D_2 \\ D_3 \end{bmatrix} = \begin{bmatrix} d_{11} & d_{12} & d_{13} & d_{14} & d_{15} & d_{16} \\ d_{21} & d_{22} & d_{23} & d_{24} & d_{25} & d_{26} \\ d_{31} & d_{32} & d_{33} & d_{34} & d_{35} & d_{36} \end{bmatrix} \begin{bmatrix} T_1 \\ T_2 \\ T_3 \\ T_4 \\ T_5 \\ T_6 \end{bmatrix} + \begin{bmatrix} \varepsilon_{11}^T & \varepsilon_{12}^T & \varepsilon_{13}^T \\ \varepsilon_{21}^T & \varepsilon_{22}^T & \varepsilon_{23}^T \\ \varepsilon_{31}^T & \varepsilon_{32}^T & \varepsilon_{33}^T \end{bmatrix} \begin{bmatrix} E_1 \\ E_2 \\ E_3 \end{bmatrix} \tag{2-10}$$

The electromechanical coupling coefficient k is another important parameter to describe the transduction efficiency of the materials. It represents the capability of a material to interconvert mechanical energy and electrical energy, and is defined as:

$$k^2 = \frac{\text{Converted Mechanical Energy}}{\text{Input Electrical Energy}} \tag{2-11}$$

for the converse effect, or

$$k^2 = \frac{\text{Converted Electrical Energy}}{\text{Input Mechanical Energy}} \tag{2-12}$$

for the direct effect.

As described above, the symmetry of the material is a decisive factor to determine whether the dielectric, piezoelectric or electric components of the tensors is non-zero and unique in the piezoelectric materials. For instance, the piezoelectricity of materials with 4*mm* crystal symmetry such as tetragonal PZT or $BaTiO_3$, may take the form

$$\begin{bmatrix} S_1 \\ S_2 \\ S_3 \\ S_4 \\ S_5 \\ S_6 \end{bmatrix} = \begin{bmatrix} s_{11}^E & s_{12}^E & s_{13}^E & 0 & 0 & 0 \\ s_{21}^E & s_{22}^E & s_{23}^E & 0 & 0 & 0 \\ s_{31}^E & s_{32}^E & s_{33}^E & 0 & 0 & 0 \\ 0 & 0 & 0 & s_{44}^E & 0 & 0 \\ 0 & 0 & 0 & 0 & s_{55}^E & 0 \\ 0 & 0 & 0 & 0 & 0 & s_{66}^E \end{bmatrix} \begin{bmatrix} T_1 \\ T_2 \\ T_3 \\ T_4 \\ T_5 \\ T_6 \end{bmatrix} + \begin{bmatrix} 0 & 0 & d_{31} \\ 0 & 0 & d_{32} \\ 0 & 0 & d_{33} \\ 0 & d_{24} & 0 \\ d_{15} & 0 & 0 \\ 0 & 0 & 0 \end{bmatrix} \begin{bmatrix} E_1 \\ E_2 \\ E_3 \end{bmatrix} \tag{2-13}$$

and

$$\begin{bmatrix} D_1 \\ D_2 \\ D_3 \end{bmatrix} = \begin{bmatrix} 0 & 0 & 0 & 0 & d_{15} & 0 \\ 0 & 0 & 0 & d_{24} & 0 & 0 \\ d_{31} & d_{32} & d_{33} & 0 & 0 & 0 \end{bmatrix} \begin{bmatrix} T_1 \\ T_2 \\ T_3 \\ T_4 \\ T_5 \\ T_6 \end{bmatrix} + \begin{bmatrix} \varepsilon_{11}^T & 0 & 0 \\ 0 & \varepsilon_{22}^T & 0 \\ 0 & 0 & \varepsilon_{33}^T \end{bmatrix} \begin{bmatrix} E_1 \\ E_2 \\ E_3 \end{bmatrix}. \tag{2-14}$$

For a plate of a piezoelectric material where both stress and electric field are along the z-axis, the electromechanical response can be expressed as:

$$S_3 = s_{33}^E T_3 + d_{33} E_3 \tag{2-15}$$

$$D_3 = d_{33} T_3 + \varepsilon_{33}^T E_3 . \tag{2-16}$$

At the same time, the corresponding longitudinal factor for electromechanical coupling factor k_{33} is defined as:

$$k_{33}^2 = \frac{d_{33}^2}{\varepsilon_{33}^T s_{33}^E} \tag{2-17}$$

The constants d_{33}, ε_{33}^T, and s_{33}^E are frequently found in the manufacturer's data of piezoelectric materials available in the market.[24][25]

The applications of piezoelectricity cover many areas, and typically piezoelectric ferroelectric materials are used for the following reasons. First, many ferroelectric materials have a high piezoelectric effect, so they can achieve high and efficient electromechanical transduction of energy. Second, since the direction of remanent polarization in ferroelectric materials usually can be manipulated by an applied electric field, it is possible to obtain a device with a macroscopic unipolar direction, which is necessary for piezoelectric action. Finally, materials with perovskite structure have broad applications such as in capacitors and are very important also in piezoelectric applications. Ferroelectric perovskite materials are already available in mass production, and also offer a relatively low production cost.[26]

2.3 Curie Temperature

In ferroelectric materials, the Curie temperature (T_c) is described as the temperature where the spontaneous polarization of the materials rapidly increases as their temperature lowers below the critical point. Conversely, when the ferroelectric material is heated, at the Curie temperature the spontaneous polarization falls to zero. Above the transition temperature, the dielectric permittivity of proper ferroelectrics[iii] typically follows the so-called Curie-Weiss law,

$$\varepsilon = \varepsilon_0 + \frac{C}{T - T_0} \tag{2-18}$$

where ε_0 is the free-space permittivity, C is the Curie constant, T is temperature, and T_0 is the Curie-Weiss temperature.[27] For second order ferroelectric phase transitions, $T_0 = T_c$, while for first order ferroelectric phase transitions, $T_0 < T_c$.

2.4 Perovskite Structure (Tolerance Factor)

One of the most well known materials is $BaTiO_3$[28] a perovskite that undergoes a phase transition from cubic to tetragonal at 120 ^oC, and other transitions of lower symmetry at lower temperatures.

Fig. 2.4 (a) shows the ideal perovskite structure with stoichiometric ABX_3 cubic symmetry, where A is a large cation in 12-fold coordination, and B is a smaller cation in 6-fold coordination, surrounded by an octahedron of X anions. This structure can be considered as a framework of BX_6 octahedra with the A cation placed in voids between octahedra (Fig. 2.4 (b)).

[iii] For most ferroelectrics (called proper ferroelectrics), the relatively permittivity is observed to increase, reaching a peak at T_c and decreasing below T_c. There is a class of ferroelectric, known as improper or extrinsic ferroelectrics, for which there is no peak in permittivity, just an anomaly.[37]

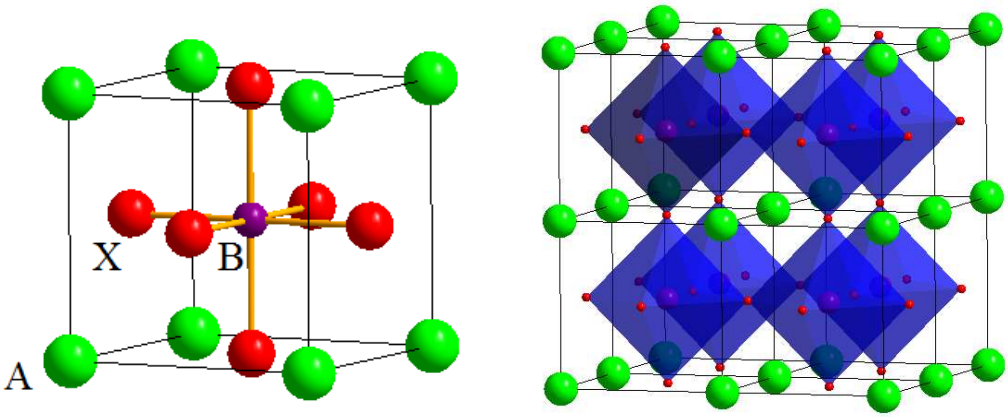

(a) (b)

Fig. 2.4 The unit cell (a) and BX_6 octahedra (b) in the ideal ABX_3 perovskite structure.

Many perovskite materials have this ideal cubic structure at high temperature. However, on cooling, they will undergo a transition from cubic symmetry to lower symmetry ones. The distortion of the cubic structure can be observed at room temperature. The phase transition is often due to either a distortion of the octahedra, tilting of the octahedra, or displacement of ions in the octahedra.[29]

In the case of cubic $BaTiO_3$, each titanium ion is in the centre, of by an octahedron of oxygen anions. Fig. 2.5 shows the oxygen ions surrounding a titanium ion in the tetragonal form of $BaTiO_3$ where the titanium atom is slightly off centre. It becomes a distorted cubic form. The reversible dipole moment arises from the titanium off-center position in the oxygen octahedron in the unit cell of $BaTiO_3$. The smaller the off-center displacement, the easier is the reversion of dipole moment.[22]

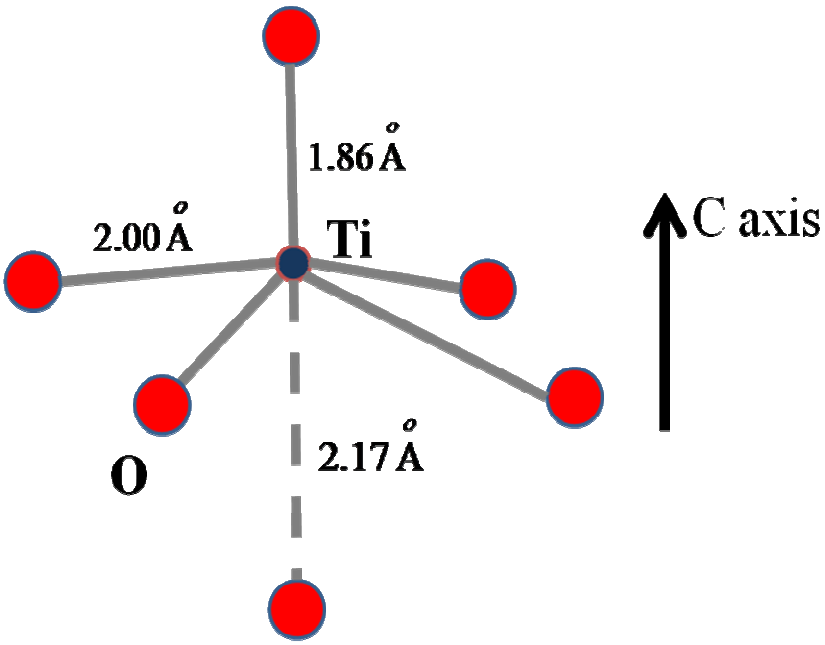

Fig. 2.5 A titanium ion surrounded by six oxygen ions in the tetragonal structure of $BaTiO_3$.[22]

The "tolerance factor" is a convenient parameter to assess the distortions in a non-ideal perovskite material. Based on the geometrical packing, Goldschmidt [30] proposed the concept of a tolerance factor '*t*', defined as

$$t = \frac{r_A + r_X}{\sqrt{2}\left(r_B + r_X\right)}. \tag{2-19}$$

Here r_A, r_B and r_X are ionic radii of atoms A, B and X, respectively. Usually these radii are given as Shannon radii.[31] The tolerance factor is often used to predict the crystal system of complex perovskites at room temperature. For the known perovskite materials, a stable perovskite structure can be obtained within the range $0.88 < t < 1.09$. For t greater than or equal to 1, tetragonal and cubic structures are usually observed, while for t less than 1, monoclinic, rhombohedral or orthorhombic structures are often found in perovskite materials. It is possible to obtain the desired high Curie temperature, and other ferroelectric properties, by suitable doping on the A or B sites. Although the tolerance factor has been used to predict many Pb-based ferroelectric materials, other factors, such as ionic electronegativity also play a role. Since many perovskite materials change phase with temperature, the tolerance factor

has to be used with caution. It can be used only as a rough guide to predict perovskite structures, but for a more accurate prediction, further considerations are needed.[32][33]

2.5 The morphotropic phase boundary (MPB)

Some solid solutions of ferroelectric materials have optimum dielectric, piezoelectric and elastic properties near the boundary between different phases, the so-called morphotropic phase boundary (MPB). Complex-structured solid solutions are a major group of the MPB applications of ferroelectric materials, such as $Pb(Zr_{1-x},Ti_x)O_3$ (PZT) that is used in high-performance in actuator applications. In PZT, MPB is associated with the ferroelectric phase transition between the rhombohedral and the tetragonal phases due to a change of composition or mechanical pressure. In the vicinity of the MPB of ferroelectric materials, along with the sudden change of crystal structure, dielectric and piezoelectric properties achieve a maximum. At the MPB compositions in ferroelectric materials two phases coexist, balanced in free-energy and coupled with each other, resulting in the enhanced polarizability which is the main reason of the high dielectric and piezoelectric properties. Currently, many MPB systems are being developed from the ferroelectric relaxor-$PbTiO_3$ materials, extending to the lead based relaxor materials $Pb(B_1B_2)O_3$ with complex perovskite structures, as depicted in Fig. 2.6.

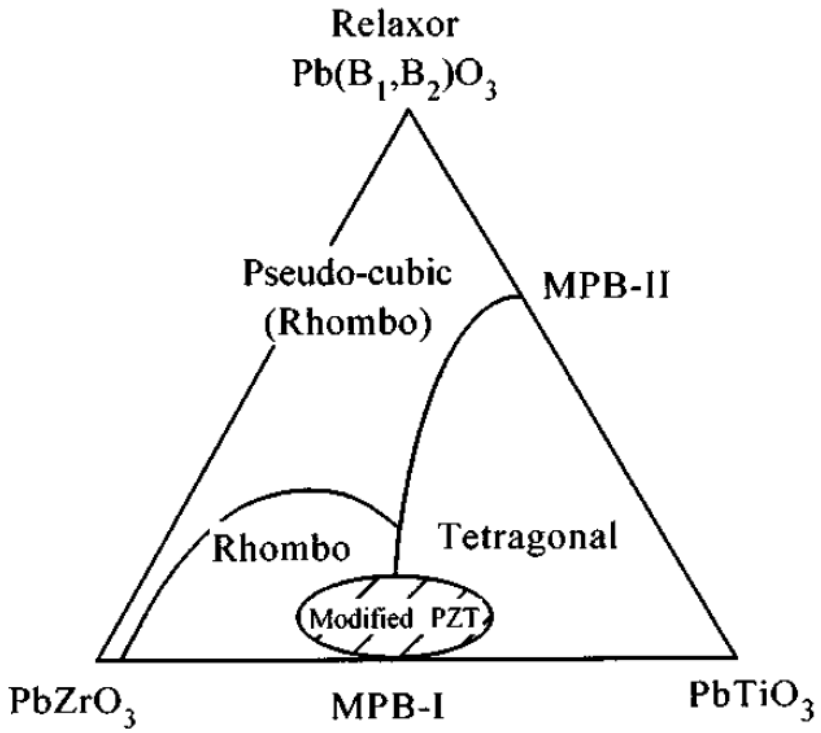

Fig. 2.6 Ternary diagram showing MPBs in relaxor $Pb(B_1B_2)O_3$ piezoelectric ceramics.[1]

Exploring the compositions along the MPB of solid-solution materials is a good way for selecting promising end members that achieve the highest ferroelectric properties. $Pb(Mg_{1/3}Nb_{2/3})O_3$-$PbTiO_3$[34] is a good example for utilizing MPB to maximize the associated performance. We employ a similar idea in this work to search for promising high Curie temperature piezo/ferroelectric materials of high performance. Fig. 2.7 shows the piezoelectric coefficient d_{33} at room temperature plotted as a function of Curie temperature for PZT, modified PZTs, and Relaxor-PT systems. The effect of Curie temperature (T_c) on the piezoelectric properties reveals that the enhanced piezoelectric properties come at the expense of a lower Curie temperature and therefore, less polarization stability, i.e., aging and ultimately loss of piezoelectric activity.[1]

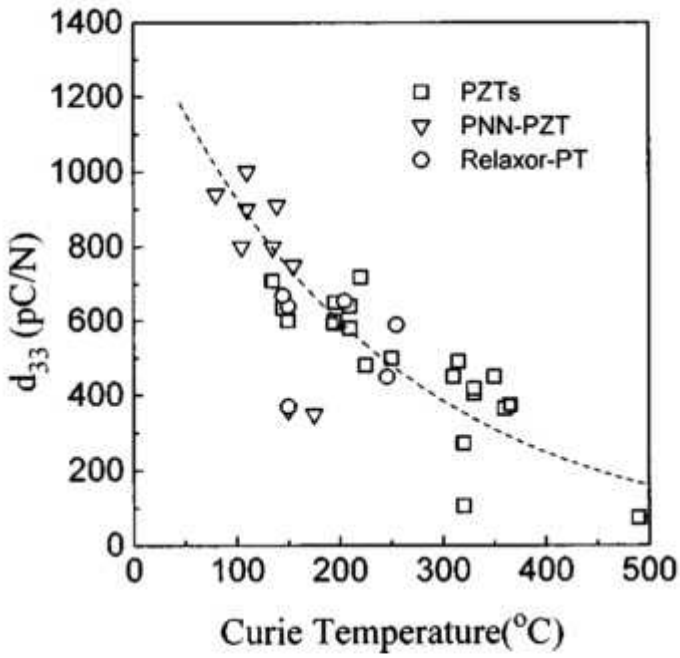

Fig. 2.7 Piezoelectric coefficient (d_{33}) of $PbTiO_3$-based piezoelectric ceramics versus Curie temperature.[1]

2.6 Ferroelectric phase transitions

A phase is a thermodynamic system in which the material has uniform physical properties. The transformation from one phase to another one is called a phase transition. Considering the change of order parameter and symmetry under a phase transition, phase transitions can be classified as either first order or continuous phase transitions (including second order transitions and higher order). In a ferroelectric crystal, polarization is the order parameter of the system.

The description of a ferroelectric phase transition can be obtained by assuming that the thermodynamic potential is a polynomial function. The elastic Gibbs free energy G_1, the thermodynamic potential, is normally expressed as a function of temperature, stress, and displacement. To simplify the problem, let us assume that electric displacement $D_i = D$ is aligned only along a crystallographic axis resulting

in the spontaneous polarization along this direction, and also that the applied electric field is restricted to this direction. Also, we assume that stresses vanish and the paraelectric phase has a center of symmetry. With these assumptions, the free energy G_1 can be expressed as the simple polynomial form

$$G_1 = \frac{1}{2}\alpha D^2 + \frac{1}{4}\gamma D^4 + \frac{1}{6}\delta D^6 , \tag{2-20}$$

where the energy is that of the paraelectric phase and a sixth order expansion is used for mathematical simplicity. Although the coefficients α, γ, δ are usually dependent on temperature, we assume γ and δ independent of temperature for the simplest description of first and second order ferroelectric transitions.[35]

2.6.1 Second order ferroelectric phase transitions

The electric field E, parallel to D, is the derivative of Gibbs free energy (equation (2-20)) with respect to displacement D at constant temperature T, expressed as:

$$E = \left(\partial G_1 / \partial D\right)_T = \alpha D + \gamma D^3 + \delta D^5 . \tag{2-21}$$

Fig. 2.8(a) depicts the free energy G_1 dependence of displacement D according to equation (2-20) with parameters γ and δ positive. It shows that if $\alpha > 0$ there is a minimum value at $D = 0$ in the free energy curve; however, if $\alpha < 0$ there are double minima at $D \neq 0$. Since $E = \left(\partial G_1 / \partial D\right)_T$, the extrema describe the equilibrium values of electric displacement at $E = 0$, and, furthermore, since $\vec{D} = \varepsilon_0 \vec{E} + \vec{P}$, the extrema represent also the spontaneous polarization P_s. As G_1 is also dependent on temperature, following the extrema of G_1 as function of temperature we can determine how the polarization changes with temperature.

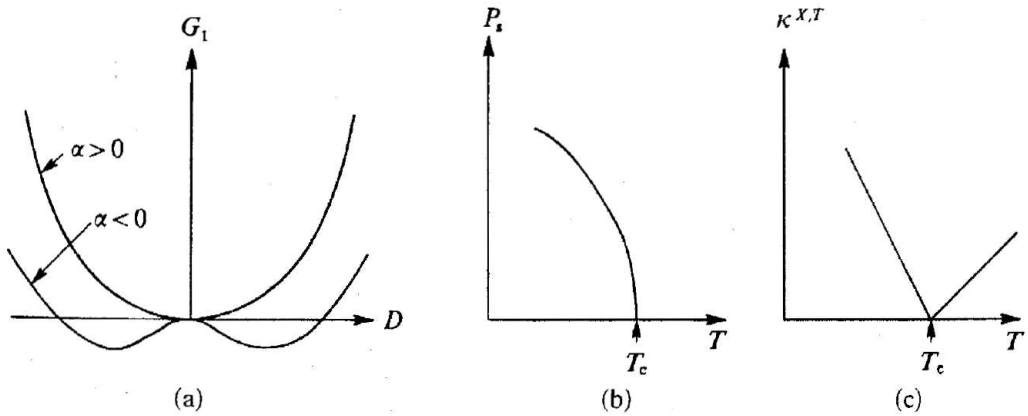

Fig. 2.8 (a) Free energy shown as a function of the displacement at different temperatures. The free-energy parameter α is proportional to $T - T_c$. (b) Spontaneous polarization (P_s) versus the temperature. (c) Reciprocal isothermal permittivity ($\kappa^{X,T}$) versus temperature. It is assumed that the system is near a second-order ferroelectric phase transition.[35]

It is clear that the spontaneous polarization P_s is continuous as α goes through zero, which means that the system undergoes a second order phase transition. In fact, α is the reciprocal permittivity of the paraelectric phase at $E = 0$, according to equation (2-21). Conventional phenomenological theory (inspired in Landau's theory of phase transitions and often termed Devonshire theory for ferroelectrics) assumes that close to Curie temperature T_c the parameter α has a linear dependence on temperature with a positive constant β, expressed as:

$$\alpha = \beta(T - T_c) = \kappa^{X,T>T_c} . \tag{2-22}$$

The spontaneous polarization P_s and isothermal dielectric constant $\kappa^{X,T}$ below T_c fulfill, respectively,

$$P_s^2 = \beta(T_c - T)/\gamma, \;\; P_s \to 0 \tag{2-23}$$

and

$$\kappa^{X,T} = \beta(T_c - T) + 3\gamma P_s^2, \;\; P_s \to 0 . \tag{2-24}$$

The substitution of equation (2-23) into equation (2-24) gives

$$\kappa^{X,T} = 2\beta(T_c - T), \;\; T < T_c . \tag{2-25}$$

Fig. 2.8 (b) and (c), respectively, depict the spontaneous polarization P_s and isothermal dielectric constant $\kappa^{X,T}$ as a function of temperature near the second

order ferroelectric transitions. The slope of the curve of $\kappa^{X,T}$ against temperature at $T < T_c$ is negative, while the slope of the curve of $\kappa^{X,T}$ against temperature at $T > T_c$ is positive. The value of the slope below T_c is twice as large as above T_c.

Since $S = -\left(\partial G_1 / \partial T\right)_{D,X}$ in conventional phenomenological theory, the entropy S and specific heat c can be calculated in this model. Using $\alpha = \beta\left(T - T_c\right)$ and assuming coefficients γ and δ independent of temperature, differentiating the Gibbs energy (equation (2-20)) with respect to T generates the zero-field entropy

$$S = -\frac{1}{2}\beta P_s^2 . \tag{2-26}$$

Substituting the spontaneous polarization given by equation (2-23) below T_c generates the entropy

$$S = \frac{1}{2}\beta^2\left(T - T_c\right)/\gamma, \quad T < T_c \tag{2-27}$$

$$S = 0, \qquad T > T_c \tag{2-28}$$

close to T_c. Correspondingly, $T\,\mathrm{d}S/\mathrm{d}T$ calculated in the zero field gives us the specific heat:

$$c^{X,P_s} = \frac{1}{2}\beta^2 T/\gamma, \quad T < T_c \tag{2-29}$$

$$c^{X} = 0, \quad T > T_c . \tag{2-30}$$

In the description above, the entropy S is continuous through the Curie temperature T_c while the specific heat c undergoes a discontinuous jump at T_c: $\Delta c = \frac{1}{2}\beta^2 T_c/\gamma$.

To sum up, a second order phase transition normally satisfies continuous first derivatives of the free energy (*e.g.* P_s and S) and has a discontinuity in second derivatives (*e.g.* c). However, most ferroelectric materials do not undergo second order phase transitions but rather first order phase transitions with discontinuous first derivatives of free energy.[35]

2.6.2 First order ferroelectric phase transitions

In the case of first order phase transitions, coefficient γ is negative and δ is positive in the Gibbs function (equation (2-20)) and the coefficient α is the reciprocal isothermal permittivity at constant stress in the paraelectric phase arising from equation (2-21). The assumption of Devonshire theory is using Curie-Weiss form

$$\alpha = \beta(T - T_0), \tag{2-31}$$

where T_0 is called the Curie-Weiss temperature that is not equivalent to the Curie temperature T_c. Assuming $\gamma = -\gamma' (\gamma' > 0)$ the free energy has the form

$$G_1 = \frac{1}{2}\beta(T - T_0)D^2 - \frac{1}{4}\gamma' D^4 + \frac{1}{6}\delta D^6. \tag{2-32}$$

The dielectric equation of state (equation (2-21)) with positive constant β, δ and γ' is now expressed as

$$E = \beta(T - T_0)D - \gamma' D^3 + \delta D^5. \tag{2-33}$$

The free energy G_1 as a function of temperature is sketched in Fig. 2.9 (a). It possibly exhibits extreme values at zero value of D and also at $D = \pm D_c$ ($P = \pm P_c$) in the case of non-zero D. The requirements for the occurrence of a zero field first order transition are that the free energy G_1 and the first derivative of the free energy G_1 with respect to the displacement D are simultaneously equal to zero in the case of non-zero D, represented by the equations

$$\frac{1}{2}\beta(T - T_0) - \frac{1}{4}\gamma' P_s^2 + \frac{1}{6}\delta P_s^4 = 0 \tag{2-34}$$

and

$$\beta(T - T_0) - \gamma' P_s^2 + \delta P_s^4 = 0. \tag{2-35}$$

The solutions to meet these conditions are

$$T = T_c = T_0 + \frac{3}{16}\frac{\gamma'^2}{\beta\delta} \tag{2-36}$$

$$P_s^2 = P_c^2 = \frac{3}{4}\frac{\gamma'}{\delta}, \quad T = T_c \tag{2-37}$$

for the temperature and the value of spontaneous polarization at Curie temperature T_c. Differentiating equation (2-33) with respect to D at zero-field gives us the reciprocal permittivity

$$\kappa^{X,T} = \beta(T - T_0) - 3\gamma' P_s^2 + 5\delta P_s^4 . \tag{2-38}$$

Above T_c it clearly satisfies $\kappa^{X,T} = \beta(T - T_0)$, as assumed in Devonshire theory. The corresponding reciprocal permittivity on approaching to the Curie temperature from above can be expressed as

$$\kappa^{X,T} = \frac{3}{16}\frac{\gamma'^2}{\delta} + \beta(T - T_c), \quad T \to T_c^+ . \tag{2-39}$$

Below T_c, when the temperature T infinitely is close to the Curie temperature T_c from below, substituting the spontaneous polarization obtained solving equation (2-33) when $E = 0$ into equation (2-38) generates

$$\kappa^{X,T} = \frac{3}{4}\frac{\gamma'^2}{\delta} + 8\beta(T_c - T), \quad T \to T_c^- . \tag{2-40}$$

In the above descriptions, the reciprocal permittivity undergoes a finite discontinuity at Curie temperature T_c. Comparing equations (2-39) and (2-40), we can deduce that the ratio of the reciprocal permittivity at T_c^- to that at T_c^+ is 4 and the slope $\mathrm{d}\kappa/\mathrm{d}T$ nearby but below T_c is -8 times as great as that above T_c. Figs. 2.9 (b) and (c) depict the schematic changes of spontaneous polarization and reciprocal permittivity around Curie temperature T_c.

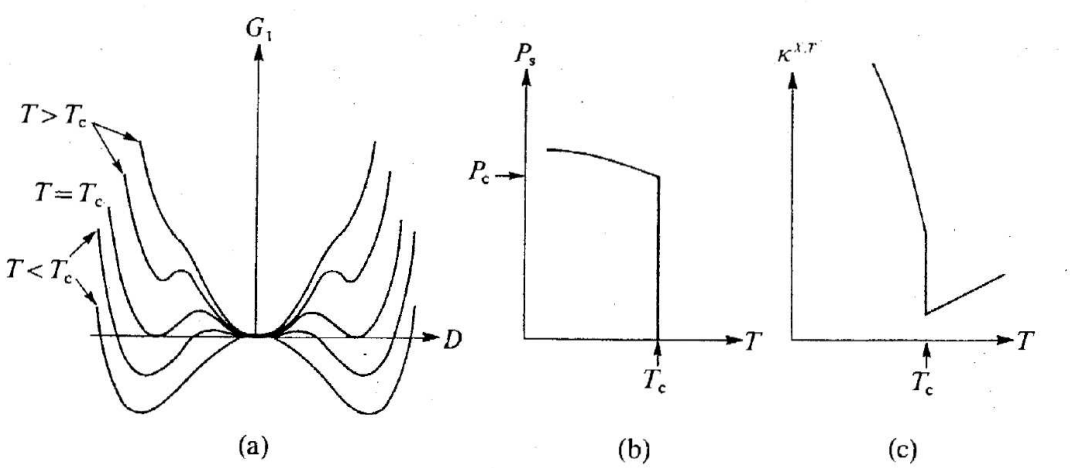

Fig. 2.9 (a) Free energy as a function of displacement at different temperatures. (b) Spontaneous polarization (P_s) as a function of temperature. (c) Reciprocal isothermal permittivity ($\kappa^{X,T}$) versus temperature. It is assumed that the system is near a first-order ferroelectric phase transition.[35]

Since a first order phase transition does not represent a singular point in Gibbs free energy, the paraelectric phase can persist as a metastable phase below the Curie temperature, while the ferroelectric phase can exist as a metastable phase above Curie temperature. These metastable phases occupy the local minima in Fig. 2.9 (a), that have energies higher than that of minima representing the stable phases. In theory, the lowest temperature for the presence of a paraelectric phase as a metastable state is T_0, while the highest temperature for the ferroelectric phase existence at zero field and as a mestable state is $T_1 = T_0 + \left(\gamma'^2/4\beta\delta\right)$. In practice, these metastable states are really found in first order phase transitions and the actual phase transition temperature by approaching from the low temperature side is a little higher than that from the high temperature side. This temperature difference may reach $T_1 - T_0$ and this phenomenon of 'lagging behind' is called thermal hysteresis. Actually, the thermal hysteresis is smaller than the theoretical value and because of non-uniformities in the material the transition from a mestasble state to a stable state is usually a complex dynamic process which cannot be explained by simple thermodynamic theory.

The change of entropy and latent heat are discontinuous at T_c arising from a discontinuity of the change in polarization shown in Fig. 2.9 (b). Since entropy $S = -\left(\partial G_1/\partial T\right)_{D,X}$, $S = -\frac{1}{2}\beta P_c^2$ at T_c in ferroelectric phase and it is zero in paraelectric phase. At Curie temperature T_c the corresponding discontinuity in entropy is

$$\Delta S = \frac{1}{2}\beta P_c^2 . \tag{2-41}$$

Furthermore, the latent heat calculated from the entropy discontinuity is

$$T_c \Delta S = \frac{1}{2} T_c \beta P_c^2 . \tag{2-42}$$

Due to thermal hysteresis and difficulties on the experiments including non-uniformities in sample compositions, temperature gradients, non-uniform heat-rates, *etc*., the real first order phase transitions are more complex than described by the above results obtained from simple thermodynamic theory.

In summary, materials with a first order phase transitions experience the transition at $T_c = T_0 + \left(3\gamma'^2/16\beta\delta\right)$ between two absolutely stable states with discontinuous spontaneous polarization and susceptibility. Close to Curie temperature

the reciprocal susceptibility has a linear dependence on temperature on both phases with a ratio of the slopes in paraelectric phase to the ferroelectric phase of $-8:1$. Due to the presence of metastable states, the paraelectric and ferroelectric phases are metastable down to T_0 or up to $T_1 = T_0 + \left(\gamma'^2/4\beta\delta\right)$, respectively. Therefore, the maximum possible thermal hysteresis is $\gamma'^2/4\beta\delta$ from a supercooling temperature to a superheating temperature. Above T_1, although the metastable ferroelectric phase disappears, the ferroelectric phase can be still induced by a sufficient strong applied electric field until $T_2 = T_0 + \left(9\gamma'^2/20\beta\delta\right)$. Above T_2, only the paraelectric phase persists. In practice, this theory is useful for characterization of this type of materials and we can estimate the parameters β, γ' and δ by measuring the dielectric properties near the Curie temperature T_c.[35]

Chapter 3

Experimental Techniques

3.1 Flux method for growing single crystals

The flux method is a method of crystal growth from high temperature solutions, widely used in exploring new materials. The flux method uses a solvent to dissolve the components of the desired materials at high temperature. To avoid reaction of the materials with crucibles, we normally choose refractory, non-reactive crucibles such as those made of platinum or alumina. For single crystal growth, the solution has to be saturated and the starting temperature is a little higher than saturation temperature. A slow cooling of the solution is then used to precipitate and nucleate the crystals. In this process, the crystal formation takes place either by spontaneous nucleation or by the introduction of seed crystals. As the crystals form, saturation of the solution is reduced and also the saturation temperature is lower. So the process of the crystal growth can continue as the solution cools.

The flux method has many advantages over other crystal growth methods. In theory, we can use this method to grow any crystals by a suitable flux in reasonable crystal growth conditions. It is a good method when one is dealing with incongruent

melting materials which need to grow below their melting temperatures. A lower temperature can be used compared to other methods, materials that decompose at high temperature or highly volatile compounds can still be used. This method does not require special equipment and can operate at relatively low temperatures with lower cost.

Unfortunately, there are also some disadvantages. Many of crystals grown from flux method have relatively small sizes (from millimeter to centimeter) that limits its use for some applications. Also, some elements of the desired crystals can possibly be substituted by the flux elements and there may be flux inclusions in the grown crystals.

3.1.1 The solvent selection

A solution is a homogenous system composed by a solute dissolved in a solvent. For a given solute, the selection of solvents plays a very important role on the crystal growth procedure, the quality and size of grown crystals. Ideally, we wish to choose a solvent with low viscosity and volatility, non-corrosive and non-toxic with a good solubility and convenient solubility gradient. The solubility, which is the maximum amount of the solute dissolved in a solvent, dictates the growth procedure. High solubility makes the growth of bulk single crystals difficult, while small solubility restricts to the growth rate and size of single crystals. At the same time, the choice of the solubility gradient for growing bulk single crystals cannot be flat or too steep. A flat solubility gradient means that lowering the temperature has little effect on the supersaturation of the solution, and a steep solubility gradient means that even a small temperature change can cause a great fluctuation of the supersaturation; both conditions preclude the growth of high quality bulk crystals. However, a slow evaporation of the solvent is a good choice for a small solubility gradient to grow single crystals. During the crystal growth process, the growth units are transported through diffusion to the location of the growth, so a low viscosity of the solvent is beneficial for crystal growth. Based on the physical and chemical properties of

materials, one should choose a proper flux with a low melting point and a large difference between melting point and boiling point for increasing the reaction extent. The solute and solvent should not have undesired reactions. Also, the flux should be easily separated from the desired single crystals. Actually, it is difficult to find a flux to satisfy all above requirements and thus we often resort to complex (mixture) fluxes to meet these conditions. However, crystals grown in complex fluxes tend to be less stable, and these fluxes must be carefully chosen.[36]

There are two main types of flux: metals (such as In, Ga and Sn) which are mostly used in the growth of semiconductor crystals; oxides and halides (such as PbO and PbF_2) which are mostly used for the growth of ionic crystals. In practice, the oxides and fluorides including PbO, PbF_2, Bi_2O_3, Na_2O, B_2O_3, P_2O_5, MoO_3 are often used and a mixture consisting of two or three of them are used in many cases.[37]

3.1.2 The general principles and classification of crystal growth from high temperature solution

Single crystal growth can be regarded as a process aiming to obtain a long-range orderly arrangement of atoms, ions or molecules through a phase transition from liquid, vapor or solid state into the desired crystalline phase. When the system is in dynamic equilibrium, with a minimum free energy, crystal growth cannot occur. Crystal growth is possible if there is a suitable disturbance of this equilibrium such as temperature, pressure or chemical potential changes, resulting in many different crystal growth methods; the flux method is one of them. The formation of a single crystal occurs through the following three steps: formation of supersaturation or supercooling of the solution; formation of nucleation centers; transport to nucleation centers for crystal growth.

Because the driving force for crystal growth is supersaturation or supercooling, the maintenance of the steady supersaturation or supercooling states during crystal

growth are prerequisites for obtaining high-quality single crystals. Nucleation is an important step in crystal growth, which can occur spontaneously or induced by a seed. [38]

We can describe the supersaturation of a system by specifying the concentration and temperature. The concentration driving force (ΔC) can be expressed in the form

$$\Delta C = C - C^*, \tag{3-1}$$

where C and C^* are, respectively, the actual and equilibrium concentration of the solution at a given temperature. The supersaturation ratio (S) is defined as

$$S = \frac{C}{C^*}. \tag{3-2}$$

The relative supersaturation (σ) is described as

$$\sigma = \frac{C - C^*}{C^*} \quad \text{or} \quad \sigma = S - 1. \tag{3-3}$$

The supersaturation of a solution can be estimated by measuring the concentration of the solution at a given temperature with the known corresponding solubility. [36]

Fig. 3.1 diagrammatically shows a typical eutectic phase diagram of a solution from which crystal growth from high temperature solution will be attempted. Let us consider the basic situation without agitating and introducing seed crystals. When the system is located at A with composition n_A in equilibration, a slow cooling of the solution can be used for spontaneous nucleation by reaching B as indicated by curve 1. In this process, it passes through a supersaturation or supercooling region in the range between the liquidus line and the dashed line crossing B in Fig. 3.1, called the metastable or Ostwald-Miers region. From temperature T_B, we continue the cooling of the solution (curve 1) until the eutectic point is reached and the crystal grows until the solution reaches composition n_F. Alternatively, evaporation can be used to force the the solution to go through the metastable region and nucleating at D in curve 2. Curve 3 shows the solvent transportation process between a hotter and a cooler region. In practice, the three transitions could occur at the same time, while only one is dominant. In this phase diagram, the solvent can be an element, a compound or a combination of compounds. The solute is an element or a compound with a melting point generally higher than that of the solvent.[39]

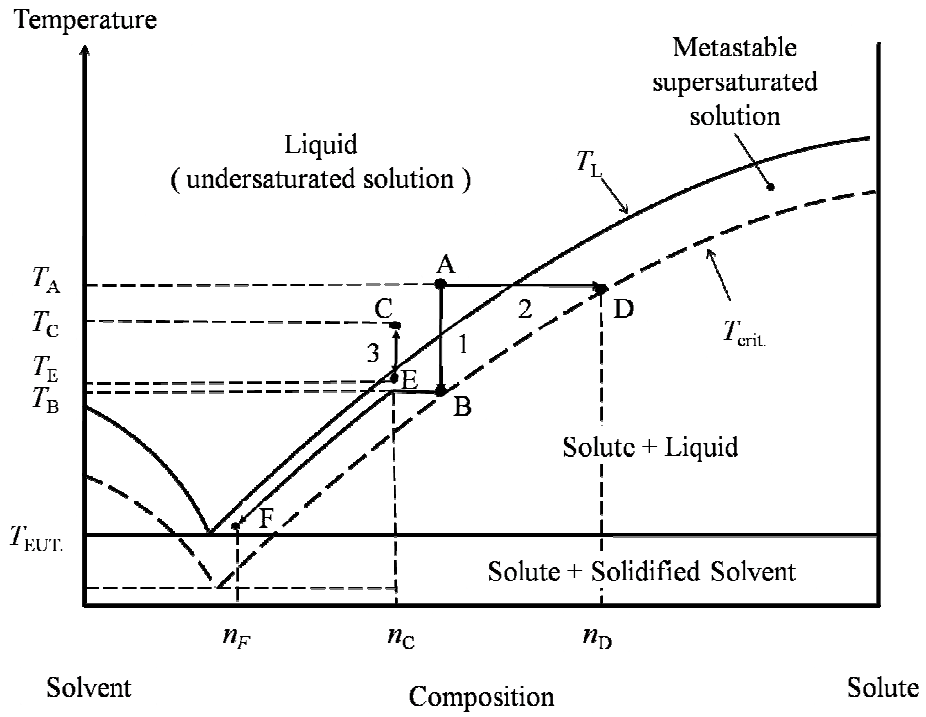

Fig. 3.1 Typical eutectic phase diagram. Curve 1 corresponds to a slow cooling crystal growth; Curve 2 corresponds to a crystal growth by solvent evaporation; Curve 3 depicts a gradient transport process.[39]

3.1.3 The method of crystal growth from high temperature solution (flux method) - Slow Cooling Method

The method of crystal growth from high temperature solution (flux method) can be generally divided into two types: spontaneous nucleation and seed growing technique. The former includes slow cooling, solvent evaporation, transport techniques and so on. The latter includes top seeding method, kyropoulos method[40], zone melting method, the crucible tilt and the crucible reverse method, *etc*. The slow cooling method will now be described.

Slow cooling method is the most common flux method that normally employs a cooling rate of 0.2 ^{o}C/h to 10 ^{o}C/h. For growing high-quality single crystals bigger

than a few millimeters, the cooling rate must be less than 1 ^{o}C/h. The equipments used in this technique are very simple and inexpensive. In favourable cases, a crystal of 2 to 10 mm suitable for the structure determination and physical properties measurements can be obtained. The slow-cooling method is very useful to explore new materials and new structures.[41] However, a narrow range of growth temperature is necessary to avoid the appearance of undesired single crystals in the crystal growth. Although it is difficult to accurately control the system temperature, this technique has significant advantages and is widely used in single crystal growth.[36]

The procedure of the slow-cooling technique is the following. The starting materials are mixed thoroughly and added into the crucible with no more than 3/4 full for crystal growth in a muffle furnace. For preventing evaporation of volatile solvent or solute constituents, the crucible should be sealed or covered. First, for the materials to sufficiently react and homogenize, the furnace temperature is raised from ten up to a hundred degrees above the melting point and hold on several hours to a day. Then the temperature is quickly lowered to the melting point (saturation temperature), or better to nucleation temperature. The nucleation temperature is not easy to measure and is unstable and often related with the purity of materials. So, an estimate of the nucleation temperature higher than the actual temperature is often used. Then we slowly drop the temperature with a rate of 0.1-5 ^{o}C/h. Last, we stop the crystal growth before crystalline phases other than the desired one appear. Fig. 3.2 is the schematic picture of crystal growth by flux method in our work. Ideally, we should use a totally isolated system with a good temperature controller and with a set of several thermocouples to monitor the temperature in different places. In our case we used the commercial furnace Termolab (Electric Furnace, LDA), capable of attaining a maximum temperature of 1150 ^{o}C, shown in Fig. 3.3. Temperature is read from a *K*-type thermocouple and the temperature rates are controlled to better than 1 ^{o}C using a PID temperature controller.

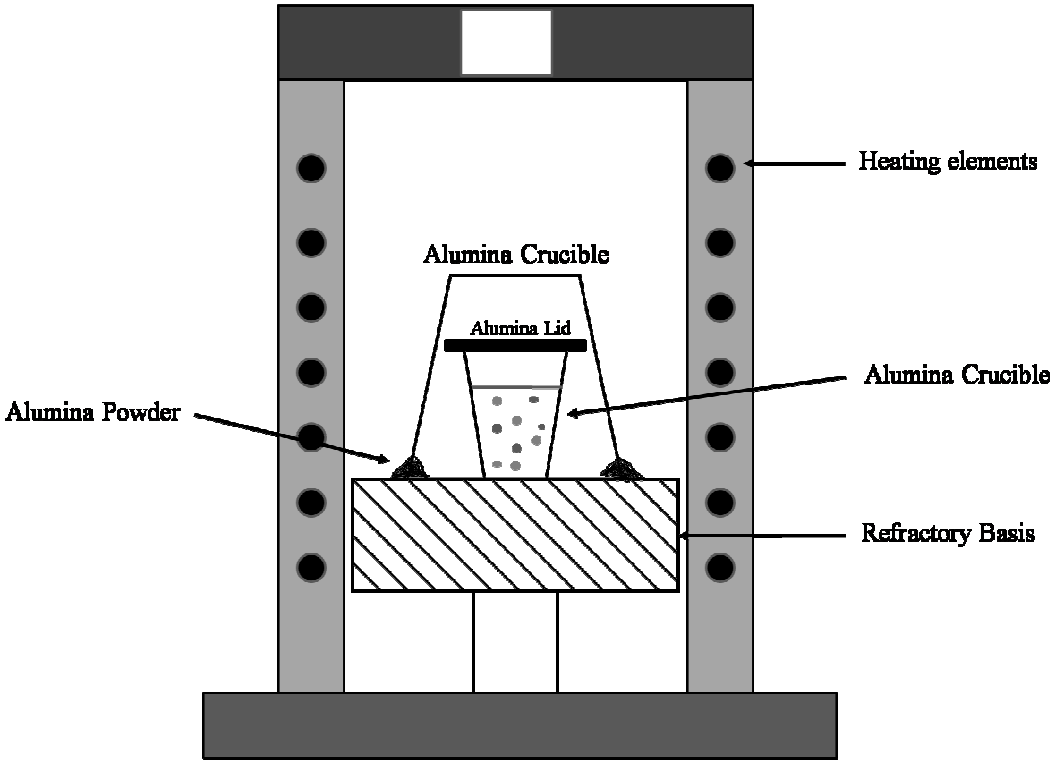

Fig. 3.2 Schematic picture of crystal growth by flux method.

Fig. 3.3 Termolab Electric Furnace.

3.2 X-ray diffraction

X-ray diffraction is widely used to identify and describe the crystalline materials and provide information for structure analysis based on their diffraction pattern. When a beam of X-ray passes through a sample, the X-ray interaction with the electrons of the sample produces scattering. When the X-rays are scattered by a crystal, a regular structure with distances between atomic layers similar to the wavelength of X-rays, the occurrence of constructive and destructive interference between the scatted rays leads to X-ray diffraction. The produced diffraction patterns contain important structural information about the crystal. Such X-ray diffraction patterns can be described by Bragg's Law.

3.2.1 Bragg's Law

When an X-ray beam is incident at some angle on the surface of a crystal, the beam is partially scattered by the first layer of atoms at the surface and the remaining beam passes through to the second layer of atoms. Part of the beam reaching the second layer of atom is scatted by the second layer and the remaining beam penetrates to the third layer (Fig 3.4). This process continues to occur in the next several layers and the cumulative scattering from the regular structure produces the diffraction pattern. X-ray diffraction requires that the sample must be crystalline and the spacing of crystal layers must be roughly similar to the wavelength of the radiation.

Suppose that a narrow beam of X-ray is incident on the crystal surface at angle θ. Constructive interference occurs when

$$n\lambda = 2d\sin\theta\,, \tag{3-4}$$

where θ is the incident angle of the X-ray beam, n is the integer assigned to the diffraction order, λ is the X-ray wavelength and d is the spacing between the layers of atoms. Equation (3-4) is the important Bragg's Law. When the incident angle satisfies

the condition

$$\sin\theta = \frac{n\lambda}{2d}, \tag{3-5}$$

X-rays can be reflected from the crystal, while at all other angles as a result of destructive interference no reflection occurs. Note that only crystalline solids which have a regular structure will show a diffraction pattern and amorphous materials will not. [42]

While the positions of the maximum of the diffraction pattern are given by Bragg's law, the relative intensities of the maxima are related to the contents of the unit cell, *e.g.*, the type and position of the atoms inside the cell. Actually these intensities are given by the squared amplitude of the Fourier transform of the electronic charge density in the unit cell. Therefore, these intensities contain invaluable information about the structure and by suitable analysis can be used to solve the crystal structure or refine a given structural model based on a measured diffraction pattern.

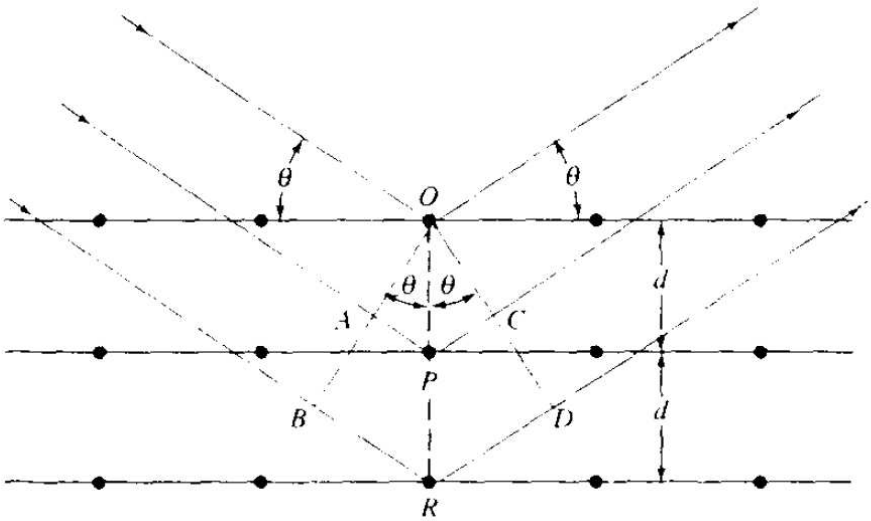

Fig. 3.4 Diffraction of an X-ray beam by a crystal.[42]

3.2.2 Instrumentation

In fact most materials are not single crystals, but polycrystalline or in powder form, consisting of a lot of very small crystallites oriented in all possible directions. When the X-ray beam strikes at a powder sample, most possible diffraction peaks can be produced and detected by scanning the Bragg's angle. A powder X-ray diffractometer working in Bragg-Brentano geometry is typically used for the study of powder samples. It is typically composed of an X-ray source, a detector, a sample holder and a way to vary the incident angle. Fig. 3.5 shows that when the X-ray strikes on the sample surface at incident angle ω, the detector situated at opposite direction of the source receives the signals of the intensity of the X-ray at the diffraction angle 2θ. In our work, a Bruker D8 Advance X-ray diffractometer (Fig. 3.6) is used.

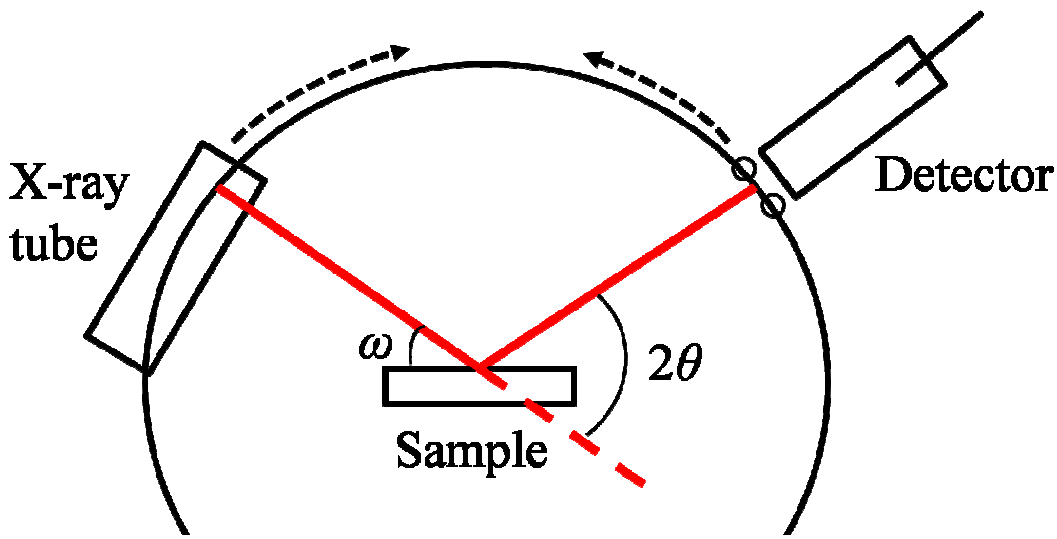

Fig. 3.5 Schematic diagram for a powder X-ray diffractometer operating in Bragg-Brentano geometry. The diffraction angle 2θ is that between the incident X-ray beam and the detector; it is always twice the incident angle ω between the incident beam and the sample.

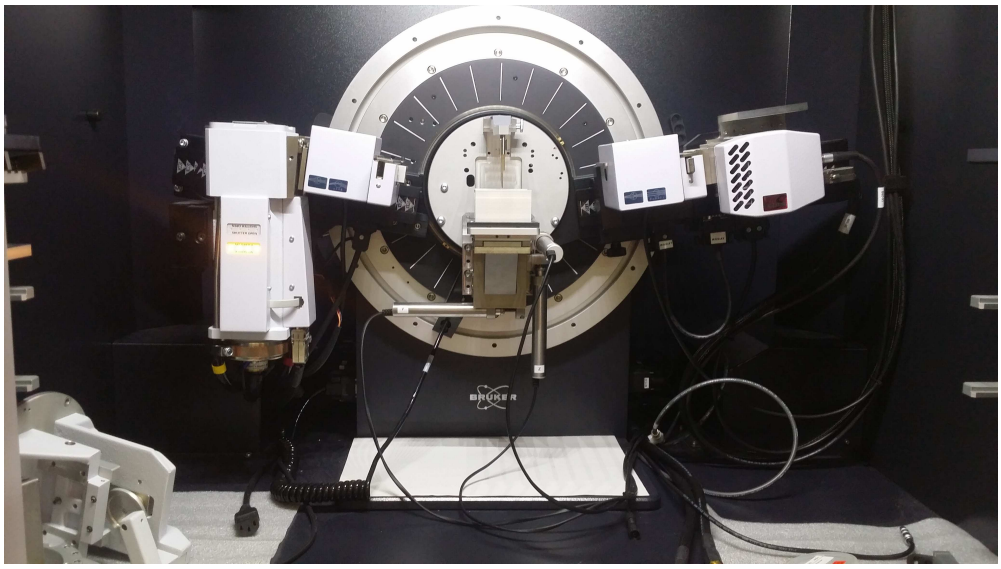

(a)

(b)

Fig. 3.6 Bruker D8 Advance X-ray diffractometer.

The most common X-ray source is the X-ray tube and one design of such tube is shown in Fig. 3.7. It consists of a high vacuum tube and generally contains a massive block of copper with a metal target anode and a filament of tungsten acting as the cathode. There are many possible target materials such as tungsten, copper, chromium, scandium, molybdenum, rhodium, silver, iron and cobalt. Electrons are produced in the heated filament by the thermionic effect and a high voltage is applied between the anode and the cathode so that electrons are fired and accelerated to strike the anode, emitting X-rays. The intensity of the X-rays can be controlled by adjusting the filament current, and their wavelength or energy is determined by the accelerating voltage. Finally, the X-rays exit the X-ray tube from the beryllium window. Because a lot of heat is generated in this process, the copper block usually needs be cooled by water.

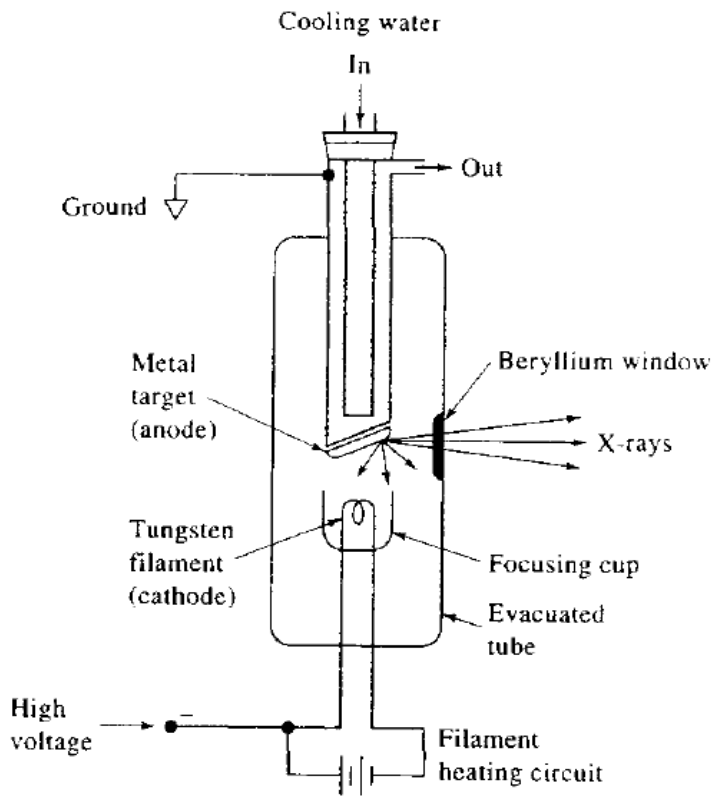

Fig. 3.7 Schematic picture for an X-ray tube.[42]

While early X-ray instruments used photographic film to detect and record the information of X-rays, modern equipments are generally equipped with other type of X-ray detectors. Most used X-ray detectors include gas-filled proportional chambers, scintillation counters and semiconductor transducers. Comparing with film, scintillation counters and semiconductor based detectors can measure diffraction intensities more accurately, and the data is directly available in digital format (counts/s), more convenient to be processed by a computer that is often shared to control the instrument and analyze the data.[42]

3.3 Differential Scanning Calorimetry (DSC)

Differential scanning calorimentry (DSC) is one of the conventional thermal analysis techniques which are often used to study the thermal behavior of a material. Other conventional thermal analysis techniques include thermogravimetry (TG), differential thermal analysis (DTA), dynamic mechanical analysis (DMA) and thermomechanical analysis (TMA).[43]

DSC measures the difference in heat flow rate between the sample and a reference sample as a function of temperature. DSC can determine the enthalpy and the characteristic temperatures of a physical transformation such as a phase transition or chemical reaction. When a sample undergoes a physical transformation, the enthalpy change in the transformation determines a heat exchange between the sample and its surroundings and this produces a DSC signal. The two common types of DSC are the heat flux DSC and the power compensation DSC. In the heat flux DSC the sample and a reference sample are placed on a thermoelectric platform in the same furnace. When the furnace is heated or cooled, the heat can be transferred to the sample through the platform with a given thermal resistance. In this process we can measure the temperature difference of sample and reference sample as a result of their different heat capacities and the sample heat flow is assumed to be proportional to the temperature difference. The heat flux DSC measures the heat exchanged between the sample and the environment.[44] The temperature difference ΔT between sample and

reference sample is measured with thermocouples or other temperature to voltage transducers. The result of the DSC measurement is a curve of heat flux as a function of temperature. An endothermic or exothermic reaction of the sample can be shown as either a positive or negative peak in the DSC curve, depending on the instrument. Thus, we can measure the amount of heat absorption or heat release during a physical transformation. The enthalpy of a given physical transformation can be directly calculated by integrating the area under the peak in this curve, expressed as

$$\Delta H = kA \tag{3-6}$$

where ΔH is the enthalpy of a physical transformation, k is the calorimetric constant and A is the area under the endothermic or exothermic peak in the curve. The calorimetric constant k depends on the instrument and can be determined by measuring a standard sample.[45]

DSC can quickly and accurately measure enthalpy changes in a wide temperature range using a small sample of mass of a few mg. DSC can be combined with other techniques in the same instrument, a popular combination being DSC and TG. The combination of these two techniques is called Simultaneous Thermal Analysis (STA). This is the case of the instrument used in this work, the Perkin-Elmer STA-6000 (Fig. 3.8).

Fig. 3.8 Perkin-Elmer STA-6000.

3.4 Fourier transform infrared spectrometry (FTIR)

Fourier transform infrared spectrometry (FTIR) is a method of measuring an infrared spectrum of a sample. Infrared spectrum includes the information about the absorption peaks of the sample occurring at the vibrational frequencies of the atoms in the material. The infrared spectrum can be used as a fingerprint of the material. When the infrared radiation passes through a material, a part of infrared radiation is absorbed by the material and the remaining being either reflected or transmitted. The infrared spectrum of a material characterizes its molecular structure. Hence, infrared spectroscopy is a good tool either in qualitative identification of materials or in quantitative analysis with modern software technology.[46]

A FTIR spectrometer contains the following components: the source, the interferometer, the sample, the detector and the computer.

Many recent interferometers are designed on the basis of the original Michelson interferometer (two-beam interferometer). The Michelson interferometer divides an incident beam of radiation into two beams going through two different paths and then recombines the two beams, resulting in the interference between the beams. The detector can measure the intensity variation of beam dependence of the path difference. Fig. 3.9 shows a simple Michelson interferometer, consisting of two mutually vertical plane mirrors. One is a fixed mirror and the other one is a movable mirror. A beamsplitter bisecting the two mirrors is used to divide the incident collimated beam from the source into two beams. Part of the beam is reflected to the fixed mirror and part of the beam is passed through to the movable mirror. When the two beams are reflected back to the beamsplitter, the interference between coherent beams occurs and the partial reflection and transmission happen again. The resulting interferogram including the spectral information is produced through the intensity variation of the beams to the detector and back to the source which is dependent on the path difference of the beam traversed.[47]

The signals from the interferometer cannot be directly interpreted, so we use a Fourier transformed to obtain the frequency spectrum. A computer can be used to carry out this Fourier transformation and provide the desired spectral information for analysis.

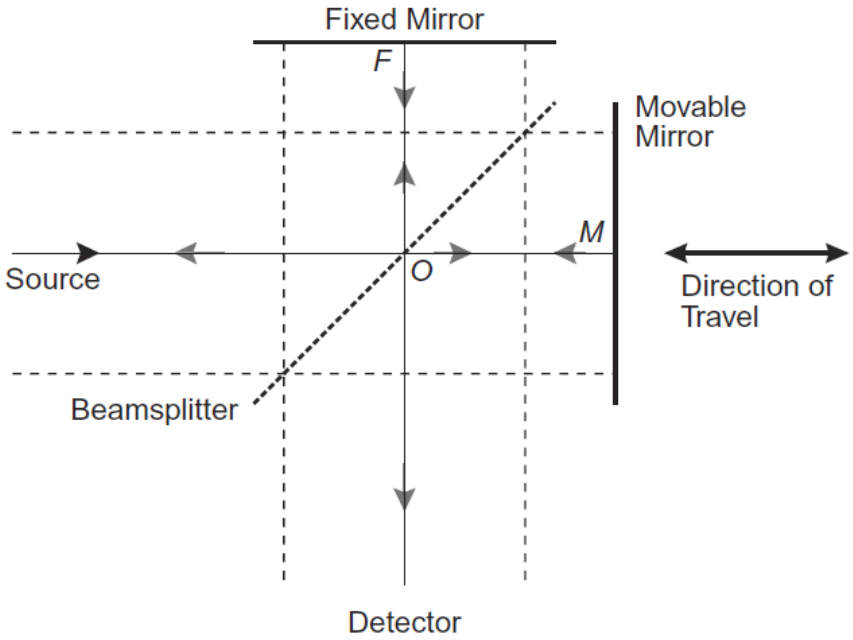

Fig. 3.9 Schematic picture of a Michelson interferometer.[47]

FTIR has many advantages compared with the alternative wavelength dispersive technique. Because the information of all the wavelengths can be detected simultaneously and there are no slits to restrict the transmission of the radiation, it can effectively improve the signal-to-noise ratio for a given scanning time. The moving mirror which is the only movable unit in the interferometer can quickly move in short distances and this results in a very short measurement time, of just a few seconds. One can add several fast scans to improve the signal/noise ratio. Therefore, highly accurate results can be obtained by FTIR and as such it is an invaluable technique for structural analysis.[48]

3.5 Electron Microscopy

Electron Microscopy (EM) is a technique that uses a beam of accelerated electrons to produce an image of a specimen. The beam of electrons is focused and accelerated and then the images are magnified through electromagnetic lenses operating in high vacuum.[49]

When a beam of electrons strikes at a specimen, the incident electrons interact with the atoms in the specimen, undergoing elastic and inelastic scattering, as shown in Fig. 3.10. In the elastic scattering, electrons keep their kinetic energies and only change their trajectories due to the large difference of the mass between the electrons and the nuclei of the atoms. In the inelastic scattering, the incident electrons may collide with the electrons around the atomic nucleus in the specimen and then eject these electrons from their original orbits; this results in an energy loss of the incident electrons. These interactions result in signals that can be used to form the image in the electron microscopy.[50]

There are two basic types of the EM: the scanning electron microscope (SEM) and the transmission electron microscope (TEM). They are used for different applications. In short, the most common SEM produces an image in three dimensions using the detection of back-scattered or secondary electrons, when the beam scans the surface of a sample, while TEM forms an image in two dimensions by the electrons going through an extremely thin slice of the specimen.[49]

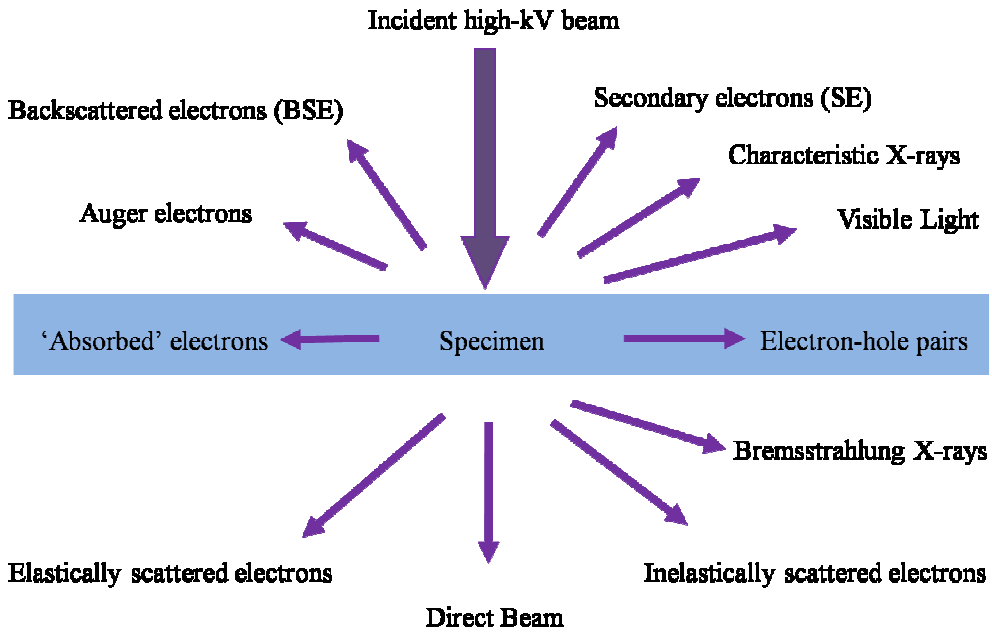

Fig. 3.10 Signals produced from the interaction of a beam of high-energy electrons with a thin specimen.[51]

3.5.1 Scanning electron microscope (SEM)

The scanning electron microscope is widely used for materials characterization. SEM can produce images of the surface topography, composition, structure and electrical properties of the material by scanning the specimen with a high energy electron beam. The interaction between the electron beam and the atoms in the specimen produces various signals which can be detected while the electron beam is scanned across a raster scanning.

The most important signals produced by SEM are secondary electrons and backscattered electrons. Secondary electrons are generated from the inelastic collisions and scattering between the electron beam and the electrons of the specimen, while backscattered electrons are generated from the elastic collisions and scattering between the electron beam and atomic nuclei or electrons of the specimen. The images collected from the secondary electrons can convey the information of the surface topography. In most SEMs, secondary electrons are used to produce the high

resolution images of the specimen, better than 5 nm depending on the beam size. At the same time, backscattered electron images can also provide information of chemical composition of the specimen, because the intensity of backscattered electrons is associated with the atomic number of the specimen. The production of both type of images, using either backscattered or secondary electrons, depend on the incident angle and divergence of the electron beam, the crystal orientation of the specimen and the static electric field and magnetic field distribution near the specimen surface. In addition to the above described two signals, there are also characteristic X-rays, Auger electrons, cathodoluminescence, transmitted electrons and specimen current arising from the beam-sample interaction.[52]

Fig. 3.11 shows the basic components of a SEM including electron gun, electromagnetic lenses, deflection system and the detectors. Many SEMs work under vacuum environment which can effectively prevent the oxidation of the electron source and the scattering of electrons from the gun to the specimen.

The electron gun is used for producing the primary high energy electrons which can be generated from thermal emission or field emission. In a thermionic source, the electrons escape from the cathode, such as tungsten or lanthanum hexaboride (LaB_6) cathodes, a filament heated to obtain the high temperature necessary to overcome the work function of the metal. They require a relatively low vacuum ambience and are cost inexpensive, but their disadvantages of short lifetime, low brightness and large energy spread, restrict the application. For modern SEMs, field emission gun (FEG) is a better choice. In a FEG, a high electron field is applied on a sharp oriented tip consisting of single crystal of tungsten, to extract the electron beam. There are three types of FEGs, cold field emission sources, thermal field emission sources and Schottky emitters sources, used in SEMs. The characteristics of different electron sources are summarized in Table 3.1. The electron beam is focused and deflected by an electromagnetic system of lenses and is scanned in a raster motion over the specimen. The rastered area can be scanned with the help of scanning coils. The electron beam interacts with the specimen, producing the various signals. The image formed with the signals (either from back-scattered or secondary electrons) can be displayed with a high magnification ratio.[53][54]

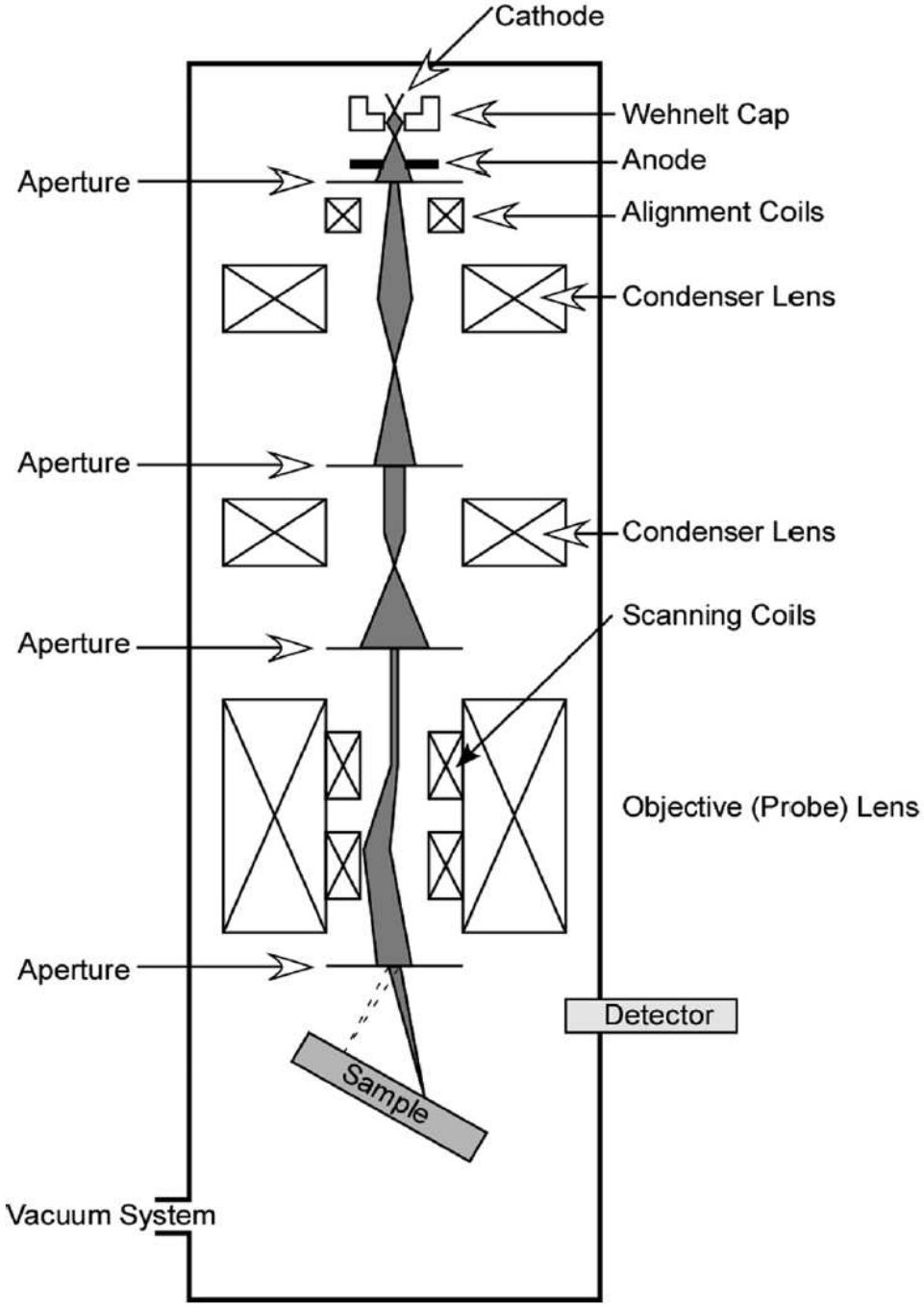

Fig. 3.11 Schematic diagram for the main components of a SEM.[54]

Table 3.1 Properties of different electron source types used in SEMs.[54]

Source type	Thermionic	Thermionic	Schottky	Cold FEG
Cathode material	W	LaB_6	W(100) + ZrO	W(310)
Work function [eV]	4.5	2.7	2.7	4.5
Tip radius [μm]	50 - 100	10-20	0.5 - 1	< 0.1
Operating temperature [K]	2800	1900	1800	300
Emission current density [A cm^{-2}]	1 - 3	20 - 50	500 - 5000	104 - 106
Total emission current [μA]	200	80	200	5
Maximum probe current [nA]	1000	1000	> 20	0.2
Normalized brightness [A cm^{-2} sr^{-1}]	104	105	107	2 × 107
Energy spread at gun exit [eV]	1.5 - 2.5	1.3-2.5	0.4 - 0.7	0.3 - 0.7

In its conceptual design SEM is similar to an optical microscope using an electron beam instead of light which permits imaging beyond Abbe's diffraction limit for light. Compared with the optical microscope, it has many advantages such as good resolution, large magnification, high depth of field and 3-D information. Unlike TEM, SEM rarely needs special specimen preparation techniques. Nevertheless, charging on the surface degrades the image and non-conductive (e.g. organic) specimens have to be coated with a very thin conducting layer (by sputtering a metal such as Au or Pd) before being examined on a SEM.

3.5.2 Transmission electron microscope (TEM)

Transmission electron microscope plays an important role in materials characterization. In TEM, a high energy electron beam strikes at an extremely thin specimen and the electron beam interacts with the specimen as it transmits through,

producing an image. The produced image is due to either absorption contrast, diffraction contrast or phase contrast. Normally, low and medium magnification images are based on diffraction contrast, while high resolution is due to phase contrast.

When the electron beam interacts with the specimen, heavy atoms of the specimen lose more energy than light atoms. It results in absorption such that different composition and thickness of the specimen appear different and contrasted in the image. When the specimen is a single crystal, a spot pattern due to the diffracted beam from a set of crystal planes will be formed. A phase contrast image can be created by the interference between at least two electron beams and these electron beams are produced by the objective lens defocus. Phase contrast contains important informations about the periodical ordered crystal structure and aperiodic characteristics and defects. For an ordered single crystal, lattice images of the crystal structure are formed through a set of lattice fringes by two electron beams. The high resolution TEM (HRTEM) is based on phase contrast.[55]

In conventional TEM (Fig. 3.12), the electron beam is generated in the electron gun by thermionic emission using tungsten cathodes or LaB_6 rods or by field emission through heating tungsten filaments. The electron beam is accelerated towards the magnetic fields of two stage condenser lenses and illuminates the specimen. After the electron beam strikes the specimen, the electrons are deflected to different degrees through a three or four stage lens system and the distribution of the electronic intensity is projected onto a fluorescent screen. The images can be recorded by a photographic film or CCD camera. In TEM, specimens must be very thin, typically, at most, hundreds of nanometers. Furthermore, special sample preparation is needed, such as cutting a thin slice of the specimen or depositing a thin film.[56]

Selected area electron diffraction (SAED) can be produced in a TEM by replacing the objective aperture with an aperture in the imaging plane. It employs a parallel high energy electron beam to form a series of two dimensional diffraction spots in the selected area of the specimen under diffraction mode. These diffraction spots arise from the specimen's crystal structure and project onto the screen the reciprocal lattice of a single crystal. SAED is one important crystallographic experimental technique for the identification of crystal structures, the determination of crystal orientations and the examination of crystal defects.[57]

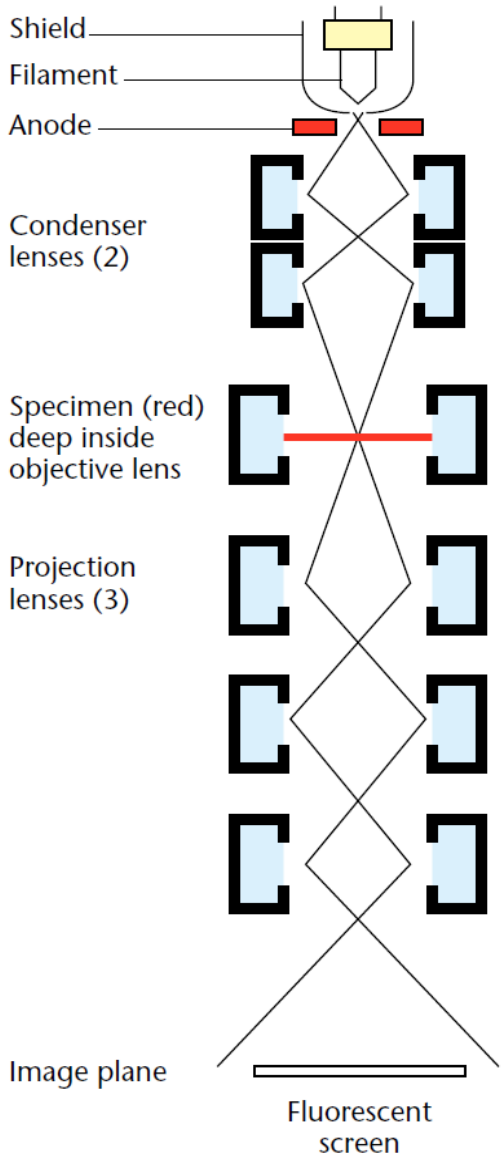

Fig. 3.12 Schematic diagram for the basic components of a TEM.[58]

3.6 Piezoresponse force microscopy (PFM)

Piezoresponse force microscopy (PFM) is an important approach for the investigation of the local piezoelectric and ferroelectric properties through imaging and controlling the nanoscale ferroelectric domains. It is achieved by applying a localized electric field bias to the sample by the way of a sharp conductive probe tip in contact with the sample surface and probing the deformation of the sample arising from the converse piezoelectric effect. With the help of a lock-in amplifier (LIA) and other instrumentations, the topography images can be recorded and even the growing of domains can be observed and studied.

In PFM, the voltage applied to the conductive probe tip in contact with a piezoelectric sample surface is

$$V_{tip} = V_{dc} + V_{ac}\cos(\omega t), \tag{3-7}$$

where V_{dc} is the switching bias voltage applied between the sample and the tip; the probing alternating current (AC) bias V_{ac}, of frequency ω, is applied to the tip resulting in deformation of the sample surface via the piezoelectric effect. The detected deflection of the tip in contact with the sample, due to the converse piezoelectric effect, is demodulated by a LIA. The tip oscillation is of the form

$$A = A_0 + A_{1\omega}\cos(\omega t + \varphi), \tag{3-8}$$

where A_0 is the surface position of the topography, $A_{1\omega}$ is the piezoelectric surface deformation at driving AC bias and φ is the corresponding phase difference. In this way, one can simultaneously record the surface topography and piezoelectric deformation. The resultant PFM magnitude image can provide information about the magnitude of the local piezoresponse, the PFM phase image can present information about the domain direction, whereas the PFM amplitude image can display both. [59]

Since Güthner and Dransfeld [60] firstly employed PFM to investigate the local domains of a ferroelectric polymer film in 1992, PFM had a rapid development and is now widely used for the ferroelectric domain imaging with the advantages of high resolution of nanometer scale, non-destruction and easy operation. The versatile applications of PFM are the following: imaging of static domain structures, poling selected areas of ferroelectric surface, observing the evolution of domain structures as a function of time and temperature, quantitatively measuring the local hysteresis loops

and thermal phenomena. Among them, the possibility of manipulation of domain structures has great potential application in memory devices.[61]

PFM is not only applied on thin films, but also on polycrystalline materials and single crystals. Recently, many ferroelectric single crystals, such as PZT, $Pb(Zn_{1/3}Nb_{2/3})O_3$-$PbTiO_3$[62][63] and $Pb(In_{1/2}Nb_{1/2})O_3$-$Pb(Mg_{1/3}Nb_{2/3})O_3$-$PbTiO_3$[64] single crystals, have been investigated by PFM to characterizate, at nanoscale, local domain structures and piezoelectric hysteresis loops.

3.6.1 The device of PFM

The scanning force microscopy (SFM) also known as atomic force microscopy (AFM) is a high-resolution kind of scanning probe microscopy (SPM) which forms a sample surface imaging using a physical probe rather than an optical or electronic probe to scan the sample. However, PFM works in a contact mode based on a standard SFM upgraded with the addition of an alternating voltage applied to the probe. On the left hand side of Fig. 3.13, that shows a schematic device of a PFM instrument, the standard parts of an SFM microscope are depicted. Based on a 4-quadrant read-out optical system, the SPM uses a sensor to measure a specified physical property at the sample surface of the sample together with *x*, *y*-coordinates to create an electronic picture of the physical topography of the sample. The right side of Fig. 3.13 describes the additional parts for PFM. The alternating voltage V_{ac} is applied to the conductive tip with the help of the function generator resulting in the oscillatory deformations of the sample and subsequently the resultant vibrations of the cantilever are read out by a LIA. The produced PFM signal contains the information about the piezoresponse of a domain and the PFM contrast normally means the difference between PFM signals as a result of various directional domains at the sample surface.[65] In our case we used a commercial setup NTEGRA Prima, shown in Fig. 3.14.

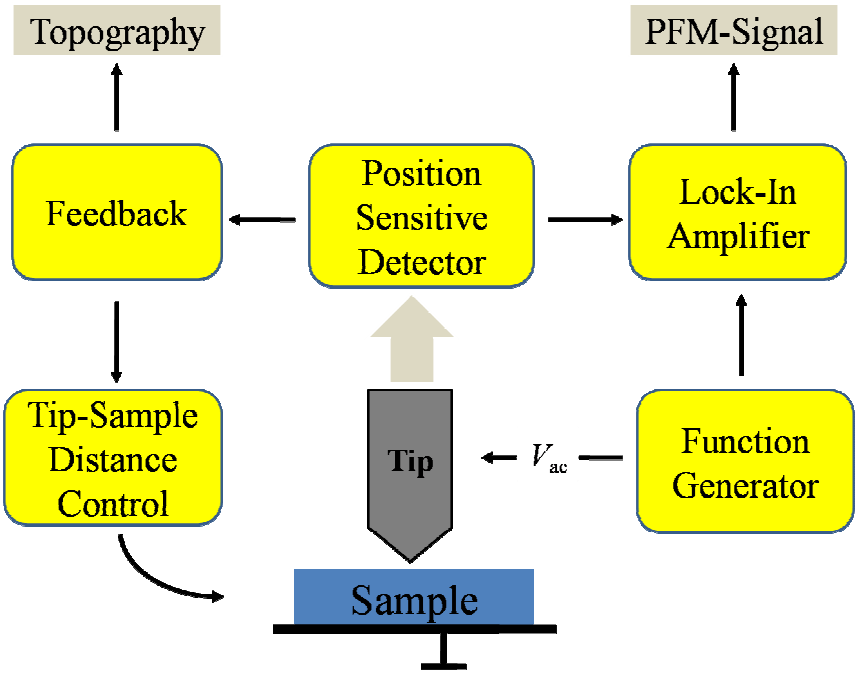

Fig. 3.13 The schematic of a PFM.[65]

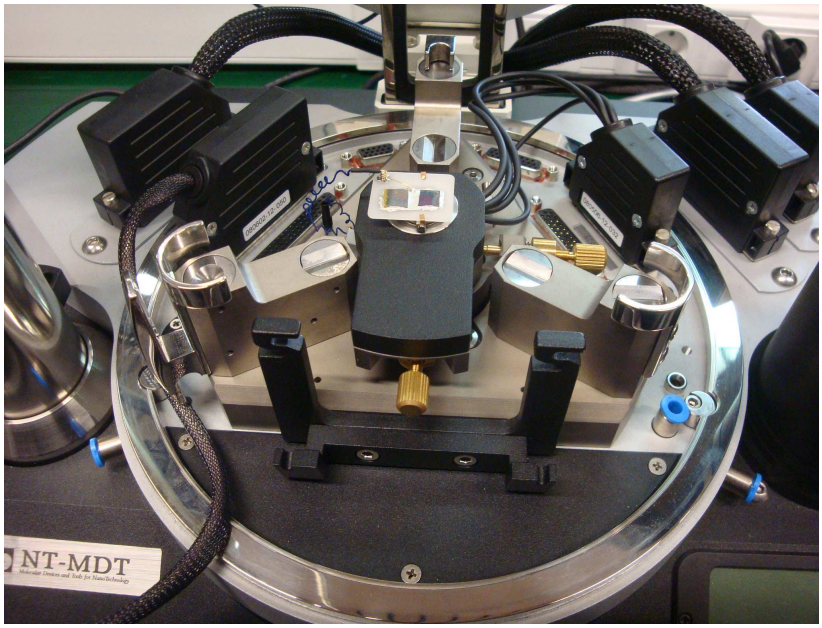

(a)

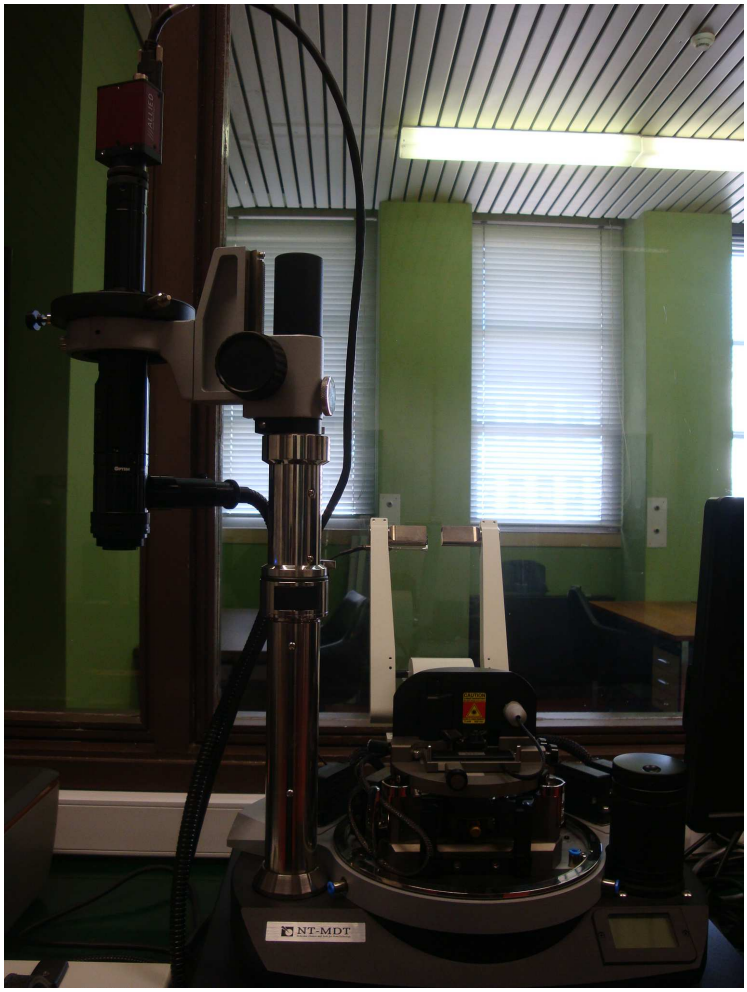

(b)

Fig. 3.14 The NTEGRA Prima -AFM/STM.

3.6.2 The concise practical guide for the settings of PFM

A concise practical guide on how to form standard PFM images will be presented, showing suitable values for alternating voltage V_{ac} (amplitude V and frequency f), the parameters of the LIA and the scanning parameters. For standard PFM operation, the frequency f of V_{ac} normally takes values in the range of 10 kHz to 100 kHz, depending on the resonance properties of the tip, while the amplitude V ranges from 1 V to 10 V. The choice of f should not disturb the simultaneous topography imaging and V determines the magnitude of the PFM signal, as the PFM signal increases with the

growing amplitude V. If measuring thick and bulk samples, V can be set as long as 10 V, while if thin films the most appropriate value is, typically, below 1 V.

Next, the choice of sensitivity, S, and the time constant, τ, parameters will be discussed. The value of the sensitivity S should be set as large as possible and the time constant τ has a relationship with the scanning parameters, that is, pixel number n, scanning speed v, and the image size $s \times s$. In theory, for the best scanning performance the value of the time constant must be as small as possible. In practice, we can choose the time constant of $\tau > \frac{5}{f}$ for a given frequency of V_{ac}, while we should choose the scanning speed within the interval $\frac{1}{3}\frac{s}{n\tau} < \upsilon < \frac{s}{n\tau}$ for a given image size and the desired pixel number. The choice of the time constant depends on the noise of the system, that is, the magnitude of the PFM signals and the instrument sensitivity also affect the choice of the time constant.

Although the typical setting of the standard PFM operation is certainly preferable for studying static domains, a faster scanning with a higher frequency of V_{ac} is required in order to record the dynamic characteristic of the domains. The frequency f of the high-frequency PFM generally ranges from 1 MHz to 10 MHz to achieve the needed temporal resolution.[65]

3.6.3 The sample surface deformation imaging

In the data reading stage of PFM, the vibrations of the cantilever are recorded to detect the deformation of the sample surface driven by the alternating voltage. Any directional, local deformation of sample surface transmits to apex of the tip and then gives rise to deflection, buckling or torsion of the cantilever. However, the corresponding driving forces (F_{delf}, F_{buck} and F_{tor}) actually act on the tip apex rather than on the cantilever (Fig. 3.15 (a)). Deflection reflects an out-of-plane deformation oriented parallel to the axis of the tip, while buckling and torsion are related to in-plane deformations normal to the tip (3.15 (b)).

The cantilever movement containing the out-of plane and two in-plane deformations are represented as the movements of the laser spot with vertical and lateral signals on the segmented photo-detector in the readout system (Fig. 3.15 (c)). The torsion is individually displayed as the lateral signal, but both deflection and buckling show up in the vertical signal. The deflection and buckling can be distinguished by detecting the same sample region at different angles, because the resultant vertical signal caused by the buckling image will be changed and that by deflection remains unchanged. Comparing the measured PFM images at 0° and 90° rotations, we can find that the PFM images arising from the buckling and torsion are exchanged with each other. If the sample is rotated by 180°, the PFM images from buckling will reverse the contrast.

In theory, we can differentiate the PFM signal caused by in-plane and out-of-plane deformation by rotating the same sample region by 0°, 90° and 180°. In practice, it is not easily to operate the rotation of the sample as the axis of rotation is located underneath the tip within a few micrometres.[65]

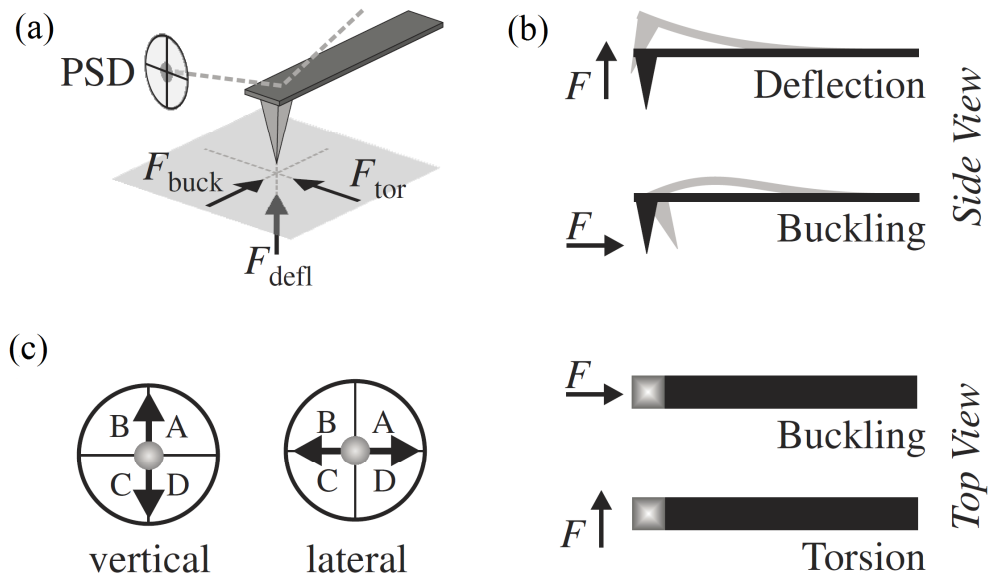

Fig. 3.15 (a) The various forces caused by the deformation of sample surface applied to the tip. The position sensitive detector is referred as PSD. (b) The cantilever movements include deflection (F_{delf}), buckling (F_{buck}) and torsion (F_{tor}). (c) F_{delf} and F_{buck} give rise to the vertical signals of laser spots, while F_{tor} leads to the lateral signals of laser spots.[66]

3.6.4 The experimental results of PFM

Through the demodulation of the LIA, the result of measurement can be expressed in two forms: magnitude and phase (R, Θ) or two amplitudes (X, Y). They are related by $X = R\sin\Theta$ and $Y = R\cos\Theta$, similar to the relationship between polar and Cartesian coordinates. In addition, let us suppose that a domain sample possesses the piezoresponse d. The X output signal of the LIA provides full information about a PFM signal, while the Y output signal is related to the background or electronic noise of SFM. As in the literature the phase and magnitude images are shown and used for investigation, we will discuss the difference of the various output signals of the LIA in PFM imaging (Fig. 3.16).

The piezoresponse of the sample dependence of the alternating voltage V_{ac} must generate in phase or 180° out of phase signals according to the polarization direction, at least when the frequency f is lower than 100 kHz. Therefore, even if the polarization vector with a certain angle ϕ (Fig. 3.16 (a)) normal to the surface is not strictly perpendicular to the surface, the phase Θ output of LIA can only generate two values of 0° and 180°, representing the polarization vector of the domain. The amplitude X of the LIA output regarding the piezoresponse can be expressed as $d_{i,j}\cos\phi$, containing the information about the phase and the magnitude R which represents the displacement at the sample surface $\left|d_{i,j}\cos\phi\right|$. Fig. 3.16 (b) shows the typical PFM signals of the LIA output arising from the domains with different polarization orientations. We can find that the magnitude R and phase Θ output are all combined into the information of the X output, as explained above. The Y output signal would ideally display a horizontal line without any information.[65]

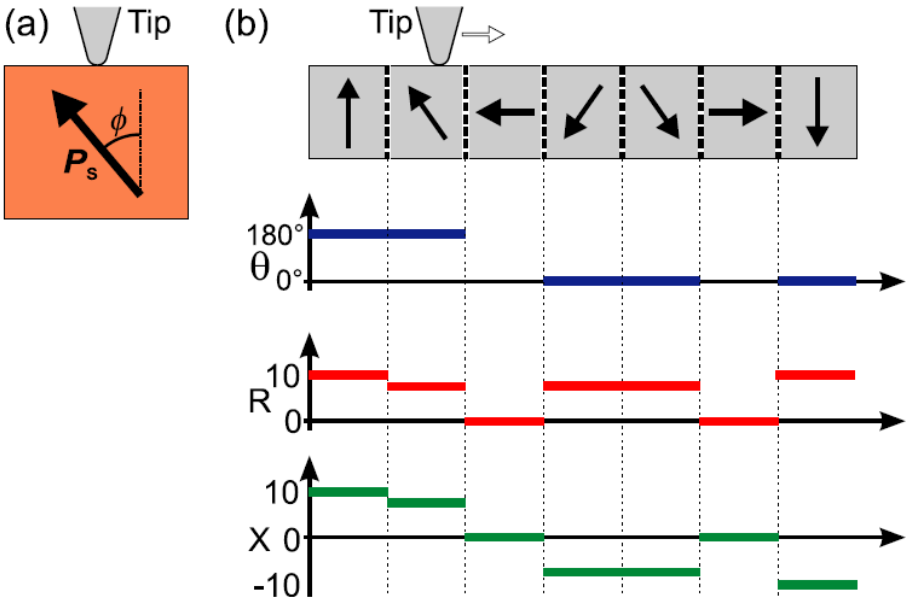

Fig. 3.16 (a) There is an angle ϕ between the polarization vector of a domain and the sample surface. (b) The different orientations of the polarization vector are displayed as Phase Θ, magnitude *R* and amplitude *X* of PFM signals.[65]

Chapter 4

Crystal growth and characterization of $BiInO_3$-$PbTiO_3$ single crystals

4.1 Experimental Procedure

$BiInO_3$-$PbTiO_3$ (BIPT) single crystals were grown by the high temperature solution method using Pb_3O_4 and Bi_2O_3 as self-flux. The starting materials Pb_3O_4 (99%), Bi_2O_3 (99.99%), In_2O_3 (99.99%) and TiO_2 (99%) high-purity powders were weighed according to xBiInO$_3$-(1-x)PbTiO$_3$ with x = 0.3, 0.4 and 0.5, stoichiometrically. Sintered BIPT polycrystalline materials and the flux materials Pb_3O_4 and Bi_2O_3 in the ratio of 7 : 3 were loaded into alumina crucibles, which were sealed by an alumina lid to minimize the evaporation of the flux. The growth was carried out in a muffled furnace. The materials were heated to 1100 ^{o}C and held at this temperature for 7 h, followed by slow cooling (1 - 6 ^{o}C/h) to 650 ^{o}C. The crucible was then cooled to room temperature inside the furnace by switching off the furnace. The as-grown crystals were light brown in color and rectangular in shape, being millimeter in size. The grown crystals xBiInO$_3$-(1-x)PbTiO$_3$ with x = 0.3, 0.4 and 0.5 (BIPT03,

BIPT04 and BIPT05, respectively) are shown in Fig. 4.1. The main advantage of this technique using Pb_3O_4 and Bi_2O_3 as flux is that no unfavorable additional cations were brought into the system.

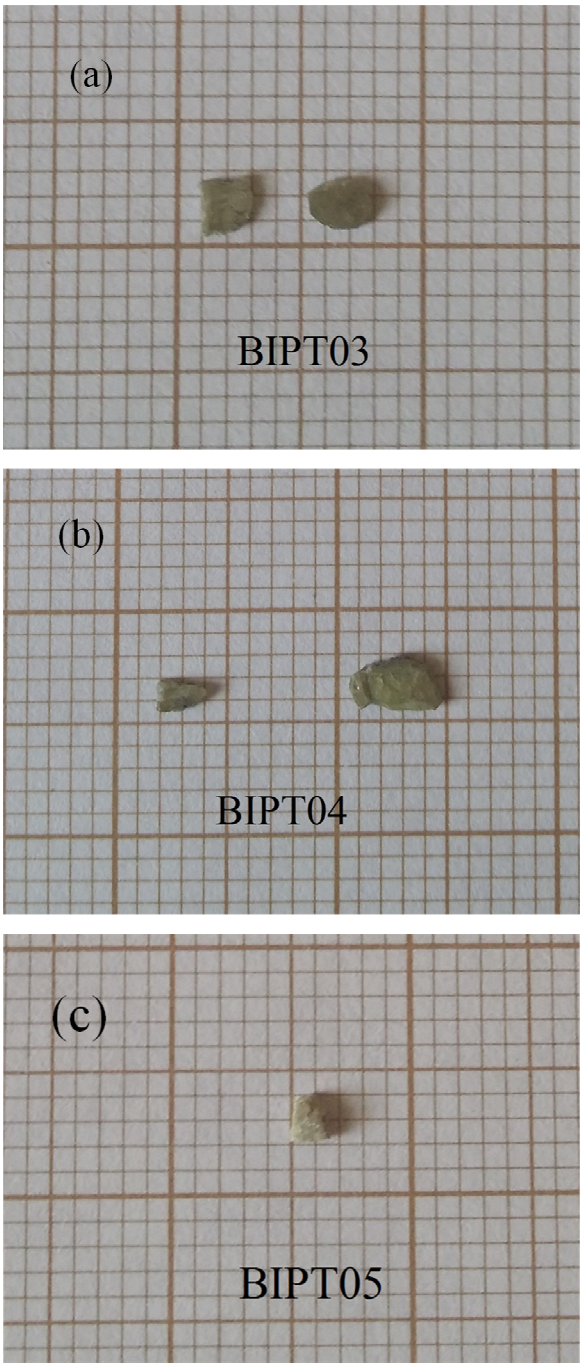

Fig. 4.1 Crystals of BIPT03, BIPT04 and BIPT05 on a 1 mm grid.

4.2 Results and discussion

4.2.1 Crystal structure of BIPT03, BIPT04 and BIPT05 at room temperature

The X-ray powder diffraction data of BIPT, which were obtained by grinding a few single crystals, were performed on a Bruker D8 Advance X-ray diffractometer (XRD) with Cu K_α radiation in a 2θ range of 10-135° with a scanning step of 0.01^o and a counting time of 19.2s per step. The crystal structure was analyzed by the Rievteld method with GSAS 2000[67]. All measurements were carried out at room temperature.

The X-ray powder diffraction patterns of BIPT03, BIPT04 and BIPT05 are shown in Fig. 4.2. Comparing the XRD patterns of BIPT with those of $PbTiO_3$ (ICSD-61168[68]), it can be seen that their X-ray diffraction patterns are similar and no additional peaks were found, which showed that they are isomorphic, namely, BIPT has a tetragonal perovskite structure with space group *P*4*mm* (No. 99). It has also been observed that there is a little shift in the peak positions of substituted compounds, which is due to the corresponding minor change in unit cell parameters. The diffraction patterns are shifted to lower angles with increasing Bi^{3+} and In^{3+} doping. To further analyze the structural changes, the diffraction data of BIPT03, BIPT04 and BIPT05 were refined by the Rietveld method starting from the parent structural data of $PbTiO_3$ (ICSD-61168). The experimental and fitted XRD patterns of BIPT03, BIPT04 and BIPT05 are shown in Fig. 4.3, and the fitting residuals R_{wp} and R_p for BIPT are 12.33% and 8.92% for BIPT03, 10.27% and 7.82% for BIPT04 and 9.25% and 7.03% for BIPT05, respectively. It can be seen that the position and intensity of calculated and experimental peaks are very well consistent with each other. The refined lattice parameters are summarized in Table 4.1. It can be seen that the lattice parameters, cell volume and density of BIPT are increasing with the dopant Bi^{3+} and In^{3+} content. This is consistent with the trend of diffraction patterns of the Fig. 4.2. The atom coordinates (x, y and z), isotropic temperature factor U_{iso} and the occupancy of atom sites are summarized in Table 4.2. Suitable constraints in position, site

occupancies and isotropic temperature factors were applied in the refinement for ions sharing the same site, such as Bi^{3+} substituting for Pb^{2+} and In^{3+} substituting for Ti^{4+}. BIPT03, BIPT04 and BIPT05 have similar atom coordinates. Since the ionic radius of Bi^{3+} is smaller than that of Pb^{2+}, the ionic radius of In^{3+} is bigger than Ti^{4+}, bond lengths and angles of BIPT have changed, as shown in Table 4.3 and Fig. 4.4, which shows the structural model of BIPT obtained by Rietveld refinement. One of the striking features of the tetragonal phase of BIPT is the large difference between the two Ti-O1 distances. It corresponds to an octahedral distortion along the four-fold axis either compression or stretching. Fig. 4.5 shows the octahedral distribution of oxygens bonding with Ti/In, showing the four-fold axis (C_4) and the deformation angle ϕ. With the variation of dopant In^{3+}, in the acentric 4*mm* (polar) room temperature phase, the bonds with oxygen atoms have bended by $\delta\phi = 11.8020^o$ ($\phi = 101.8020^o$ in BIPT03), $\delta\phi = 9.8430^o$ ($\phi = 99.8430^o$ in BIPT04) and $\delta\phi = 7.9275^o$ ($\phi = 97.9275^o$ in BIPT05). The four oxygen O2 atoms in Fig. 4.5 get closer to the lead atom, becoming more covalent and the lead orbitals become rehybridized, as some of the 6*s* orbital is used for the bonding interaction. This distortion can be ascribed to the lone pair of electrons on the Pb atom. [69] Ronald E. Cohen [70] demonstrated that the hybridization of the electron states between B-site cation and O anion is necessary for ferroelectricity in most ferroelectric ABO_3-type perovskites. Specifically, in $PbTiO_3$, its hybrid state between Ti-3*d* and O-2*p* contributes to the formation of the tetragonal phase and an additional hybrid state between Pb cation and O anion induces a large strain that contributes to the stabilization of the tetragonal phase. In $PbTiO_3$, the lowest occupied electron states in Ti cations are *d*-states. This allows for *d*-hybridization with O in a d^2sp^3-type hybridization that softens the Ti-O repulsion. In BIPT, the lowest unoccupied states of In cations are *s*-states, and exhibit a sp^3d^2-type of hybridization that should weaken the octahedral distortion in comparison with d^2sp^3 hybridization as well as the Pb/Bi-O bonding interaction. Also, the smaller covalent radius of Bi^{3+} compared with Pb^{2+}, leads to a larger strain in BIPT.

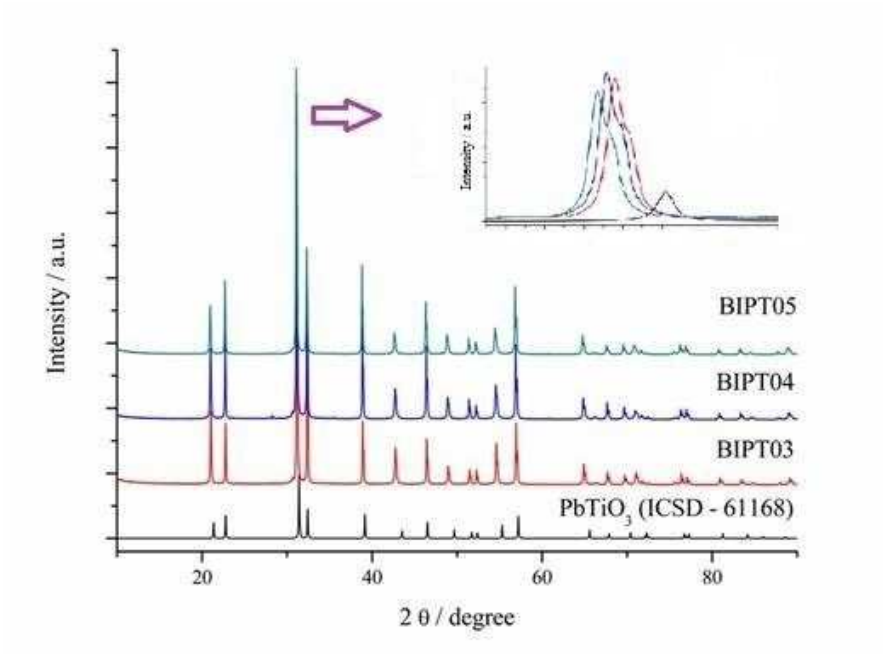

Fig. 4.2 The X-ray powder diffraction patterns of BIPT03, BIPT04 and BIPT05. The inset shows a detail of region of the most intense peak around ~ 31°.

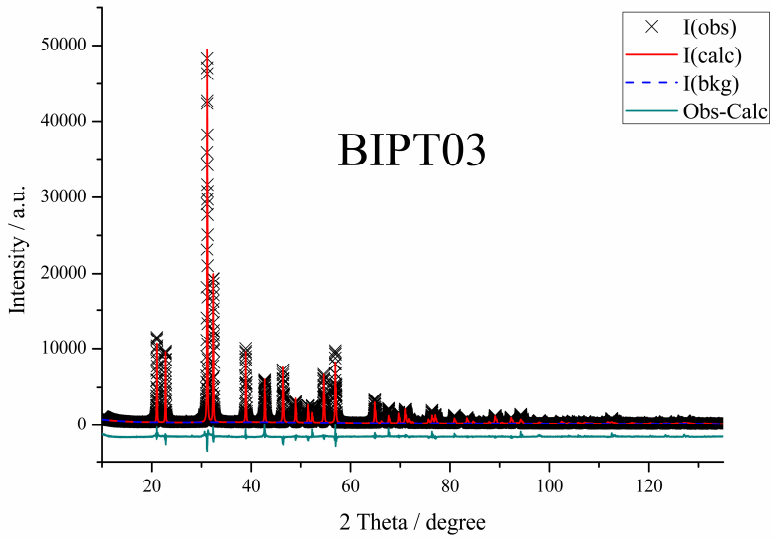

(a)

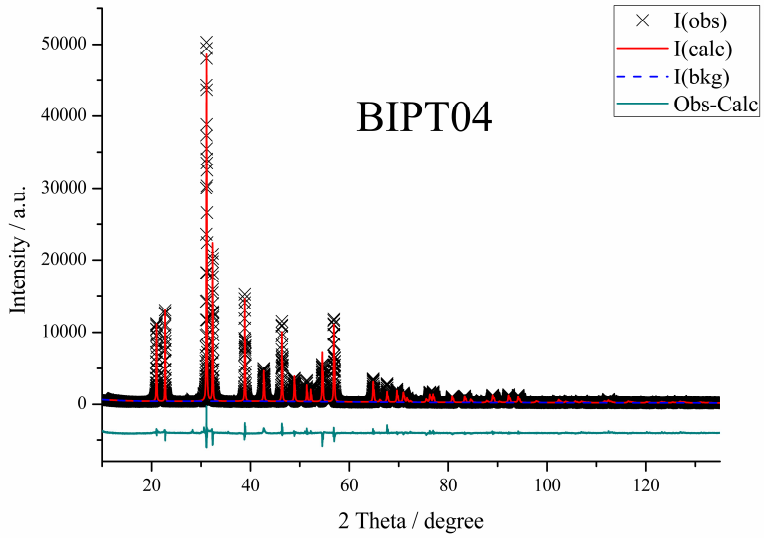

(b)

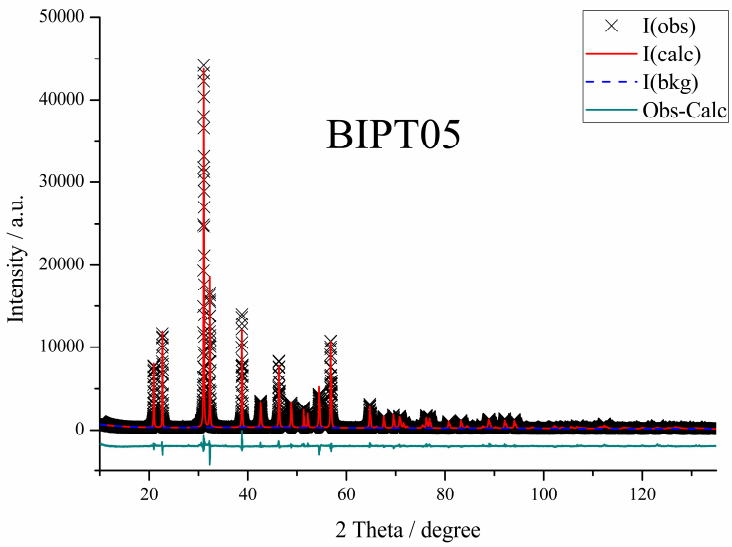

(c)

Fig. 4.3 Experimental, fitted curves of XRD of BIPT03 ((in fig (a)) / BIPT04 (in fig (b)) / BIPT05 (in fig (c)) crystalline powder are shown by crosses and solid curves, respectively. The bottom curves are differences between experimental and fitting values.

Table 4.1 Lattice parameters of BIPT03, BIPT04, BIPT05 and $PbTiO_3$ (ICSD-61168).

	a and *b* (Å)	*c* (Å)	*α*, *β* and *γ* (°)	Cell volume ($\times 10^6$ pm^3)	density (gm/cm^3)
$PbTiO_3$	3.902 (3)	4.156 (3)	90	63.28	--
BIPT03	3.914752(23)	4.23302(4)	90	64.8720(10)	8.276
BIPT04	3.917306(17)	4.23622(4)	90	65.0060(10)	8.529
BIPT05	3.919153(16)	4.241700(35)	90	65.1520(10)	8.766

Table 4.2 Fractional coordinates (*x*, *y* and *z*), U_{iso} of all atoms of BIPT with space group *P*4*mm* and occupancy of atom site, obtained from Rietveld refining.

	Atom (Wyckoff site, symmetry)	(*x*, *y*, *z*)	U_{iso}	Occupancy
BIPT03	Pb/Bi (1*a*, 4*mm*)	(0.0, 0.0, 0.00018)	0.03720	0.69252/0.29252
R_{wp}=12.33%	Ti/In (1*b*, 4*mm*)	(0.5, 0.5, 0.53438)	0.05889	0.71678/0.31678
R_p=8.92%	O1 (1*b*, 4*mm*)	(0.5, 0.5, 0.10126)	0.02073	1.0
	O2 (2*c*, 2*mm*)	(0.0, 0.5, 0.631)	0.19410	1.0
BIPT04	Pb/Bi (1*a*, 4*mm*)	(0.0, 0.0, -0.03692)	0.03829	0.62369/0.42369
R_{wp}=10.27%	Ti/In (1*b*, 4*mm*)	(0.5, 0.5, 0.51915)	0.04210	0.55987/0.35987
R_p=7.82%	O1 (1*b*, 4*mm*)	(0.5, 0.5, 0.06229)	0.02066	1.0
	O2 (2*c*, 2*mm*)	(0.0, 0.5, 0.59937)	0.02623	1.0
BIPT05	Pb/Bi (1*a*, 4*mm*)	(0.0, 0.0, -0.01034)	0.03254	0.5514/0.5514
R_{wp}=9.25%	Ti/In (1*b*, 4*mm*)	(0.5, 0.5, 0.53377)	0.03523	0.4084(10)/0.4084(10)
R_p=7.03%	O1 (1*b*, 4*mm*)	(0.5, 0.5, 0.14571)	0.02343	1.0
	O2 (2*c*, 2mm)	(0.0, 0.5, 0.5981)	0.05165	1.0

Table 4.3 Bond lengths and angles of framework geometry in BIPT.

		BIPT03	BIPT04	BIPT05
Bond Lengths (Å)	Pb/Bi-O1	2.801020(20)	2.801650(10)	2.849210(10)
	Pb/Bi-O2	2.504690(10)	2.492040(10)	2.568770(10)
	Ti/In-O1	1.833400(20) 2.399620(20)	1.935360(20) 2.300860(20)	1.646000(10) 2.595700(20)
	Ti/In-O2	1.999650(10)	1.987920(10)	1.978480(10)
Angles (^{o})	O2-Pb/Bi-O2	102.7931(6) 67.09000(30)	103.6195(5) 67.52600(30)	99.4316(5) 65.28750(30)
	O1-Ti/In-O2 (ϕ)	101.80220(10)	99.84300(10)	97.92750(10)
	O2 –Ti/In - O2	156.39571(30) 87.60240(10)	160.3139(20) 88.3253	164.14500(10) 88.91

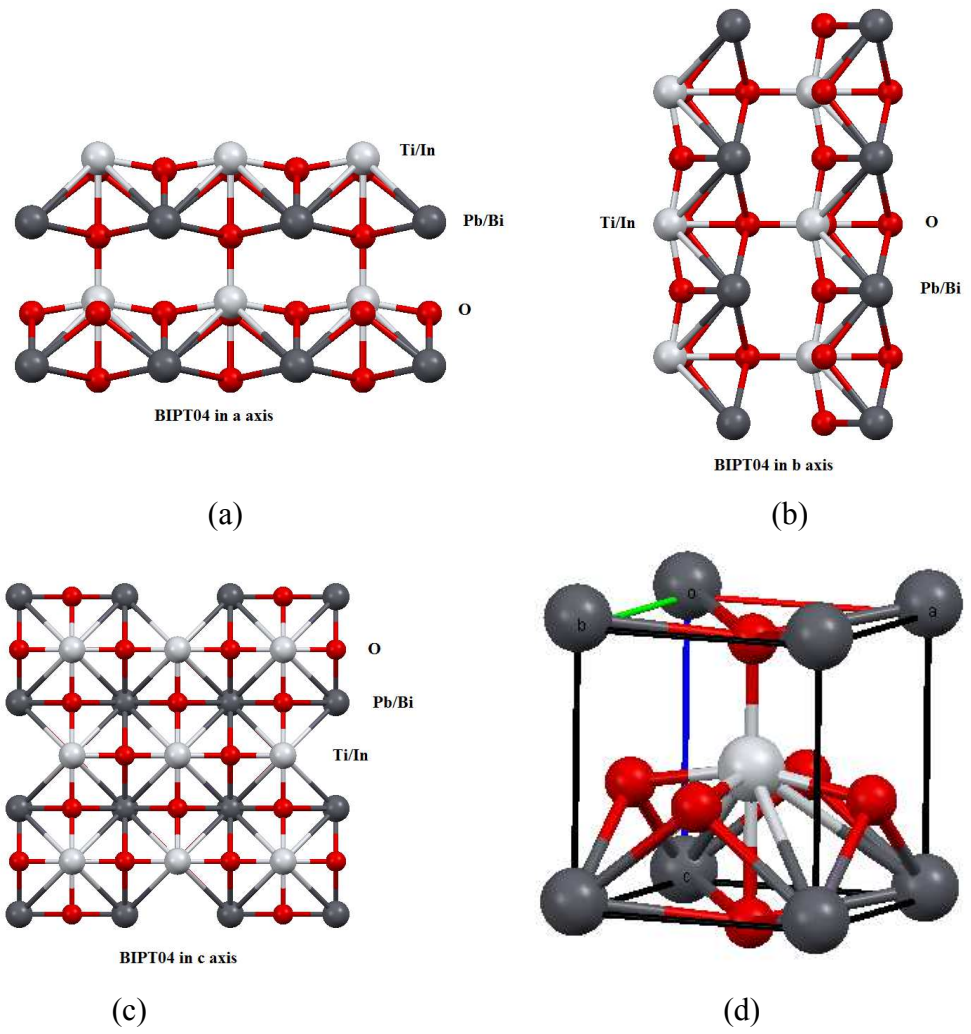

Fig. 4.4 Refined structural model of BIPT view in *a* axis (in fig. (a)), in *b* axis (in fig. (b)), in *c* axis (in fig. (c)), and the unit cell (in fig. (d)).

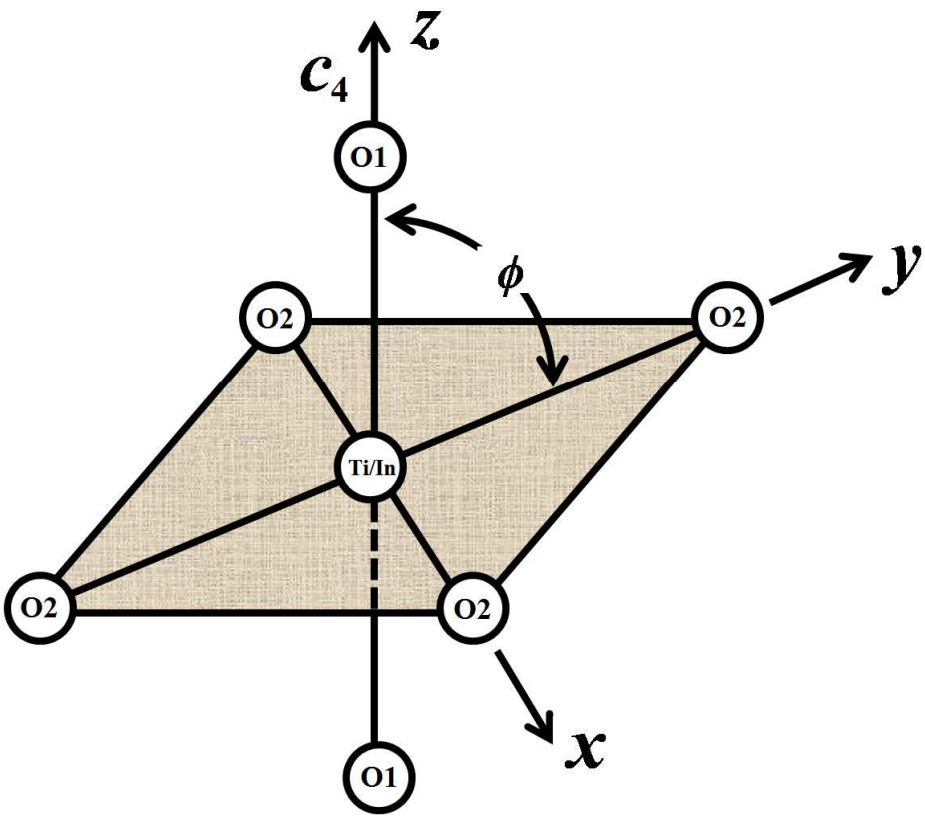

Fig. 4.5 Octahedral distribution of oxygen atoms about Ti/In in the BIPT showing the four-fold axis (C_4) and the deformation angle ϕ.

4.2.2 Crystal structure of BIPT03 at high temperature

The high-temperature X-ray powder diffraction (HT-XRD) of BIPT03, which were obtained by grinding single crystals, were performed on an X-ray diffractometer of MPD X'Pert Philips model (University of Aveiro) with Cu K_α in a 2θ range of 5-50° at a scanning step of 0.02^o. During HT-XRD experiments, the temperature was held constant in the range from room temperature up to 700 ^{o}C.

Because the splitting of the X-ray diffraction peaks is a signature of symmetry changes, the thermal evolution of the XRD patterns are discussed as follows. Fig. 4.6 shows the high temperature XRD patterns of the BIPT03 up to 700 ^{o}C, which

demonstrate a transition from a tetragonal ABO_3 perovskite-type structure to a cubic ABO_3 perovskite-type of structure. In the high-symmetry cubic phase, no reflections are split. In the tetragonal phase, (111) remains a single peak whereas the (100) reflection is gradually divided into (001) and (100) peaks with an intensity ratio of 1:1, the (110) reflection is gradually split into (101) and (110) peaks, the (200) reflection is gradually divided into (002) and (200) peaks. The (001)/(101)/(002) reflections shifts to a lower 2θ value, and the (100)/(110)/(200) reflections correspondingly shifts to a higher 2θ value. The cubic perovskite structure of BIPT03 was kept unchanged in the 600 ^{o}C / 700 ^{o}C diffractograms and no additional diffraction peaks appear, which indicates the absence of another phase transformation and /or decomposition of the perovskite structure in this temperature range.

To clearly observe the evolution of structure with temperature, all HT-XRD data were analyzed in order to extract tetragonal or cubic lattice parameters. Table 4.4 and Fig. 4.7 show the values of *a* and *c* cell parameters at each temperature. We can find that *a* and *c* cell parameters regularly change with increasing temperature and merge at 600 ^{o}C, showing a phase transition process from a tetragonal to a cubic structure.

Table 4.4 The evolution of the lattice parameters with various temperatures in BIPT03.

	Space group	Lattice parameter (Å)		Tetragonal strain *c*/*a*
25 ^{o}C	Tetragonal	*a*=3.90(3)	*c*=4.22(3)	*c*/*a*=1.08(1)
200 ^{o}C	Tetragonal	*a*=3.92(3)	*c*=4.18(3)	*c*/*a*=1.06(1)
300 ^{o}C	Tetragonal	*a*=3.93(4)	*c*=4.15(4)	*c*/*a*=1.05(1)
400 ^{o}C	Tetragonal	*a*=3.94(4)	*c*=4.12(4)	*c*/*a*=1.04(1)
500 ^{o}C	Tetragonal	*a*=3.93(1)	*c*=4.08(1)	*c*/*a*=1.03(0)
550 ^{o}C	Tetragonal	*a*=3.97(3)	*c*=4.05(3)	*c*/*a*=1.02(1)
555 ^{o}C	Tetragonal	*a*=3.97(3)	*c*=4.05(3)	*c*/*a*=1.02(1)
560 ^{o}C	Tetragonal	*a*=3.97(3)	*c*=4.05(3)	*c*/*a*=1.02(1)
565 ^{o}C	Tetragonal	*a*=3.97(3)	*c*=4.04(3)	*c*/*a*=1.01(1)
570 ^{o}C	Tetragonal	*a*=3.97(3)	*c*=4.04(3)	*c*/*a*=1.01(1)
600 ^{o}C	Cubic	*a*=3.99(2)		*c*/*a*=1.00(0)
700 ^{o}C	Cubic	*a*=4.00(1)		*c*/*a*=1.00(0)

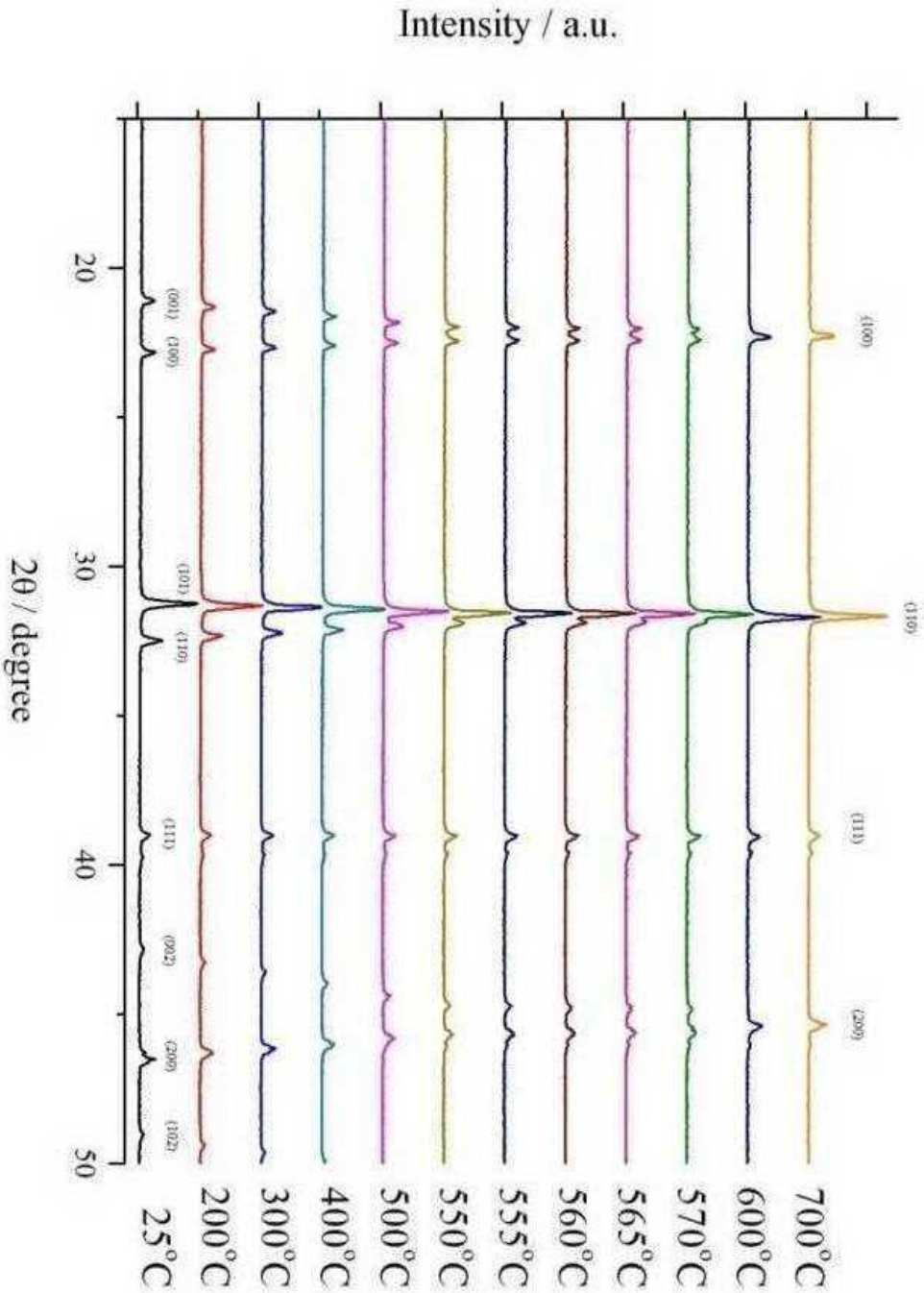

Fig. 4.6 The high temperature X-ray powder diffraction patterns of BIPT03.

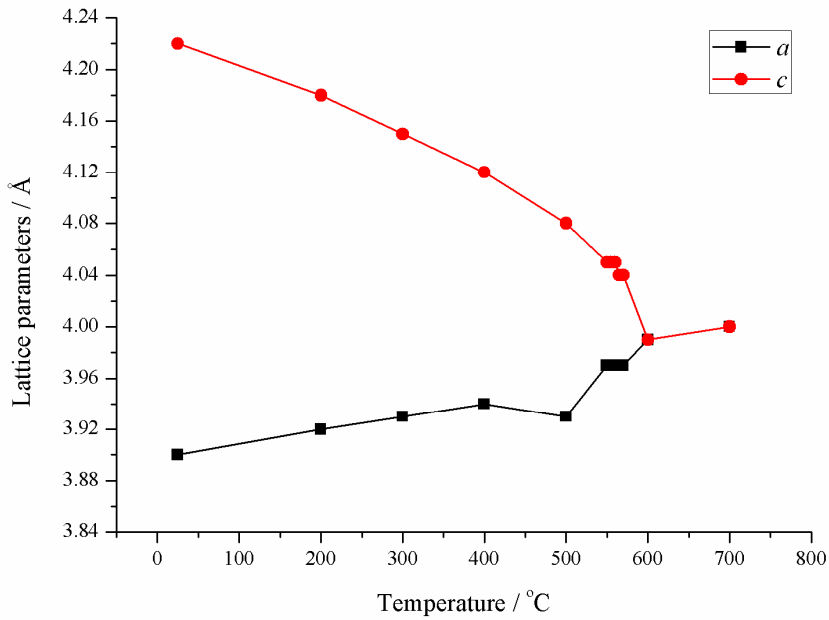

Fig. 4.7 Lattice parameters versus temperature for BIPT03 over the whole range of temperatures from 25 to 700 °C showing the evolution from the tetragonal phase to the cubic phase.

4.2.3 The chemical composition of the BIPT03, BIPT04 and BIPT05 the vibration modes of BIPT03 and BIPT04

To check the chemical composition of BIPT single crystals, we used dispersive X-ray energy dispersion spectrometry (EDS) and X-ray fluorescence spectroscopy (XRF). The XRF analysis was performed on a HITACHI, SEA6000VX-Hsfinder X-ray fluorescence spectrometer. Fig. 4.8 shows the spectra of BIPT03, BIPT04 and BIPT05 measured in air, and, for the lower energy end of the spectra, measured in helium. The XRF analysis confirms that BIPT single crystals contain Pb, Bi, Ti, and In elements. Because of lack of the internal standard substances for the XRF measurement, the analysis is not quantitative, but only qualitative. Fig. 4.9 shows the composition ratio of Bi : Pb and In : Ti in BIPT03, BIPT04 and BIPT05 as measured by XRF. It shows that Bi or In concentrations in the grown crystals were smaller than

the initial stoichiometry in the starting materials. However, the concentrations of Bi/In in the single crystals increase the order of that in BIPT03, BIPT04 and BIPT05. The chemical composition of BIPT single crystals was determined by energy dispersion spectrometry (EDS) technique. The concentrations of Bi^{3+} ions and In^{3+} in the crystal BIPT03 and BIPT04 were both 25.58 at% and 8.77 at%.

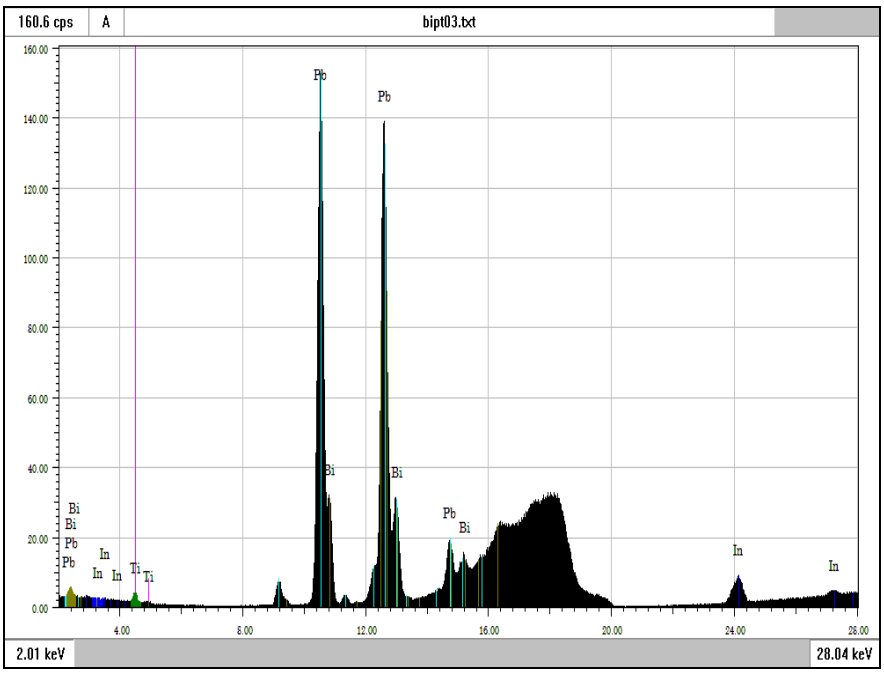

(a)

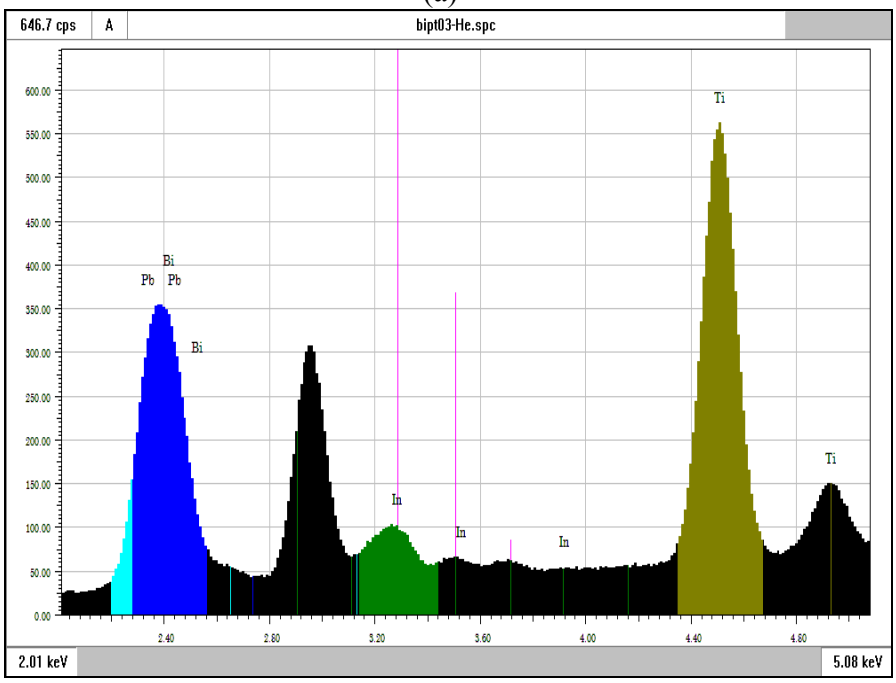

(b)

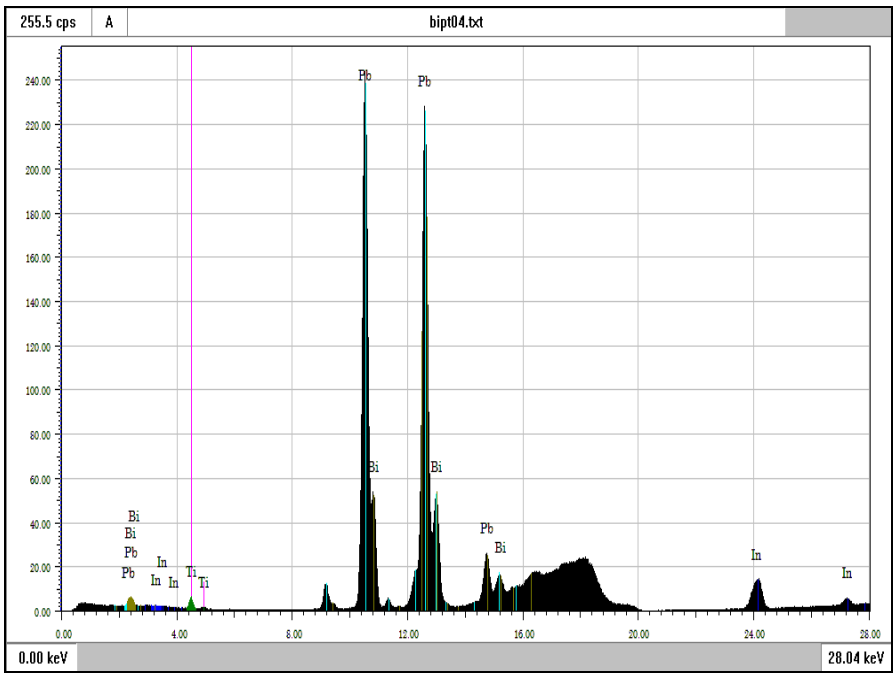
255.5 cps
A
bipt04.txt
Pb
Pb
Bi
Bi
Bi
Bi
Pb
Pb
In
In
In
Ti
Ti
Pb
Bi
In
In
0.00 keV
28.04 keV

(c)

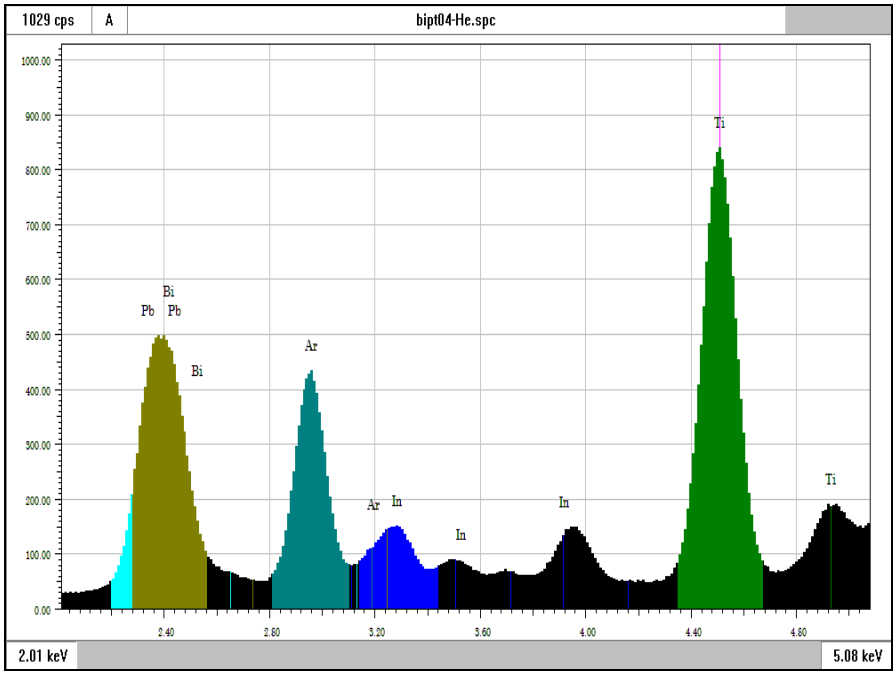
1029 cps
A
bipt04-He.spc
Pb
Bi
Pb
Bi
Ar
Ar
In
In
In
Ti
Ti
2.01 keV
5.08 keV

(d)

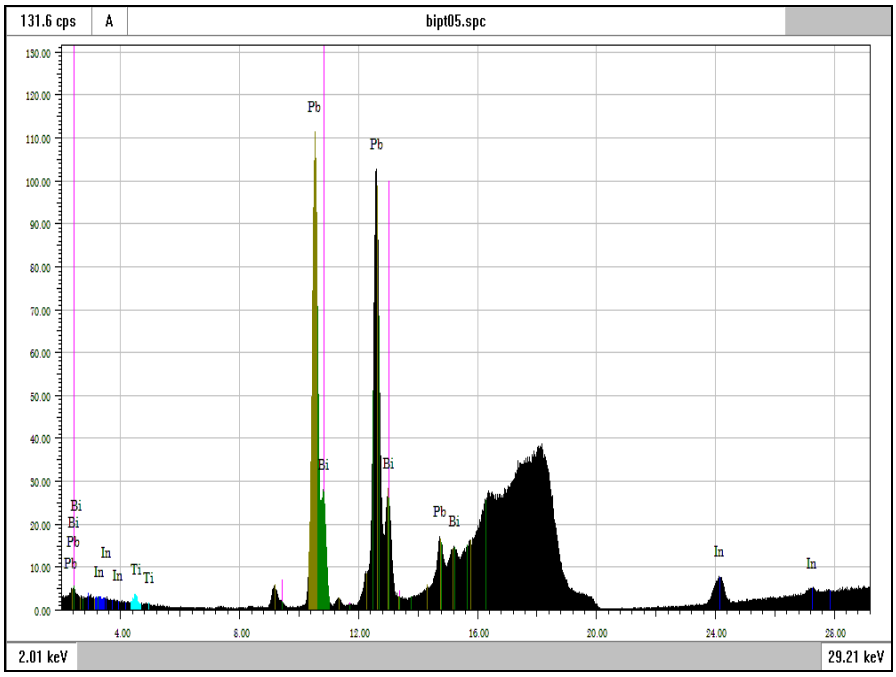

(e)

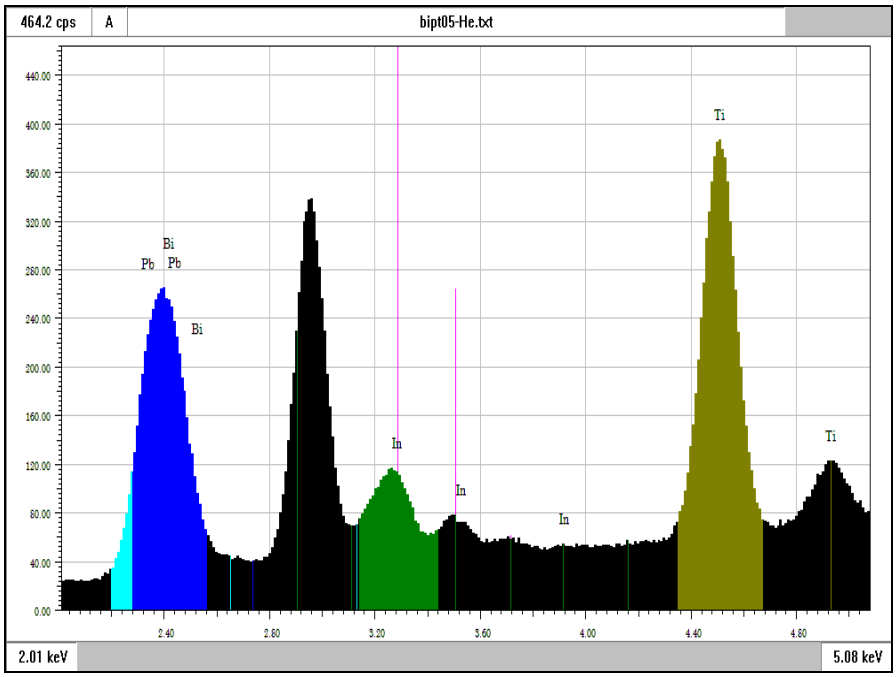

(f)

Fig. 4.8 The spectrum of BIPT03, BIPT04 and BIPT05 single crystals in air (in (a), (c) and (e), respectively) and in Helium (in (b), (d) and (f), respectively) measured by XRF.

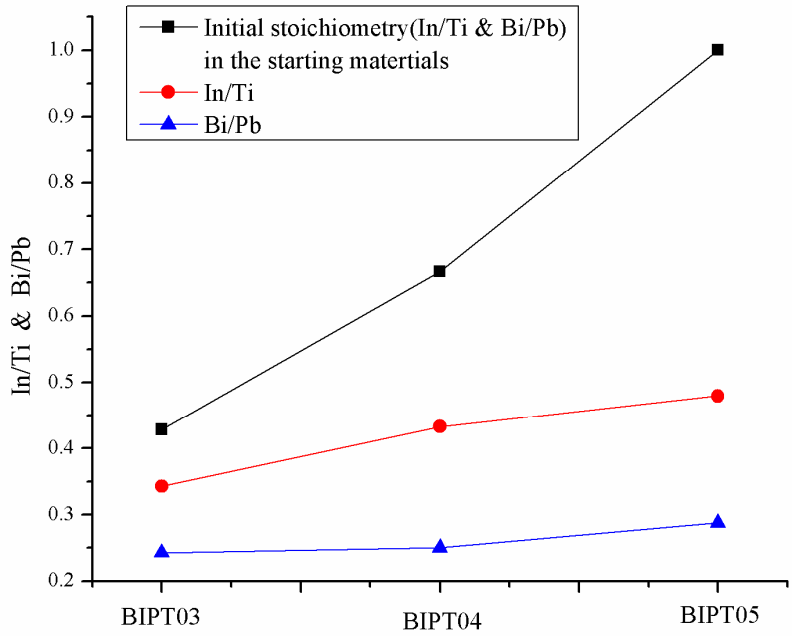

Fig. 4.9 The composition ratio of Bi : Pb and In : Ti in the BIPT03, BIPT04 and BIPT05, measured in XRF.

Fourier transform infrared spectroscopy (FTIR) spectra of BIPT03 and BIPT04 were recorded with a Thermo Scientific Nicolet 380 (Department of Chemistry of University of Coimbra) equipped with a Smart Orbit Diamond ATR (Thermo Scientific) to measure their vibrational modes. Each spectrum was the average of two independent measurements with 32 scans at a resolution of 1 cm^{-1}. The FTIR absorption bands at 553 and 739/734 cm^{-1} in BIPT03/BIPT04 in Fig. 4.10 are in close agreement with the reported data for Ti-O and Pb-O stretching modes, respectively.[71] It shows that the Ti-O and Pb-O stretching modes vibration exist with very similar frequencies in the BIPT03 and BIPT04.

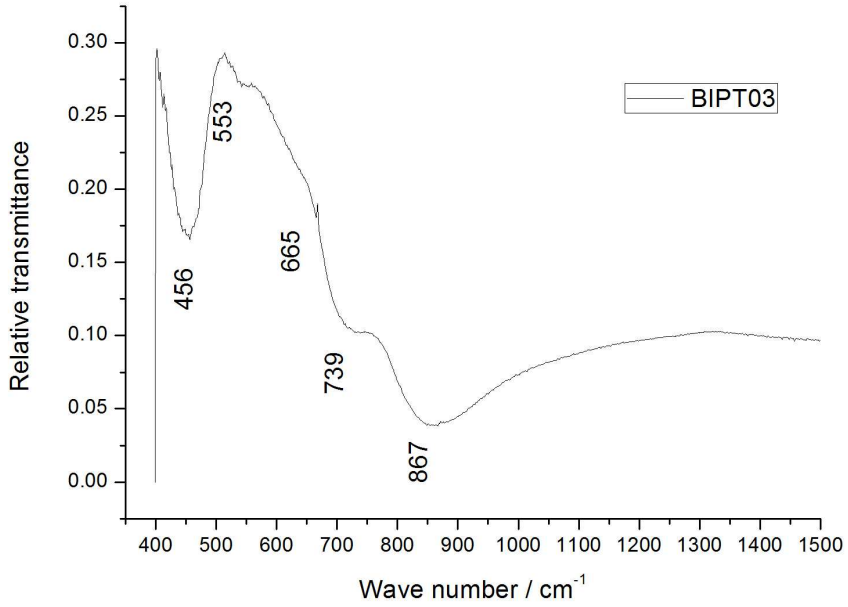

(a)

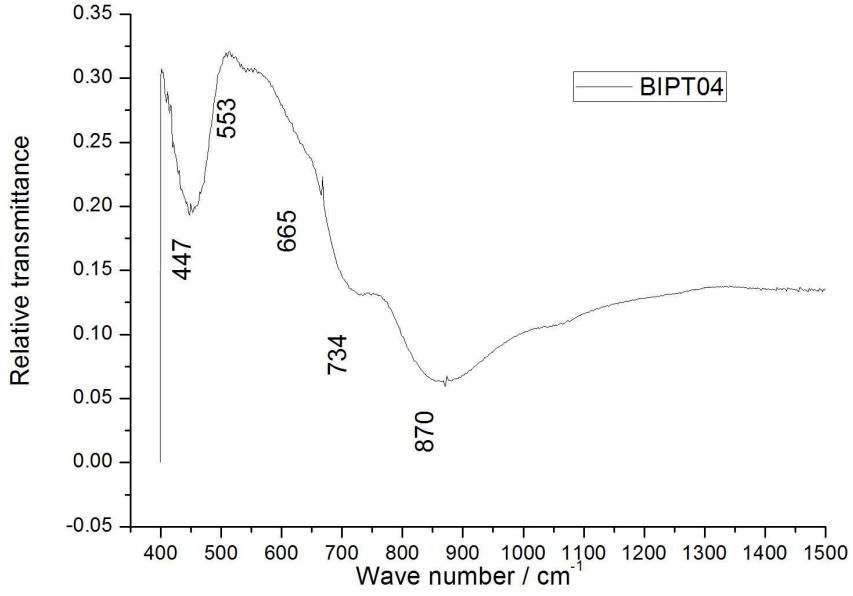

(b)

Fig. 4.10 The FTIR spectra of BIPT03 and BIPT04 single crystals in (a) and (b), respectively.

4.2.4 Thermodynamics of BIPT03, BIPT04 and BIPT05 single crystals

The differential scanning calorimetry (DSC) curves were recorded on a Perkin Elmer STA 6000 in nitrogen, in the temperature interval 50 to 750 °C, at a heating rate of 5 °C/min using 31.785 mg of sample BIPT03, 27.807 mg of sample BIPT04 and 15.484 mg of sample BIPT05. The temperature variations of heat flow of these samples are shown in Fig. 4.11. Endothermic peaks were observed in the DSC curves, which arise from the ferroelectric phase transition. The onset of endothermic peaks of BIPT03, BIPT04 and BIPT05 is associated with Curie temperatures at 555, 556 and 558 ^{o}C, respectively. Table 4.5 shows the ferroelectric phase transition temperatures, the tetragonal distortion (c/a) at room temperature and enthalpy changes. The Curie temperatures were found to increase as the substitution concentration increases. Fig. 4.12 shows the Curie temperature relationship with c/a at room temperature for BIPT samples shown in Table 4.5 and for other Bi*Me*O_3-$PbTiO_3$ samples shown in Table 1.2. It can be observed that although for most materials the Curie temperature increases with the c/a ratio, there are notable exceptions. However, in the BIPT system, the Curie temperature does always increase with the c/a tetragonal distortion.

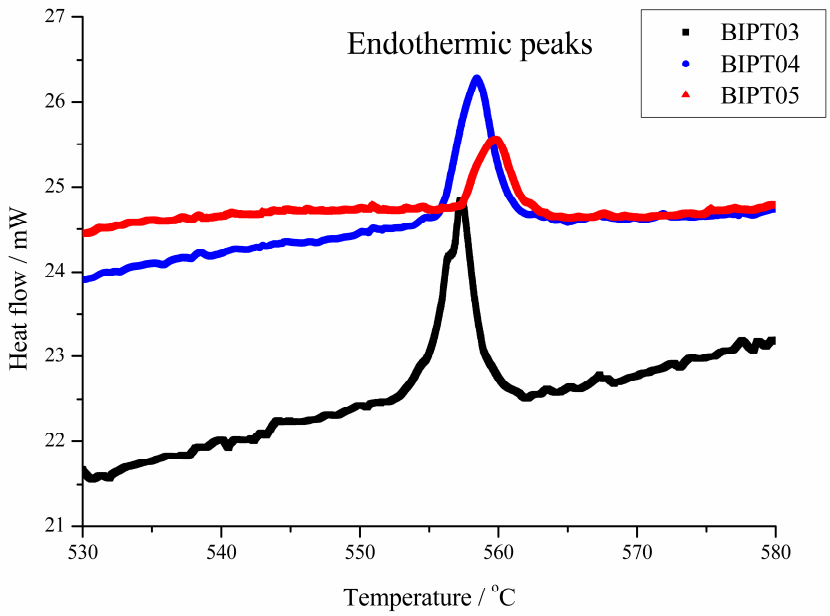

Fig. 4.11 The heat flow vs temperature (DSC trace) for BIPT

Table 4.5 The ferroelectric phase transition temperatures, the room temperature tetragonal distortion (*c*/*a*) and enthalpy of BIPT.

	BIPT03	BIPT04	BIPT05
T_c (°C)	554.66	555.8	557.15
c/*a*	1.081299(11)	1.081411(10)	1.082300(09)
ΔH (J/g)	2.5529	2.3662	2.1596

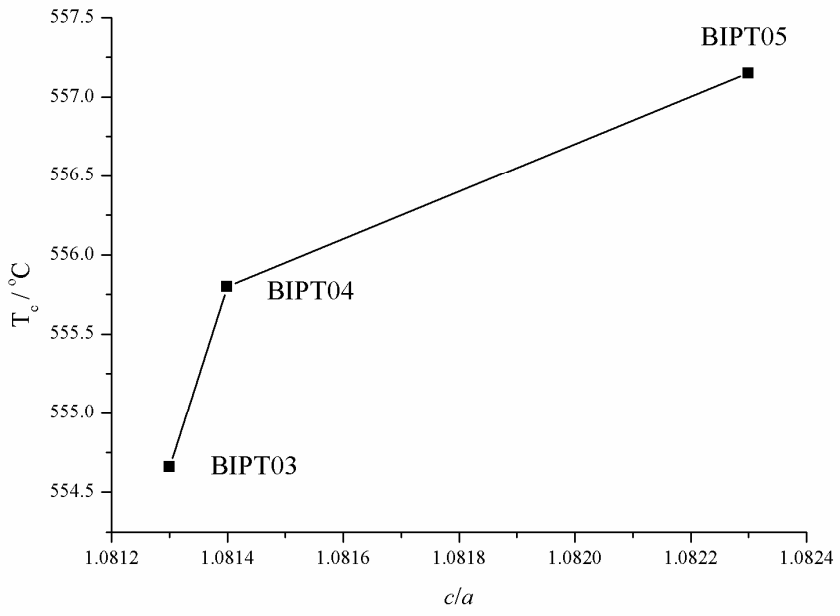

(a)

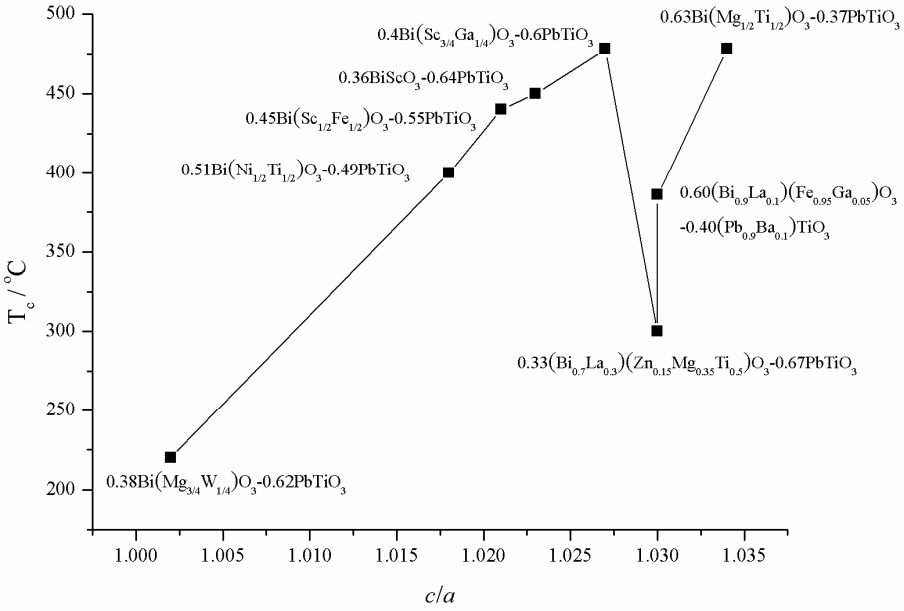

(b)

Fig. 4.12 Evolution of the Curie temperature with the *c*/*a* ratio (measured at room temperature) for (a) BIPT samples shown in Table 4.5 and (b) for other Bi*Me*O_3-$PbTiO_3$ samples shown in Table 1.2.

4.2.5 First order ferroelectric phase transitions of BIPT03 single crystals

The ferroelectric properties associated with a cubic phase to tetragonal phase transition in the absence of an electric field may be obtained, according to Section 2.6.2, by considering the one dimensional expression of the free energy,

$$G_1 = \frac{1}{2}\beta\left(T - T_0\right)P^2 + \frac{1}{4}\gamma P^4 + \frac{1}{6}\delta P^6 . \qquad (4\text{-}1)$$

Here P is the component of the polarization vector along one direction. The shape of the above free energy is schematically shown in Fig. 4.13 at different temperatures for first order phase transitions. The meanings of T_0, T_1 and T_2 have been defined in Section 2.6.2. The free energy, G_1, of the stable phase of the system in thermal equilibrium must be a minimum. When the temperature is higher than T_2, G_1 has only a minimum value at $P = 0$, so it means that only a paraelectric phase can exist without spontaneous polarization. When the temperature is lower than T_0, G_1 has the two minimum values, respectively located at $+P$ and $-P$, meaning that a ferroelectric phase exists with two equivalent opposite directions for the spontaneous polarization. When the temperature is located between T_0 and T_c, there is a third minimum value (at $P = 0$) higher than the other two minima, representing the coexistence of stable ferroelectric and meta-stable paraelectric phases. When the temperature reaches T_c, the three minimum values are equal. At this temperature, the free energy of ferroelectric phase is equal to that of paraelectric phase. When the temperature is between T_c and T_1, the minimum value (at $P = 0$) is lower than other minimum values, so the ferroelectric phase is meta-stable and the paraelectric phase stable. When the temperature is between T_1 and T_2, minimum values on both sides of $P = 0$ disappear but two inflection points remain in the curve. The disappearance of these minima indicates that even a meta-stable ferroelectric phase cannot exist. However, the presence of the inflection points suggests that it is still possible to induce the ferroelectric phase by applying an electric field of sufficient magnitude. Above T_2, since the inflection points vanish, even an electric field cannot induce the ferroelectric phase, only the paraelectric phase persists.[72]

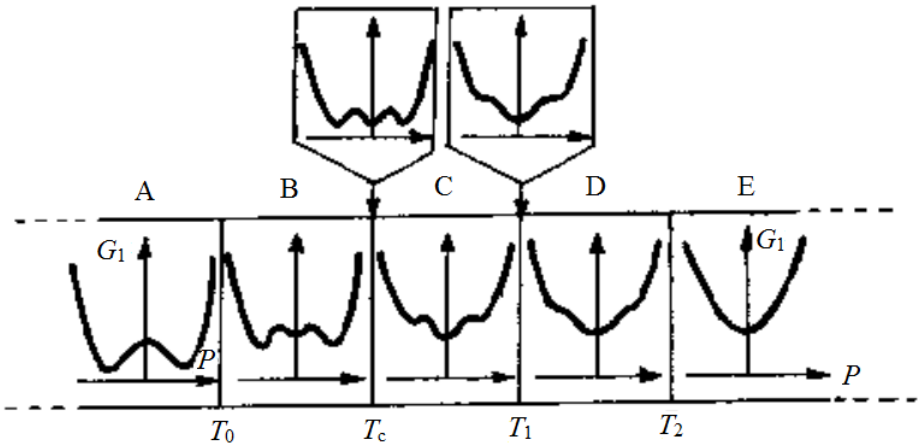

Fig. 4.13 Free energy displayed qualitatively as a function of the polarization near a first order ferroelectric transition at different temperatures.[73]

The discontinuous change of spontaneous polarization at the Curie temperature leads to temperature hysteresis and a transition entropy.[73] The endothermic peak at 555 ^{o}C sizable observed in the DSC is to be assigned to the Curie temperature of BIPT03. On the analysis of HT-XRD, transition to the cubic structure occurs at ~ 600 ^{o}C. It is obvious that the structural phase transition temperature (600 ^{o}C) of BIPT03 is not exactly occurring at the Curie temperature (555 ^{o}C), and that temperature hysteresis exists.

It is shown in Fig. 4.6, that the (101) and (110) peaks merge in the range 550 ^{o}C to 570 ^{o}C. We could consider that the BIPT03 has a stable ferroelectric and metastable paraelectric phase between 550 and 555 ^{o}C, while it is mestastable ferroelectric and stable paraferroelectric phase between 555 and 570 ^{o}C. The evolution of the ferroelectric-paraelectric phase was detected in the experimental results. The existence of “temperature hysteresis” does prove that in BIPT03 a first order ferroelectric phase transition occurs. We can thus conclude that BIPT single crystals exhibit a first order ferroelectric phase transition.

4.2.6 The morphology and microstructure of single BIPT03, BIPT04 and BIPT05 crystals

The single crystals of BIPT were divided into small pieces to analyze different samples and textures. The morphology of single BIPT crystals was inspected using scanning electron microscopy (Hitachi SU-70 model) as shown in Fig. 4.14. The platelet of BIPT03 shows a clear parallel striped pattern with ~ 2.5 μm spacing in the growth striation. Growth striation is a frequently encountered phenomenon in crystal growth from high temperature solution, which can be caused by temperature instability during the growth process, or a concentration variation at the interface between the growth face and the solution.[74] However, with increasing Bi/In doping, the growth striation was not clear enough and the spacing between stripes is smaller, as shown in Fig. 4.14 (b) and (c).

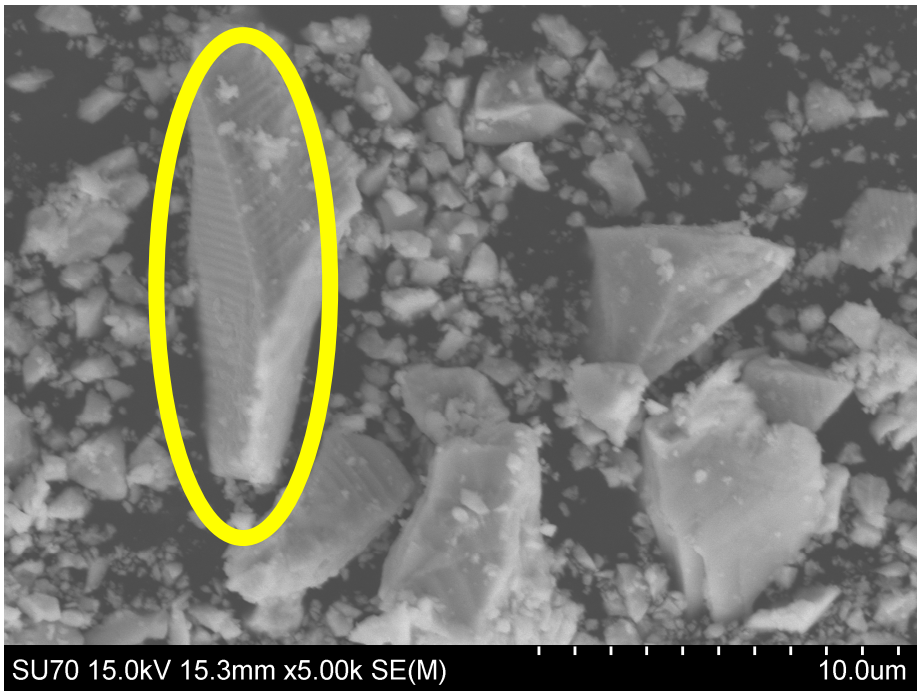

(a)

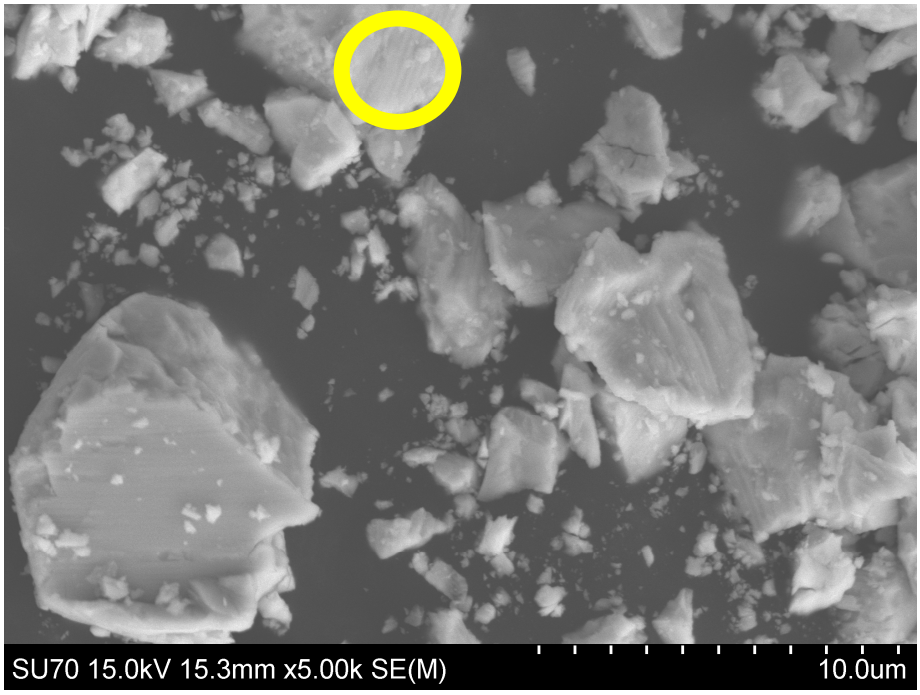

(b)

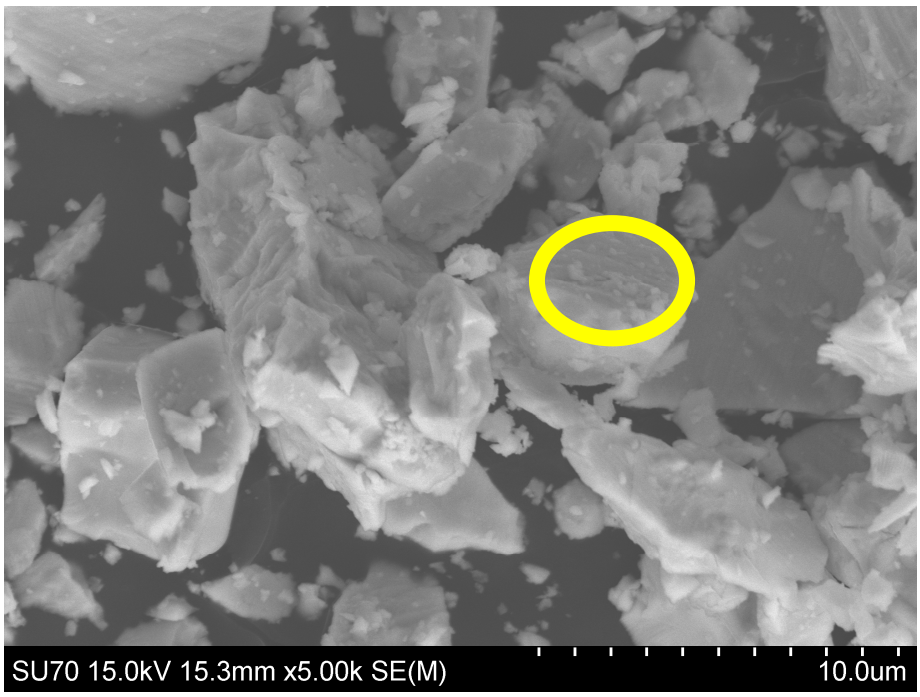

(c)

Fig. 4.14 SEM micrograph of BIPT03 (a), BIPT04 (b), and BIPT05 (c) single crystals.

The selected area electron diffraction (SAED) patterns of BIPT04 obtained by a TEM system (Hitachi H9000 NAR model, University of Aveiro) are shown in the Fig. 4.15, where clear diffraction spots of the crystalline BIPT04 are displayed, and the single-crystal nature of BIPT04 perovskite is evidently demonstrated. We observe strong diffraction spots combined with some weaker ones, showing a superlattice electron diffraction pattern due to compositional disorder. In^{3+} ions are fully or partially disordered in the B-sublattice of the perovskite BIPT structure, that is, In or Ti may be found in neighbouring unit cells at the same crystallographic positions and the disorder leads to distortion of the configuration of neighboring ions. Since compositional disorder is a common feature of ferroelectric relaxors, we can assume that there is relaxor behavior in BIPT single crystals.

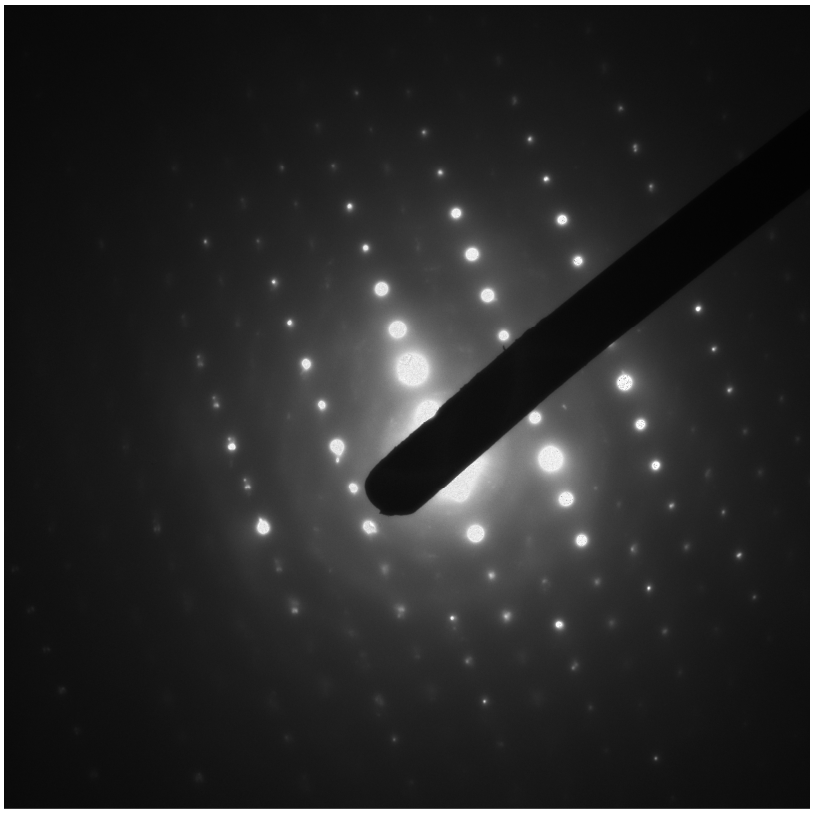

Fig. 4.15 SAED patterns taken from BIPT04 at room temperature.

The rocking curve of selected small crystals was measured in an X'Pert Philips X-ray diffractometer (LCA, University of Aveiro). The single crystals BIPT03 and BIPT04 were polished into thin plates, and a $\theta \sim 2\theta$ scan was performed, as shown in Fig. 4.16 (a) and (c). Fig. 4.16(b) shows the rocking curve of the BIPT03 crystal on the (100) face. The full-width at half-maximum (FWHM) of the diffraction peak is 0.25^{o}, but there are some small peaks in the right hand side, which indicates the crystal is coexisting with some powder, hence not of very good quality. Fig. 4.16 (d) shows the rocking curve of BIPT04 crystal on the (101) face. The peak is a double peak and the FWHM is 3.1^{o}, which indicates the crystal is twinned. We conclude that not all single-crystals are of prime quality, so we need to improve on the progress of growing single crystals of these materials.

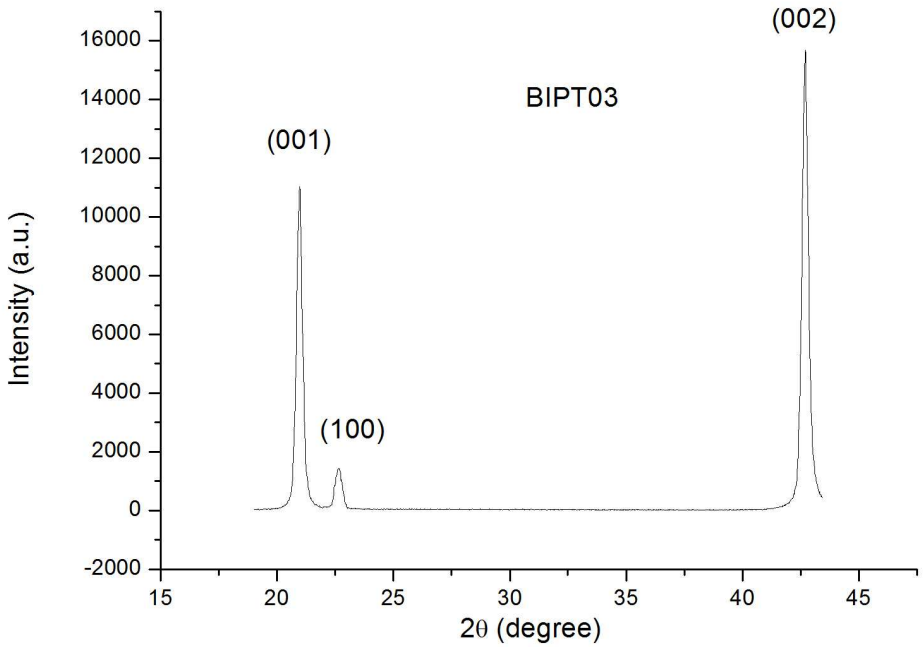

(a)

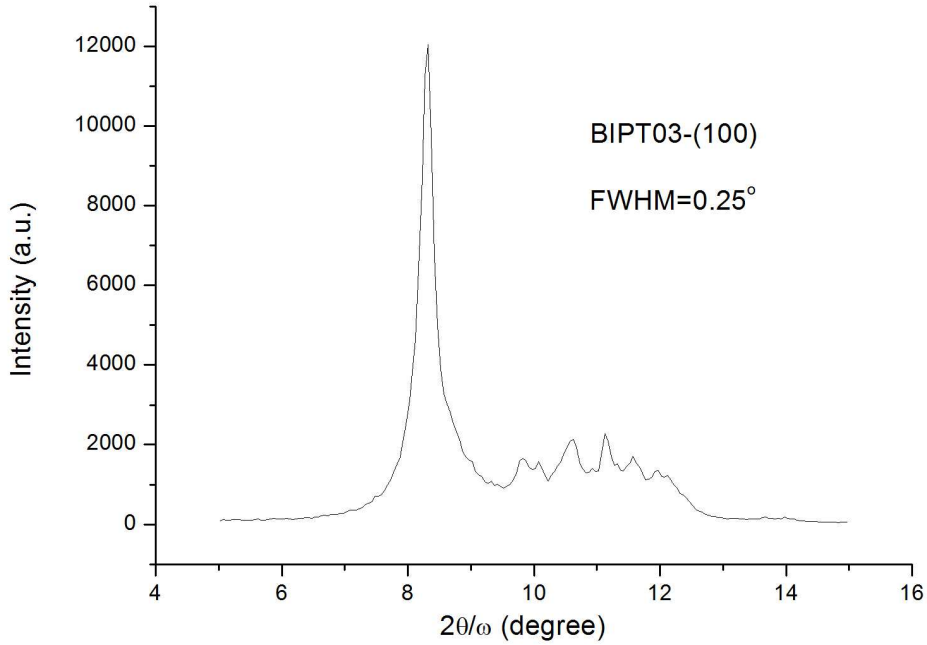
BIPT03-(100)
FWHM=0.25°
Intensity (a.u.)
2θ/ω (degree)
12000
10000
8000
6000
4000
2000
0
4
6
8
10
12
14
16

(b)

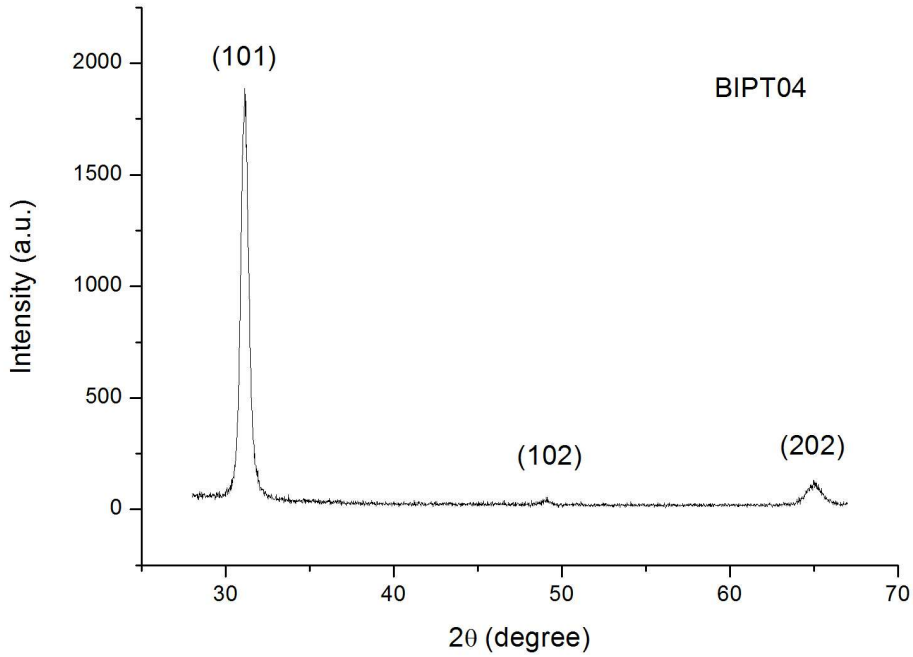
(101)
BIPT04
(102)
(202)
Intensity (a.u.)
2θ (degree)
2000
1500
1000
500
0
30
40
50
60
70

(c)

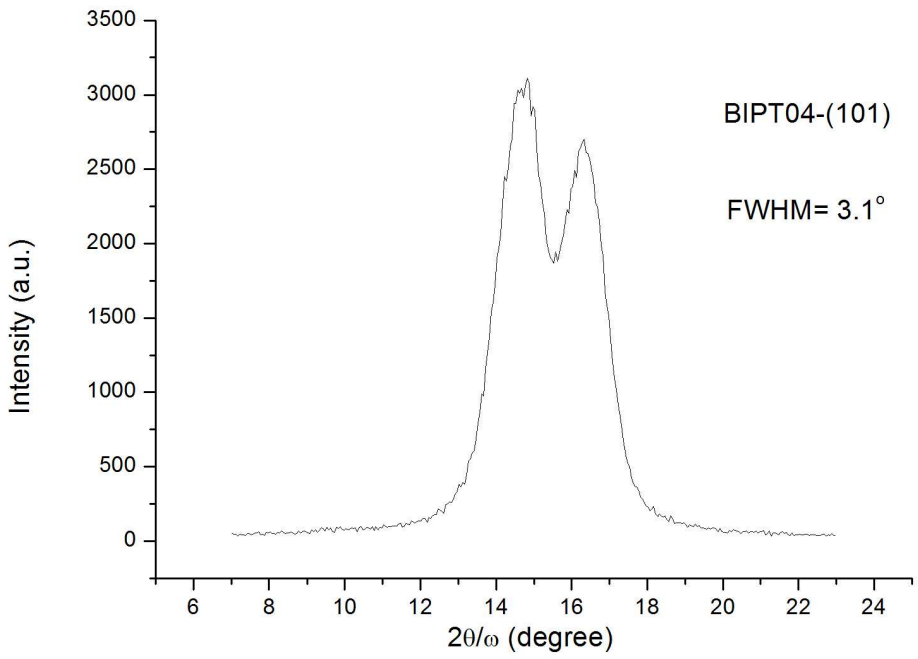

(d)

Fig. 4.16 The XRD of ground single crystal BIPT03/BIPT04 and the rocking curve of BIPT03 (100) / BIPT04 (101).

4.2.7 Piezoresponse force microscopy of the BIPT03 and BIPT04 single crystals

PFM measurements of single crystals BIPT03 and BIPT04 were performed with a commercial setup NTEGRA Prima (NT-MDT) to study local ferroelectric properties. The conductive silicon probe (NT-MDT NSG30/TiN) which has a tip curvature radius of 35 nm and a tip side coating of TiN with 20 ~ 30 nm, was used. For PFM domain imaging, we used contact-resonance ac probing signals of 3V amplitude and 100 kHz frequencies to excite surface oscillations. Images were attained by scanning small regions and at a slow rate of 1 Hz. Plate shaped crystals of BIPT04 parallel to the (010) face and BIPT03 parallel to the (110) face, confirmed by Laue photographs (Laue

diffraction pattern shown in Fig. 4.17), were cut in the as-grown crystals for PFM measurement.

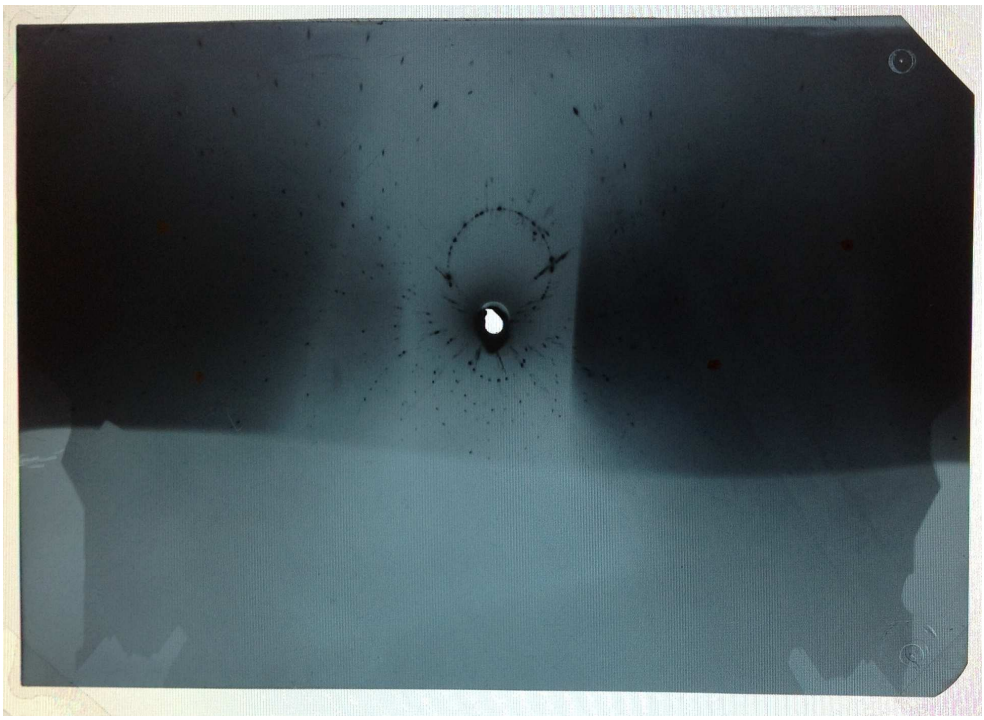

(a)

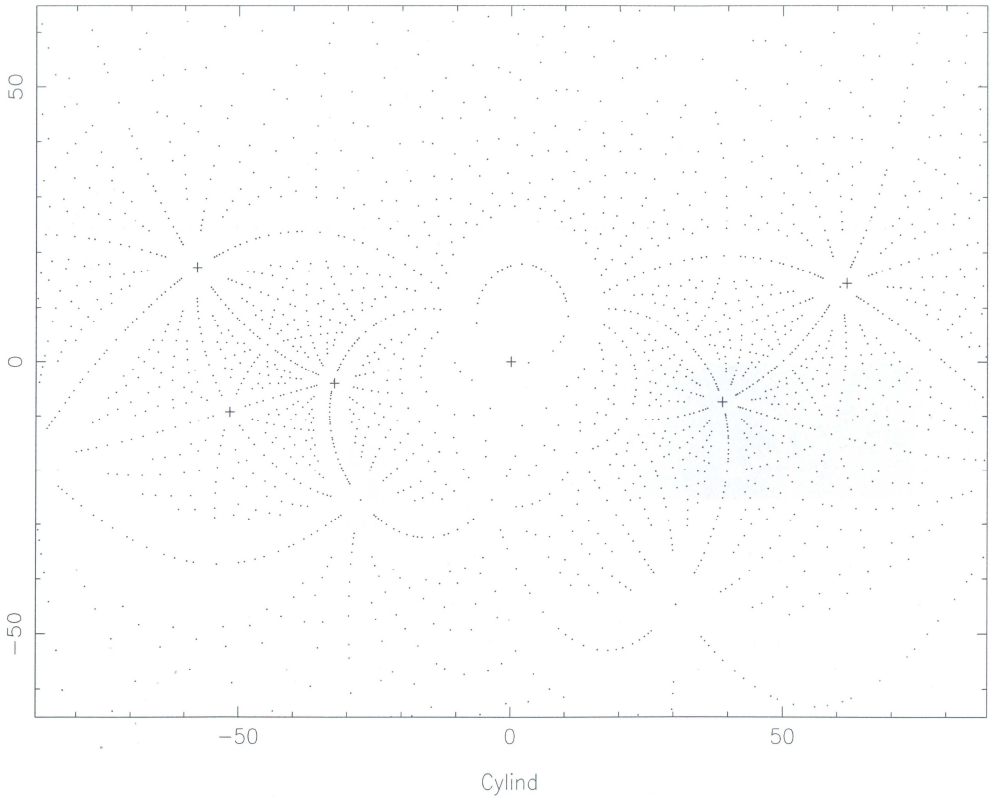

(b)

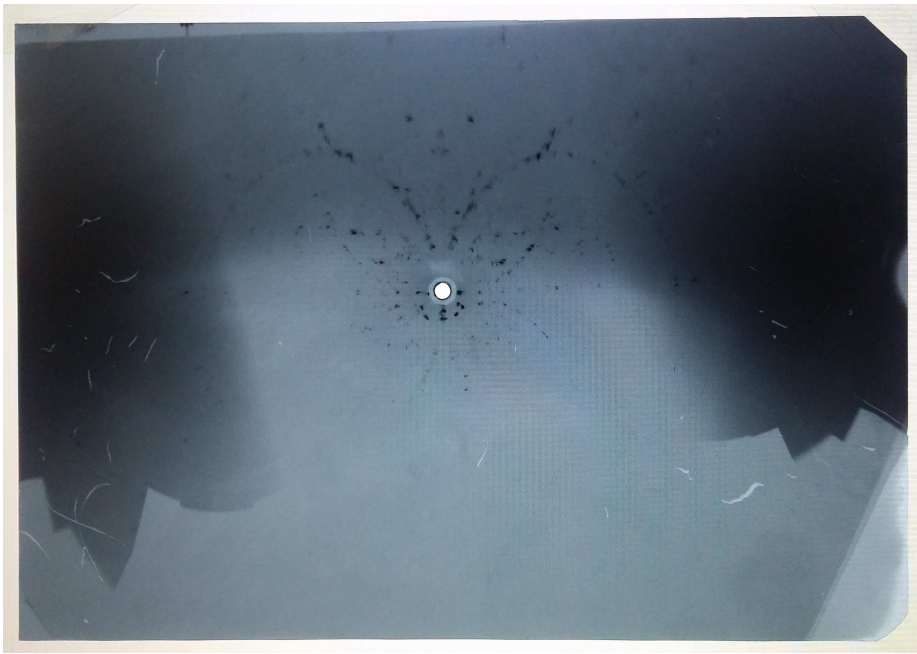

(c)

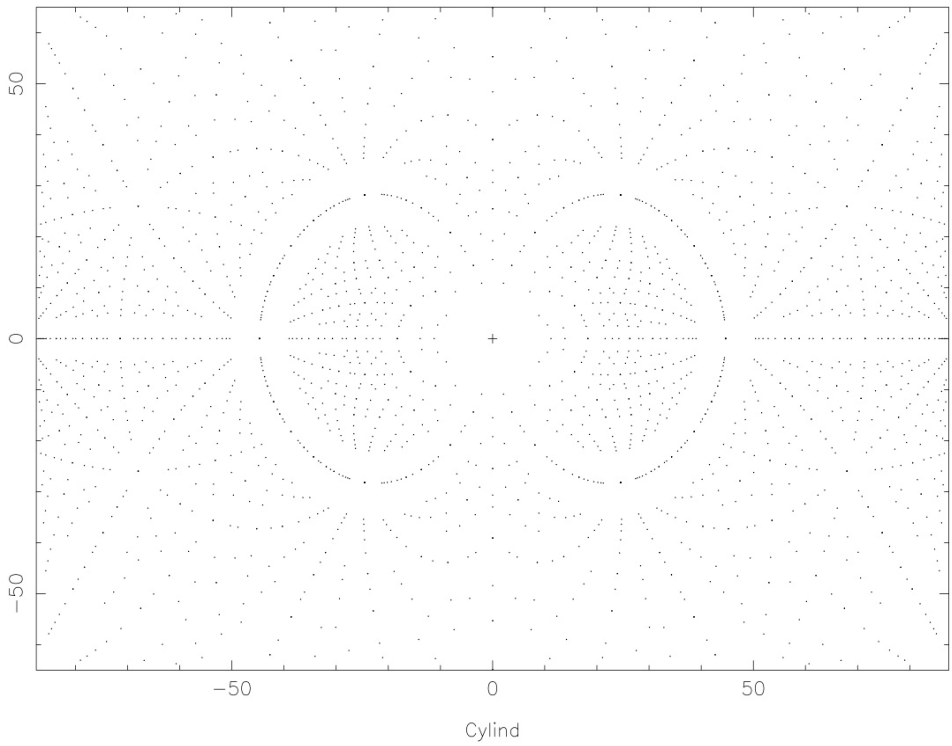

(d)

Fig. 4.17 (a) Original photograph of Laue diffraction pattern of (010) face BIPT04; (b) The calculated Laue diffraction pattern of (010) face BIPT04; (c) Original photograph of Laue diffraction pattern of (110) face BIPT03; (d) The calculated Laue diffraction pattern of (110) face BIPT03. The crosses mark a set of reflections corresponding to the major crystallographic zones used for the indexing procedure.

4.2.7.1 Domain structure of (010) face BIPT04 single crystals with a 0.5 mm thickness

Fig. 4.18 (a) and (b) show the surface morphology and PFM phase image, respectively, of the (010) face of a BIPT04 single crystal with 0.5 mm thickness. It can be seen that the surface domain distribution forms a labyrinth-like pattern, similar to that observed in many relaxor ferroelectric single crystals. The domain patterns on the (010) face, have a characteristic width of ~ 400 nm while their orientations appear quite random. The relationship between crystal orientation and six possible local spontaneous polarization vectors, ***P***, are illustrated in Fig. 4.18 (c), drawn relative to a tetragonal unit cell. As pointed out by Elisabeth Soergel[65] the phase output of LIA can only produce two signals of 0° and 180°, representing the polarization vector of the domain in corresponding half-space. As we know that domain structures are only vertical and lateral in the tetragonal ferroelectric materials, only the out of plane polatization components can be observed for (010) face measurements. Therefore, only two ***P*** vectors ($\boldsymbol{P}_y$ and $\boldsymbol{P}_{-y}$) contribute to the vertical (VPFM) phase signal for the (010) crystal.

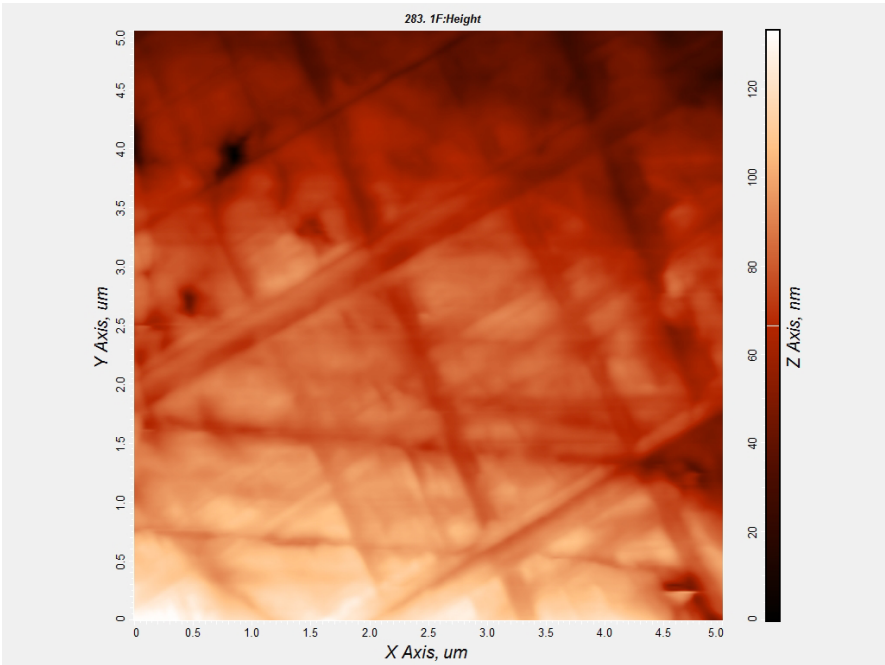

(a)

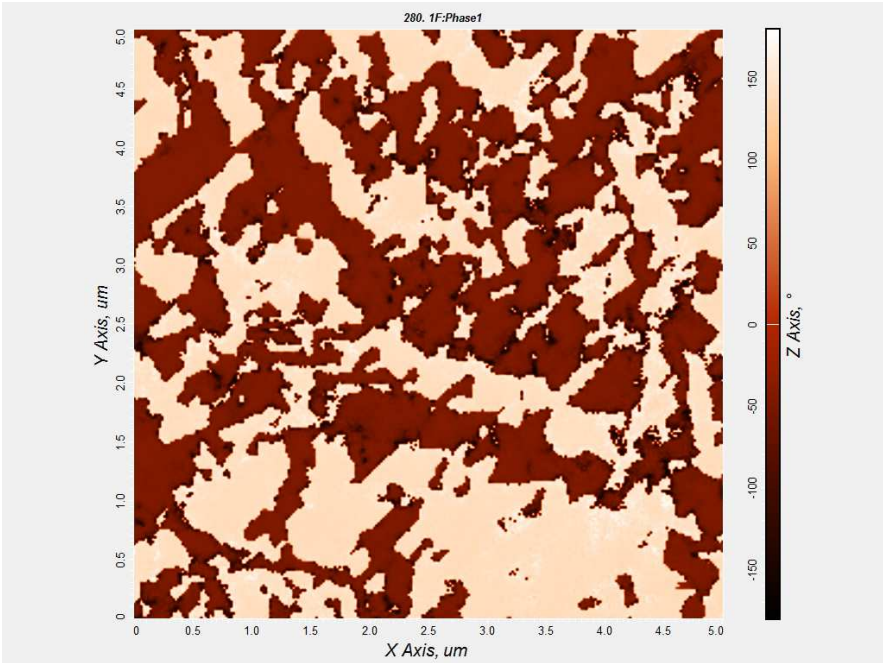

(b)

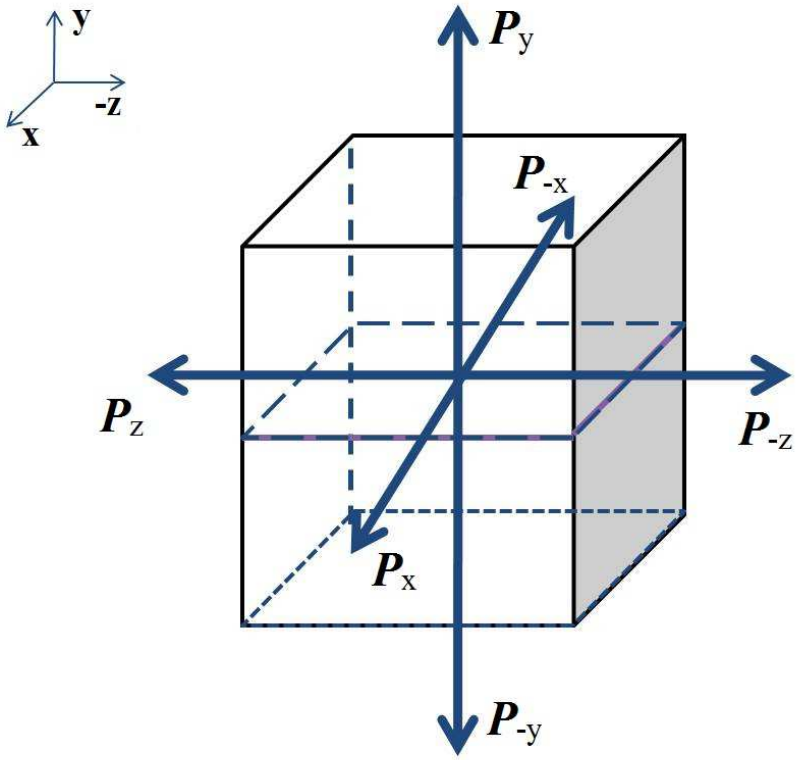

(c)

Fig. 4.18 (a) surface morphology and (b) PFM phase images of (010)-BIPT single crystals. The scan sizes of all the images are 5×5 μm^2, NSG30/TiN probes used. (c) The six polarization vectors of a tetragonal symmetry: $\boldsymbol{P}_x$, $\boldsymbol{P}_{-x}$, $\boldsymbol{P}_y$, $\boldsymbol{P}_{-y}$, $\boldsymbol{P}_z$, and $\boldsymbol{P}_{-z}$ and their orientation relative to the crystal faces.

To obtain more information about the domain structures, several images were taken at the same location using different applied bias. The phase images were acquired under the sequence of positive (+) d_c voltages: 0 V, 5 V, 10 V, 15 V and 20 V in the Figs. 4.19 (a) ~ (e). These images are clearly uniform within individual grains. The positive polarization (pointing out of the paper) appears dark in contrast, indicating a 180° domain ($\boldsymbol{P}_y$ polarization direction), and the regions with negative polarization appear in bright contrast, corresponding to a 0° domain ($\boldsymbol{P}_{-y}$ polarization direction). After DC poling, we can observe a clear change in the domain regions. A gradual evolution of the domain pattern is observed, the bright spots in the region gradually expanding with increasing d_c voltage. Another region was poled by the negative (-) d_c voltages: 0 V, -5 V, -10 V, -15 V, and -20 V as the Figs. 4.20 (h) ~ (l). A gradual evolution of the domain pattern is also observed, the dark region extends into surrounding area, and other regions evolve. With increasing or decreasing d_c voltage, the evolution of domain regions is regular and orderly. Further, domain direction tends to be consistent with the voltage direction. We can see that bias voltage can effectively control the domain orientation.

Comparing the same region after poling by 25 V and -25 V (see Fig. 4.19 (f) and (g) or Figs. 4.19 (m) and (n)), it is obvious that the dark region coverage after poling with negative voltage (-25 V) is much bigger than the bright region coverage after poling by a positive voltage (25 V). It means that polarization loops are off-centered position biased to positive voltage (+) orientation.

In the case of the above phase images, the phase signal is uniform inside the individual domain, while magnitude gradually varies from the domain center to its boundary. Both positive and negative domains appear in bright contrast in amplitude images, whereas dark and bright features appear in phase image, as shown in Figs. 4.19 (a')~(g') and (h')~(n'). Comparing with the corresponding phase images, dark lines in the amplitude images are considered as the domain boundaries that outline a domain configuration. The PFM contrast is similar across domain boundaries and two clear antiparallel domains separated by domain boundaries with a thickness of about ~45 nm are shown. It has been reported that the measured thickness of domain boundary mainly depends on the tip radius.[75] The intensity in the amplitude image reflects the magnitude of the response, and the color evolution from dark to bright represents the response from zero to a strong piezoelectric signal. From the picture, we can see that with the positive (+) d_c voltage increasing, the brightness and bright

contrast regions are lower and fewer; under the negative (-) d_c voltage, the regions exhibit a reversed contrast. It means that with increasing negative (-) d_c voltage, the piezoresponse increases, and, with increasing positive (+) d_c voltage, the piezoresponse decreases.

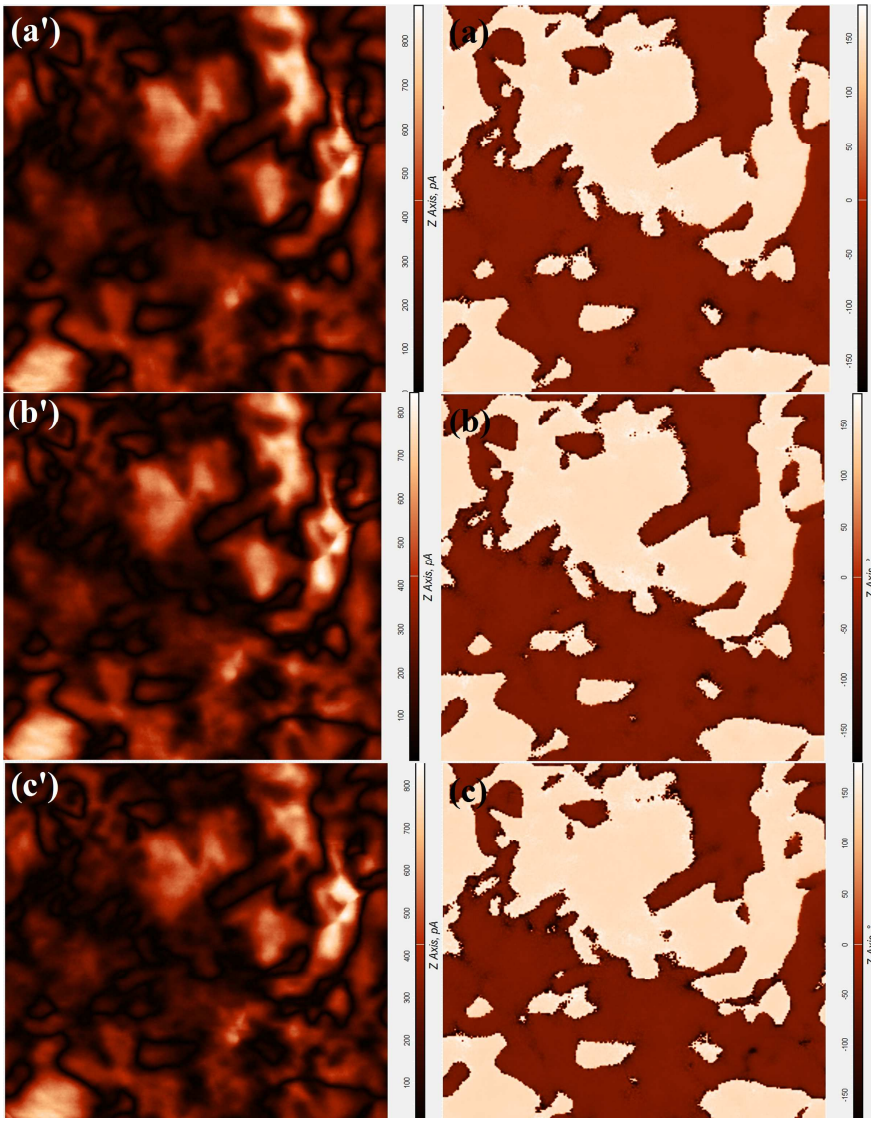

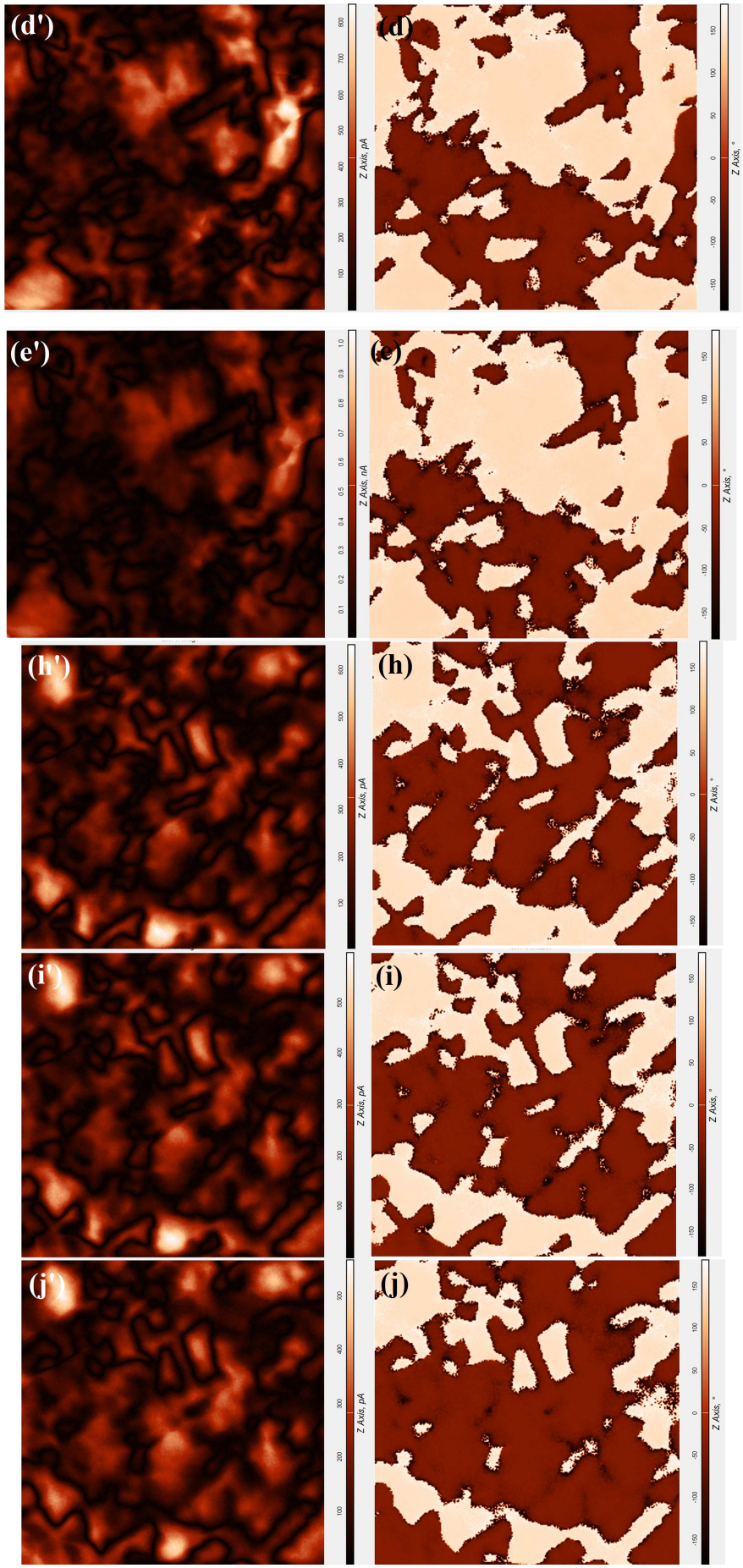
(d')
(d)
(e')
(e)
(h')
(h)
(i')
(i)
(j')
(j)
Z Axis, pA
Z Axis, nA
Z Axis, °

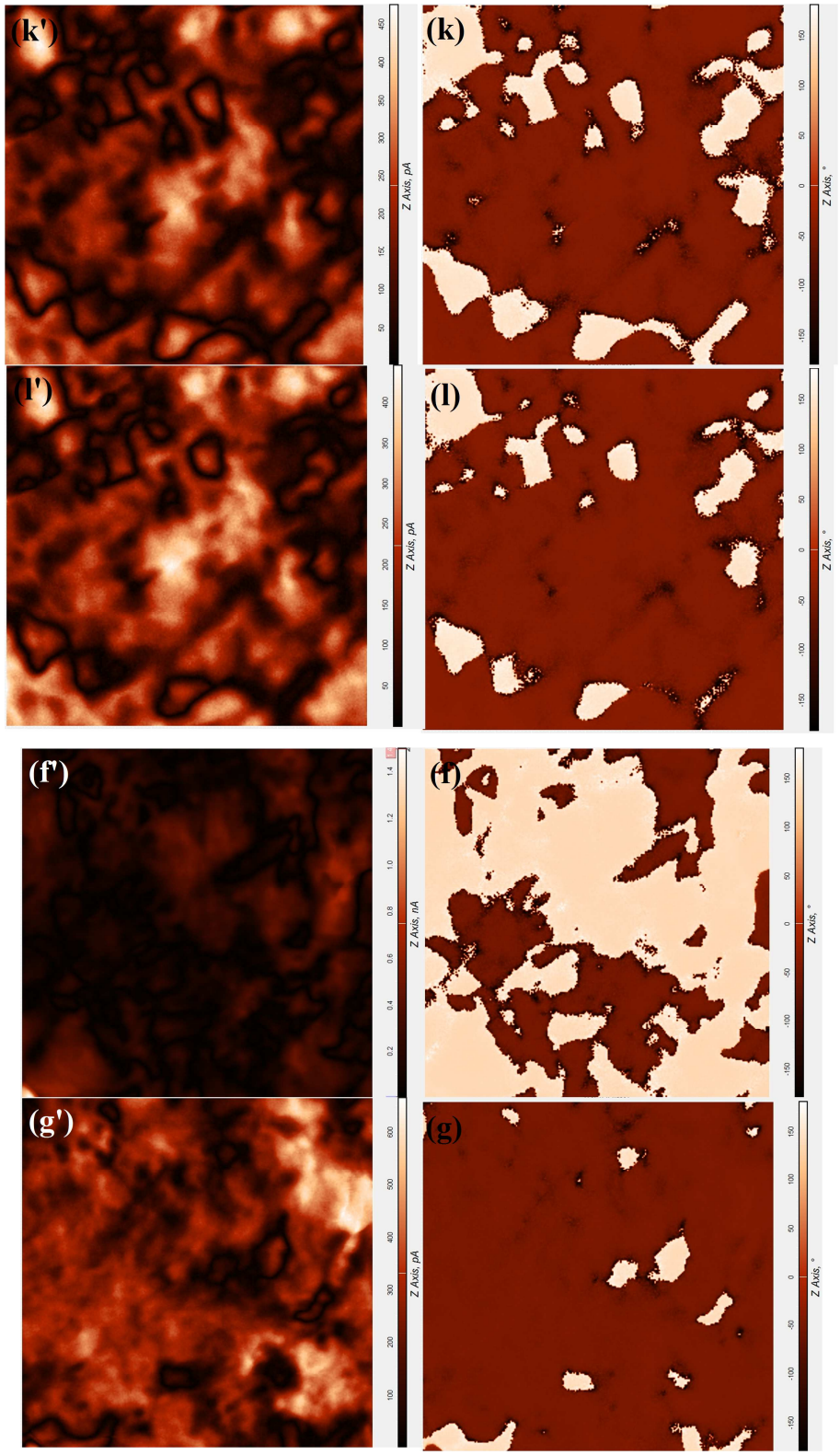
(k')
(k)
(l')
(l)
(f')
(f)
(g')
(g)
Z Axis, pA
Z Axis, °
Z Axis, nA

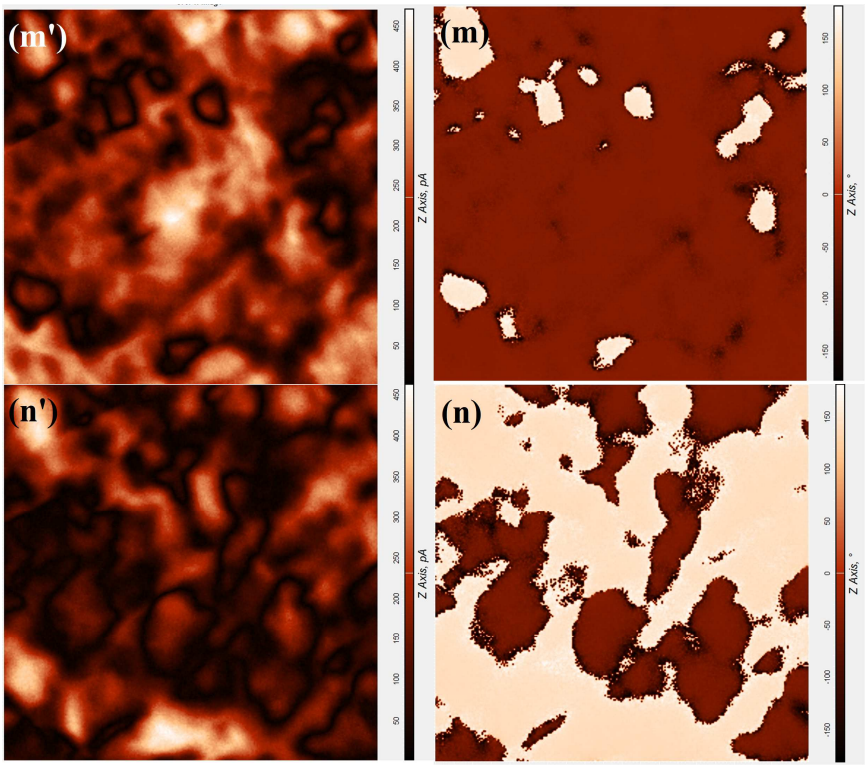

Fig. 4.19 Piezoresponse images of a (010)-oriented BIPT single crystal. (a)~(g) are, respectively, phase images under the bias voltage 0 V, 5 V, 10 V, 15 V, 20 V, 25 V and -25 V at the same location, while the (a') ~ (g') are the corresponding amplitude images. (h) ~ (n) are, respectively, phase images under the bias voltages 0 V, -5 V, -10 V, -15 V, -20 V, -25 V, and 25 V at the same location, while the (h') ~ (n') are the corresponding amplitude images.

4.2.7.2 PFM of (110) face of BIPT03 single crystals with a 0.45 mm thickness

BIPT03 single crystal was polished to 0.45 mm and the domain image on the (110) face, was measured by PFM in the scan size of 10×10 μm^2. The domain images were acquired at a random area. Fig. 4.20 (a) shows the surface morphology and PFM image, respectively. The labyrinth-like domain patterns are of ~1.4 μm in characteristic widths while their orientations appear quite random.

Fig. 4.21 shows the relationship between (110) face and the six possible local spontaneous polarizations in tetragonal perovskites. It can be seen that $\boldsymbol{P}_{\pm z}$ in the

plane of the (110) face and $\boldsymbol{P}_{\pm x}$, and $\boldsymbol{P}_{\pm y}$ oriented at an angle of ±45° with respect to the (110) face.

To obtain more information about the domain structure, a series of PFM images were taken at the same location. The phase images acquired under the sequence of positive d_c voltages: 0 V, 5 V, 10 V, 15 V can be seen in Figs. 4.20 (c), (e), (g) and (i) and corresponding the amplitude images in Figs. 4.20 (b), (d), (f) and (h). The phase images are clearly uniform within an individual domain. After DC poling, those domains that have their polarization vector at ＋45° angle with respect to the (110) face rotate towards the applied field, but the rotation cannot be sensed by the phase image; those at -45° rotate towards the field and can be clearly seen as a contrast change in the image. However, there is no obvious change in position of domain boundaries in the amplitude images, suggesting no domain growing under DC poling.

Comparing the same region after poling by positive and negative voltage, the phase images acquired under 20 V and -20 V are shown in the Figs. 4.20 (k) and (m) and the corresponding the amplitude images in Figs. 4.20 (j) and (l). It is clear that the dark region and bright region were reversed under the opposite voltage, and this further proves a polarization orientation at an angle 45° and -45° with respect to the (110) face, but it is not possible to distinguish $\boldsymbol{P}_{\pm x}$, and $\boldsymbol{P}_{\pm y}$.

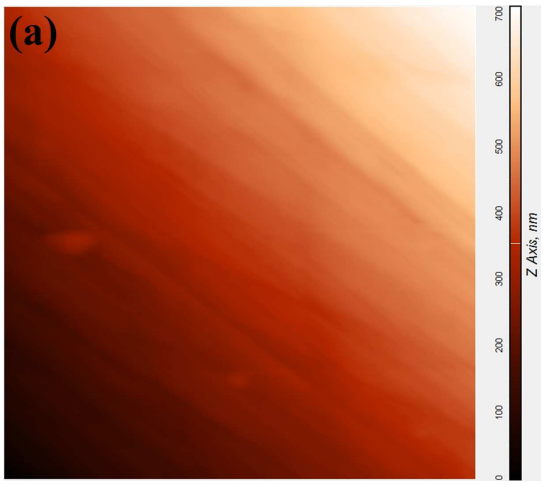

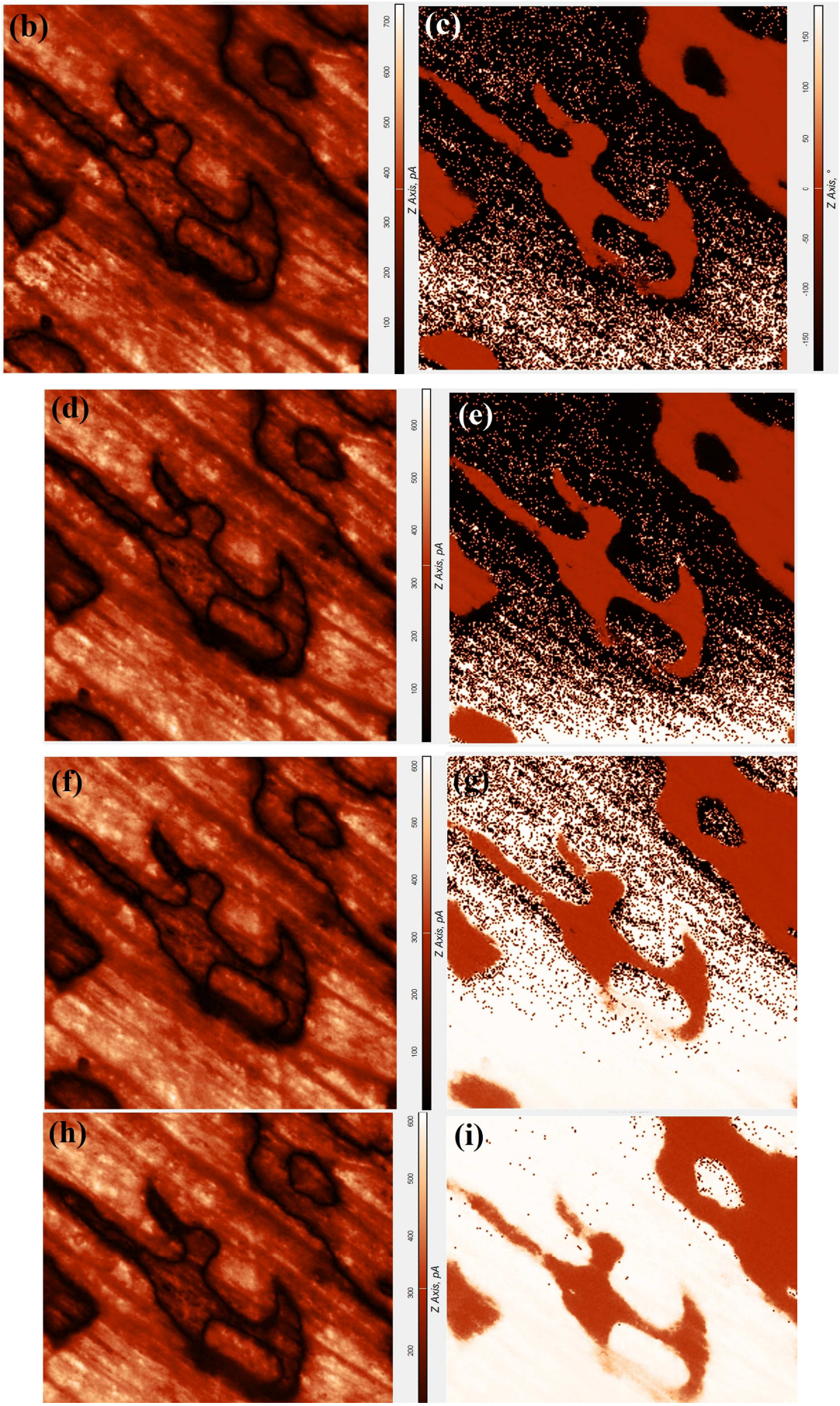
(b)
(c)
(d)
(e)
(f)
(g)
(h)
(i)
Z Axis, pA
Z Axis, °

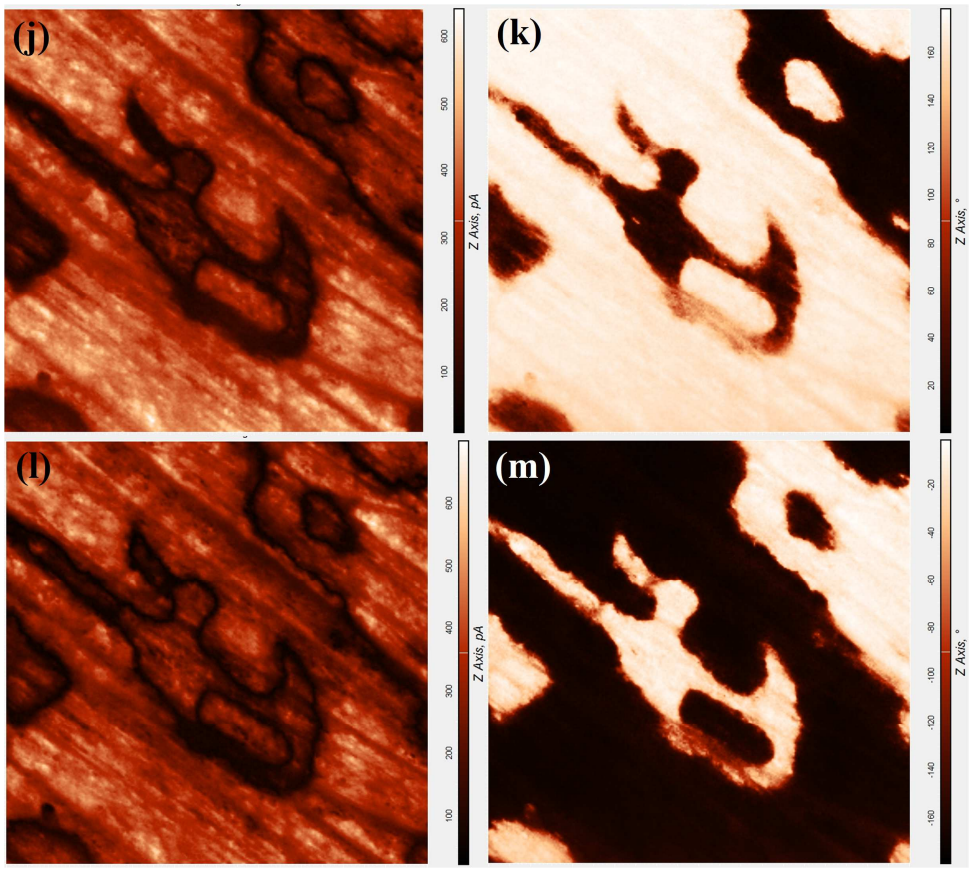

Fig. 4.20 (a) Surface morphology and pizoresponse image of BIPT03 single crystal. (c), (e), (g), (i), (k) and (m) are respectively phase image under the bias voltage 0 V, 5 V, 10 V, 15 V, 20 V and -20 V at the same location, while (b), (d), (f), (h), (j) and (l) are corresponding amplitude images. The scan sizes of all images are 10×10 μm^2. NSG30/TiN probes were used.

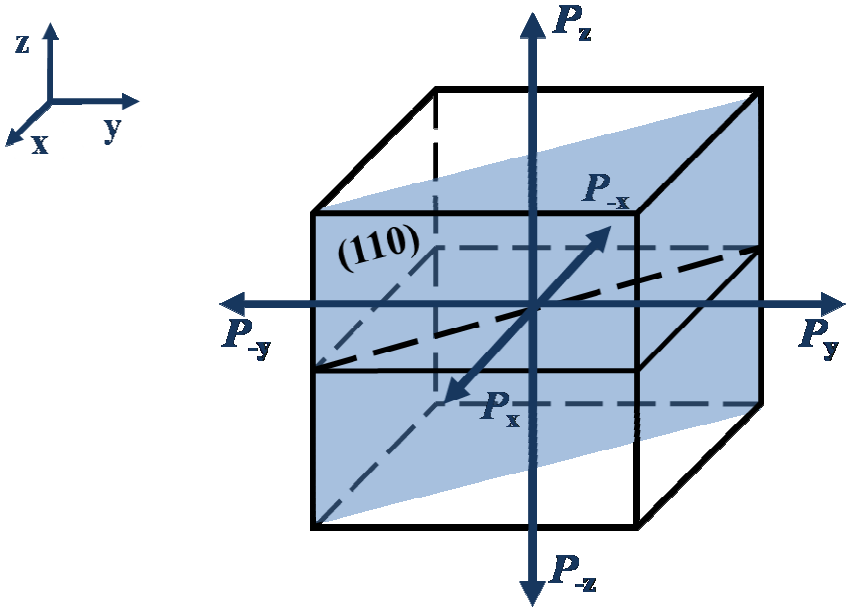

Fig. 4.21 Schematic of (110) crystal face and the six polarization vectors of a tetragonal symmetry.

4.2.7.3 Piezoresponse hysteresis loops of (010) face BIPT04 single crystals with a 0.5 mm thickness

A higher coercive field is useful for a large memory window in ferroelectric storage devices but a high voltage is necessary for switching. Hence, a balance between these factors is required for performance optimization of a ferroelectric memory device.[76] To gain a deeper insight into the local polarization switching in BIPT04 single crystal, we measured the piezoresponse voltage hysteresis loops. For the (010)-BIPT single crystals, local piezoreponse hysteresis loops were acquired at two random different positions without poling the sample, as shown in Fig. 4.22 (a). The loops are very similar for both locations, demonstrating an offset relative to the electric-field axis. The hysteresis loops show week position dependence with majority of coercive voltages being ~ 11 V. It is consistent with the above analysis. Next, we measured the local piezoresponse loops after poling ± 25 V in the different colored area shown in Fig. 4.22 (b) and the amplitude and phase loop of their corresponding area were shown Fig. 4.23 with the local coercive voltage from white area being 19.15 V, from yellow area being 26 V, from red area being 23.05 V and from black area being 25.7 V.

Fig. 4.22 (b) shows that the loops are off-centred biased to negative voltage (-) orientation, and as result the loops can fall out of the bias voltage range (± 50 V). High voltages are necessary to obtain saturated loops. The loops are found to vary more or less in appearance depending on the local switching characteristics. Comparing the loops before and after poling shown in Fig. 4.22 (a) and 4.22 (b), the coercive voltage is higher after poling and the shape and magnitudes in the two cases are quite different, which is possibly important for the polar direction recovery in material's applications.

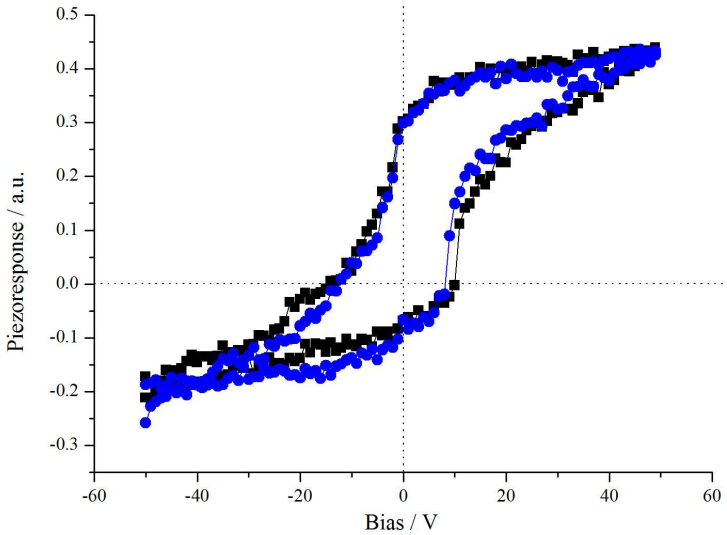

(a)

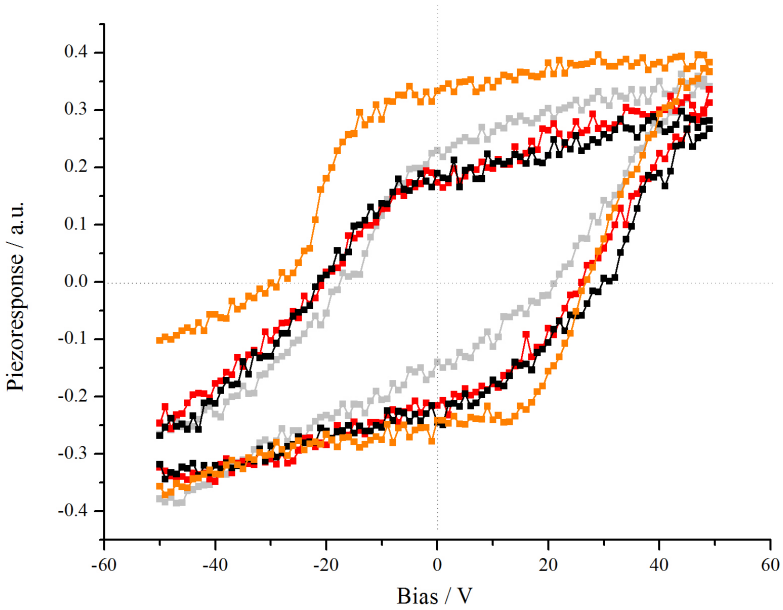

(b)

Fig. 4.22 Typical piezoresponse hysteresis loops measured on the (010) BIPT04 single crystals: (a) before poling at two different positions and (b) after poling ±25 V at four different locations. (shown in different colours)

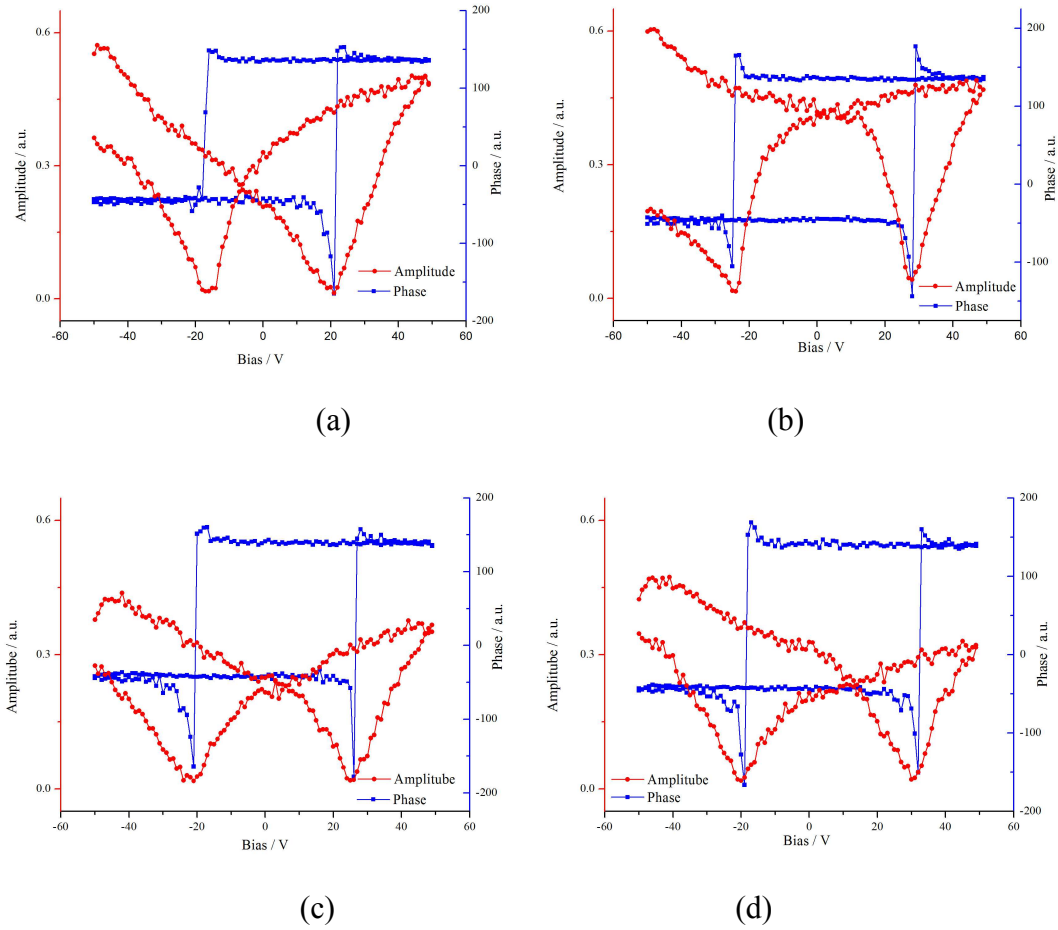

Fig. 4.23 Local piezoresponse hysteresis loops after poling ±25 V on the (010) BIPT04 single crystals. (a) On the white area with the local coercive voltage 19.15 V; (b) on the yellow area with the local coercive voltage 26 V; (c) on the red area with the local coercive voltage 23.05 V; and (d) on the black area with the local coercive voltage 25.7 V.

4.2.7.4 The influence of the thickness of (010) face BIPT04 single crystals on the domain structures

Single crystals of BIPT04 with (010) face were polished to 0.5 mm and 0.3 mm widths and the domain structure was measured by PFM in the scan size 2×2 μm^2 and 10×10 μm^2, shown in Fig. 4.24. The domains pattern on the face (010) of 0.5 mm and

0.3 mm thickness crystal are respectively of ~ 400 nm and ~5.3 μm in the characteristic widths while their orientations appear quite random. The domain growth behavior is related to the thickness of single crystals. Fig. 4.22 (a) and Fig. 4.25 show the piezoresponse loops obtained for 0.5 mm and 0.3 mm thickness crystals, respectively, from which we could acquire the local piezoresponse hysteresis loops at two random different positions without bias voltage. The hysteresis loops show week position dependence, the majority of coercive voltages being ~ 11 V for 0.5 mm thickness single crystals and ~ 7 V for 0.3 mm thickness single crystals. The coercive voltage is related to the thickness of single crystals. The thinner the (010) face of BIPT single crystal, the more it tends to single domain and smaller coercive voltages.

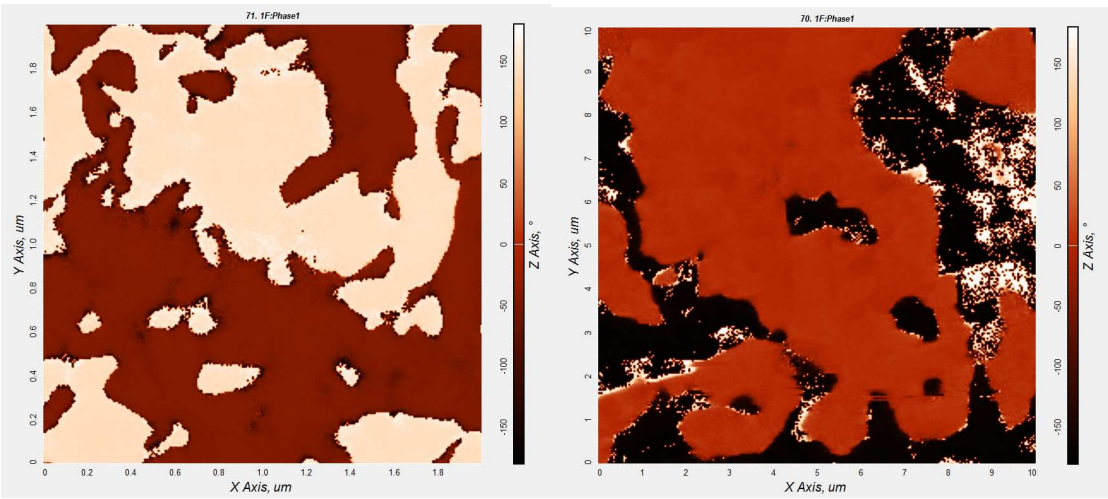

(a) (b)

Fig. 4.24 Piezoresponse images of a (010)-oriented BIPT single crystal. (a) 0.5 mm thickness with 2×2 μm^2 scan size; (b) 0.3 mm thickness with 10×10 μm^2 scan size.

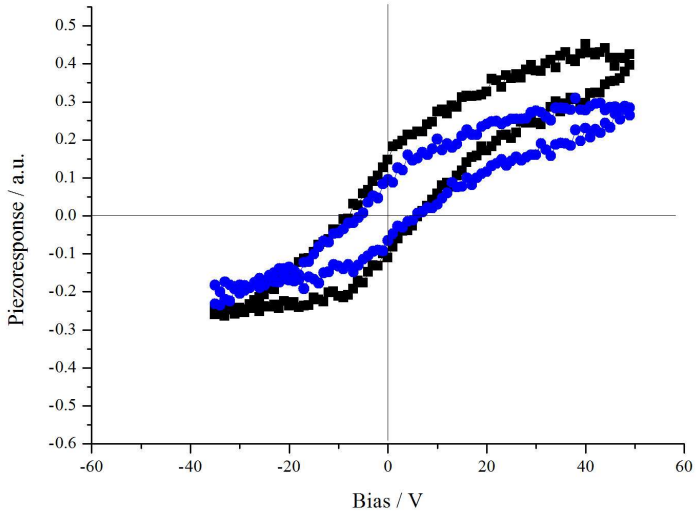

Fig. 4.25 Typical piezoresponse hysteresis loops measured on the (010) BIPT04 with 0.3 mm thickness single crystals at two different positions.

4.2.8 Macro-scale dielectric and ferroelectric measurements

Fig. 4.26 describes the temperature dependent dielectric constant (permittivity) of BIPT03 and BIPT04 single crystals in the temperature range from room temperature to 750 ^{o}C at 100 Hz. It can be seen that the dielectric constant strongly reaches a maximum value and then reduces with increasing temperature. The dielectric peak is associated to the transition from the ferroelectric to the paraelectric state. The Curie temperature of BIPT03 and BIPT04 single crystals is around 550 ^{o}C, where the dielectric constant exhibits a maximum. The measured Curie temperature is consistent with the values of DSC measurement in chapter 4.2.4.

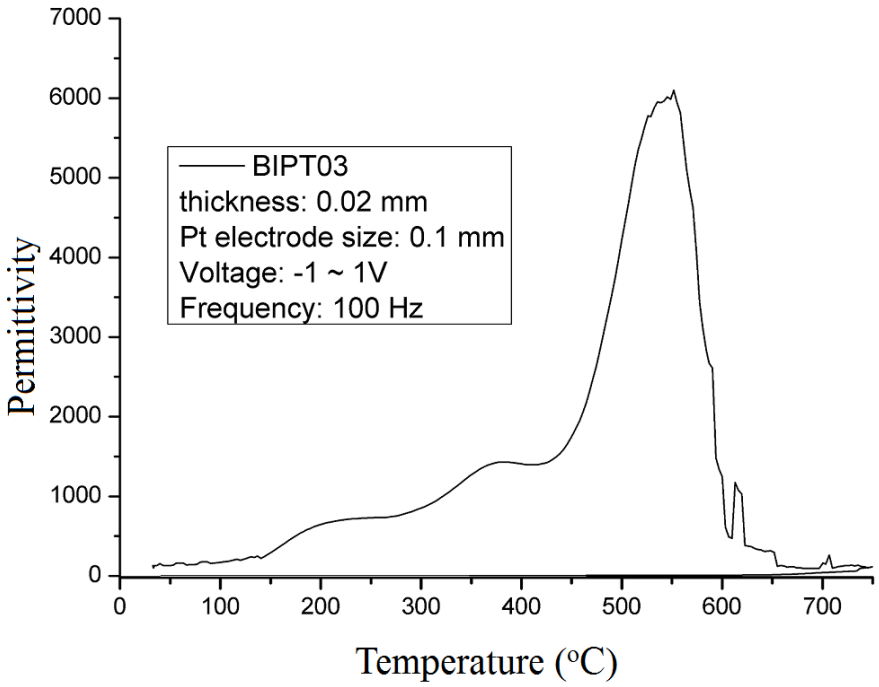

(a)

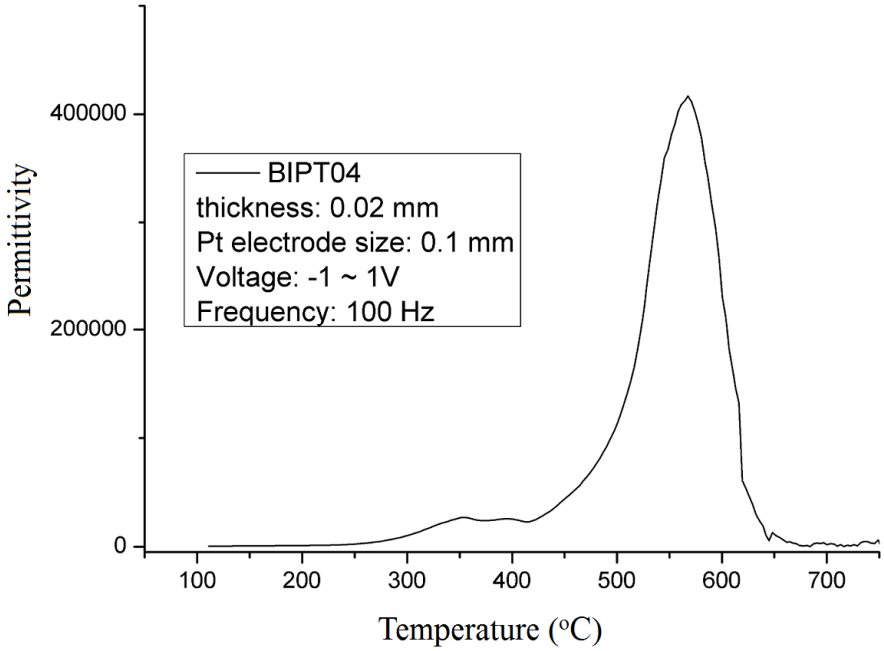

(b)

Fig. 4.26 Temperature dependence of dielectric permittivity for (a) BIPT03 and (b) BIPT04 single crystals from room temperature to 750 °C measured on a HP4284 Precision LCR Meter (University of Cambridge).

The hysteresis loops for BIPT03 and BIPT04 single crystals were measured at room temperature and are shown in Fig. 4.27. The hysteresis loop of BIPT03 is slightly more open along the polarization axis, and exhibits to some extent a higher maximum polarization value in comparison to that of BIPT04. The remnant polarization P_r is about 10 μC/cm^2 and the coercive field E_c is 52.1 KV/cm for BIPT03, whereas the values for BIPT04 are a little higher, about 9 μC/cm^2 and 44.8 KV/cm.

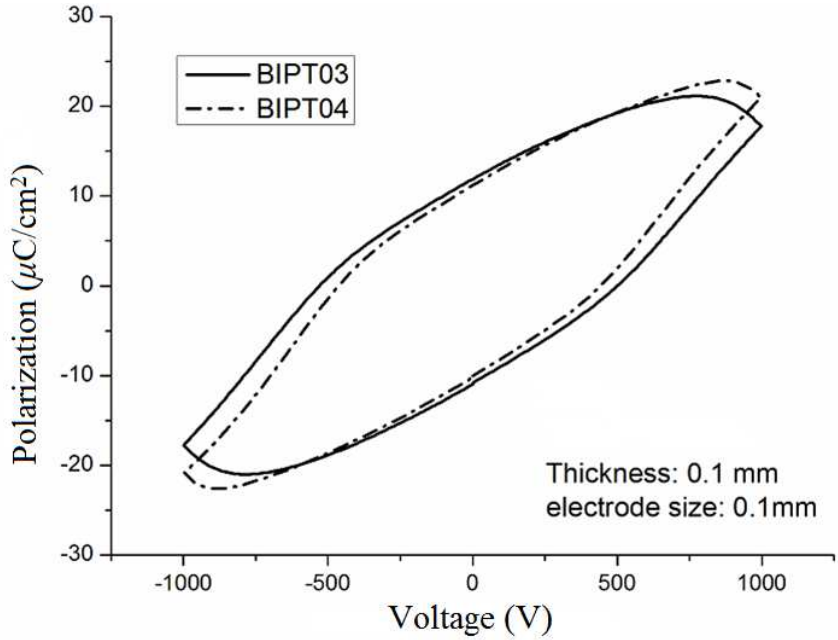

Fig. 4.27 Polarization versus electric field of BIPT03 and BIPT04 single crystals measured at 1 kHz and at room temperature.

The measured capacitance-voltage curve and the dielectric loss at 500 ^{o}C are shown in Fig. 4.28, showing a butterfly-loop shape at 1 kHz. The measured capacitance-voltage configuration in Fig. 4.28 (a) demonstrates the ferroelectric properties. The butterfly loop is an indication of ferroelectricity and, obviously, at 500 ^{o}C the material as a whole is in the ferroelectric state. Fig. 4.28 (b) shows an unusual dielectric loss at a temperature of 500 ^{o}C, which may result from the measurement conditions; for instance, the diffusion between the electrode and sample at the

relatively high temperature of 500 ^{o}C may affect the dielectric performance.

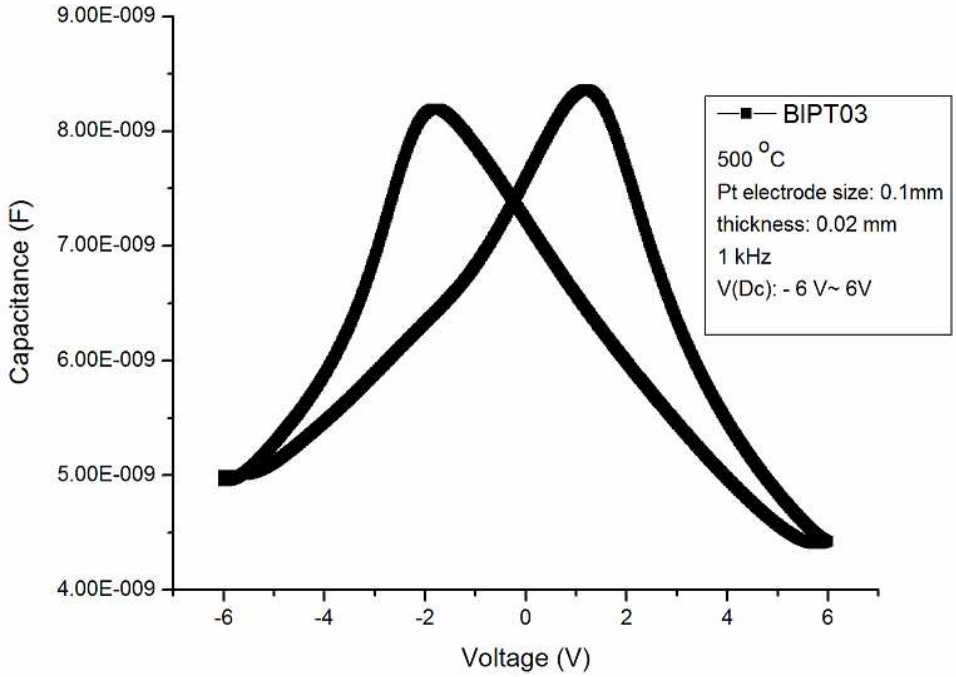

(a)

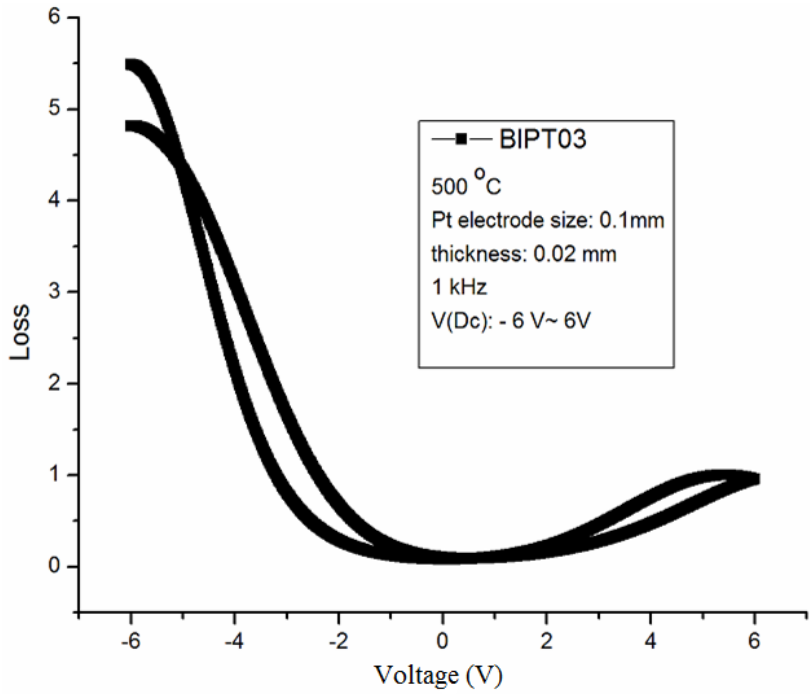

(b)

Fig. 4.28 (a) The measured loss – voltage curves of BIPT03 at 500 ^{o}C. (b) The dielectric loss at 500 ^{o}C. Tested on a HP4284 Precision LCR Meter (University of Cambridge).

Fig. 4.29 shows fatigue characteristics of BIPT03 and BIPT04 single crystals measured at 100 Hz for 2×10^9 switching cycles (15 hours) at room temperature and tested by a system of TFA2000. A similar behavior for BIPT03 and BIPT04 is observed down to approximately 10^7 cycles, with only a slight decrease in polarization (remaining above 98% of its initial value). From 10^8 cycles, the remnant polarization of BIPT03 is slightly above that of the initial one. A similar behaviour was observed for BIPT04, however, the difference is smaller than for BIPT03. It can be seen that there is almost fatigue-free behavior of BIPT03 and BIPT04 single crystals up to 10^9 switching cycles.

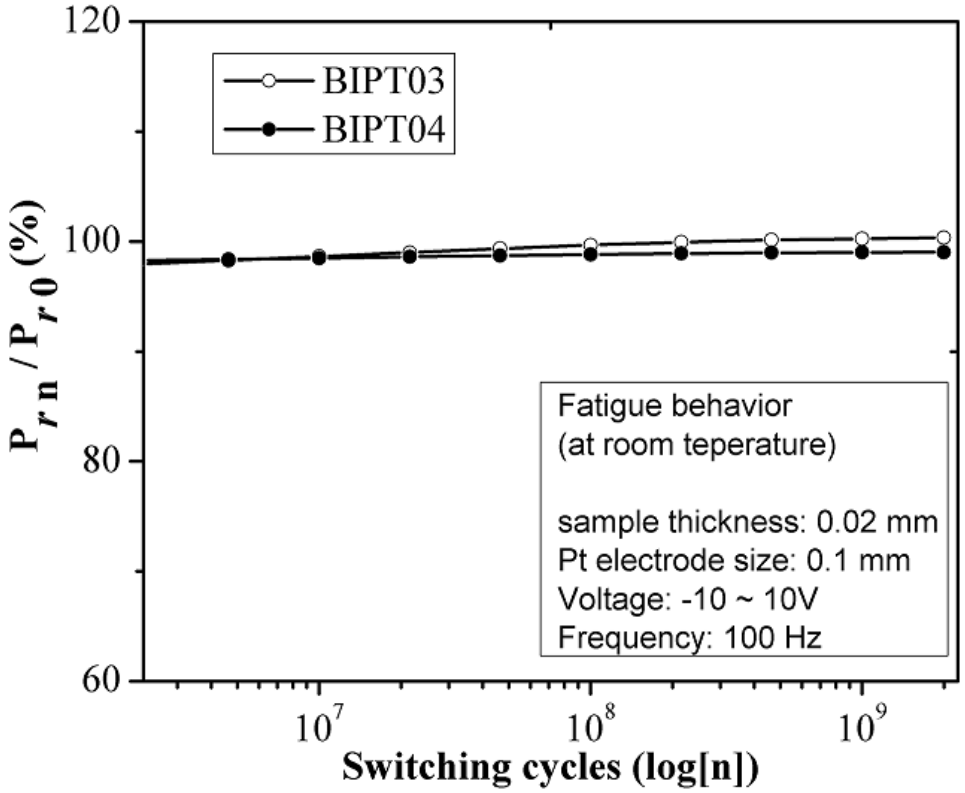

Fig. 4.29 Fatigue characteristics of BIPT03 and BIPT04 single crystals measured at 100 Hz for 2×10^9 switching cycles, for a total of 15 hours, at room temperature, on a TFA2000 system (University of Cambridge). P_{rn} and P_{r0} are the remanent polarizations in cycle *n* and in the first cycle, respectively.

4.2.9 Piezoelectric coefficient of BIPT04 single crystals

The KCF PM-3001 d_{33} Meter, shown in Fig. 4.30, was used to measure the piezoelectric constant d_{33} values of BIPT04 single crystals. Fig. 4.31 depicts a schematic diagram of this equipment. For this measurement, it is necessary to adjust the site of the top probe by turning the adjustment knob and clamp the plate of BIPT04 single crystals with suitable intensity between the top probe and bottom probe. The probes are used to supply the sample vibration power and transmit the sample signals to the meter. In detail, a three-pin is used to supply power in the connection with the meter, while a seven-pin plug is used for the signal output to the meter. [77] The measured piezoelectric coefficient d_{33} is one of most commonly parameters used for characterizing the properties of piezoelectric materials. A higher piezoelectric constant means a better piezoelectric performance.

The piezoelectric constant d_{33} of plate of BIPT04 single crystals was measured for the first time as 10 pC/N. Comparing this value with d_{33} of other materials in Table 1.2, it shows that it follows a general trend shown in Fig. 2.7, that is, high Curie temperatures come at the expense of significantly reduced piezoelectric properties. BIPT04 with a high Curie temperature has a low d_{33}. However, the value of the piezoelectric constant d_{33} can be improved by dopants, as is the case of 2.0 mol% La_2O_3-doped $0.2BiInO_3$-$0.8PbTiO_3$ ceramics with d_{33} = 12 pC/N [78] and 1.5 mol% Nb-doped $0.15BiInO_3$-$0.85PbTiO_3$ ceramics with $d_{33} \approx$ 60 pC/N, which is even higher than the d_{33} of $PbTiO_3$ of about 56 pC/N [17]. As such, one can aim in the future to explore and add suitable additives to improve the piezoelectric properties of BIPT single crystals.

Fig. 4.30 The equipment of the KCF PM-3001 Piezo d_{33} Meter.

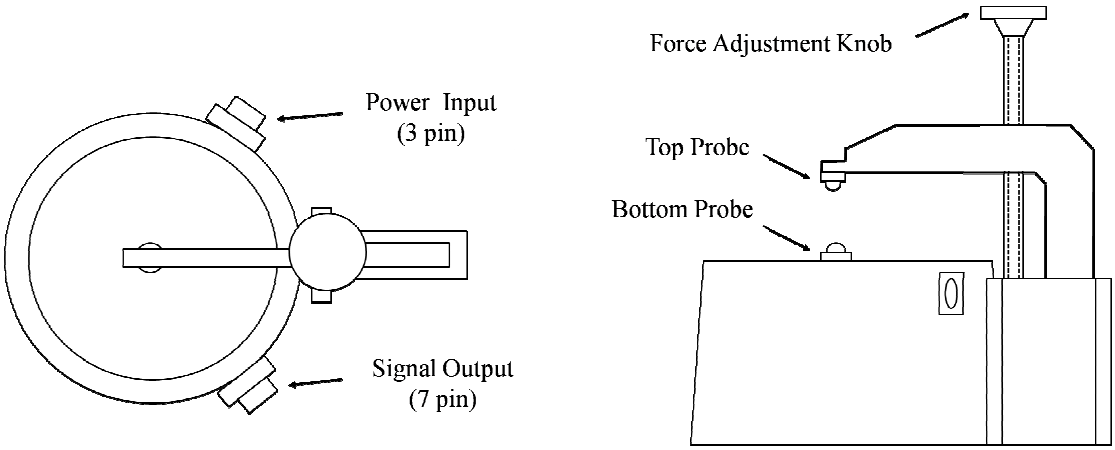

Fig. 4.31 The schematic diagram of KCF PM-3001 d_{33} Meter.[77]

4.3 Conclusion

Single crystals of $0.3BiInO_3$-$0.7PbTiO_3$, $0.4BiInO_3$-$PbTiO_3$ and $0.5BiInO_3$-$0.5PbTiO_3$ were successfully grown by the self-flux method and their structures were refined by the Rietveld method from X-ray powder diffraction data. The structural transition of $0.3BiInO_3$-$0.7PbTiO_3$ was observed by high temperature X-ray diffraction. The chemical compositions and distribution of individual elements of BIPT single crystals were studied by EDS technique and XRF spectroscopies. Ti-O and Pb-O stretching vibration modes in BIPT were observed by FTIR. The Curie temperatures of grown BIPT single crystals are 555, 556, and 557 ^{o}C, high enough for high temperature environment applications such as space exploration and automotive smart brakes. We observed that the phase transition temperature increases with increasing tetragonal distortion (c/a). According to the DSC and HT-XRD of BIPT03 results, which show a Curie temperature of 555 ^{o}C and a stable cubic structure up to 600 ^{o}C, BIPT03 undergoes a cubic to tetragonal phase transition over a wide temperature range. There is temperature hysteresis in BIPT03 crystals, which is a signature of the first order nature of the ferroelectric phase transition. The morphology of the crystallites and microstructure of BIPT were investigated by SEM and SAED. Growth striation was observed and rocking curve measurements were used to check the quality of the obtained single-crystals.

Further, we have systematically investigated the domain structures and local switching characteristics of a (010) face BIPT04 single crystals and a (110) face BIPT03 single crystals using PFM. The labyrinth domain patterns on the (010) surface of BIPT04 and on the (110) surface of BIPT03 are quite consistent with other reported relaxor ferroelectric single crystals. An analysis of the (010) face of BIPT04 at different d_c voltages suggests that domain direction tends to be consistent with the voltage direction and bias voltage can effectively control the domain orientation. The voltage orientation is important for piezoresponse. Because of polarization orientation at an angle 45° and -45° with respect to the (110) face BIPT03, there is no observable domain change up to an applied d_c voltage of 20 V. However, when a d_c voltage of -20 V is applied, domain switching occurs. For a ferroelectric material crystallizing in a specific space group, the angle of polarization orientation with respect to the single

crystal face is important for the domain reversal and this is reflected on the different d_c voltages. The measurement of piezoresponse-voltage hysteresis loops of the (010) face of BIPT04 single crystals shows that local coercive voltage is ~ 11 V without poling the sample, while local voltage is around 19 ~ 26 V after poling with ±25 V. It revealed that BIPT04 single crystals have smaller coercive voltage without poling the sample than after poling. The domain area grows with decreasing thickness and the coercive voltages decrease with decreasing thickness.

The polarization-voltage hysteresis loops, capacitance-voltage characteristics were investigated on a ferroelectric structure consisting of a platinum bottom electrode. The fatigue free behavior was observed up to 2×10^9 switching cycles at room temperature.

Finally, the piezoelectric constant d_{33} of plate of BIPT04 single crystals was measured and found to be ～ 10 pC/N.

Chapter 5

Exploring other high Curie temperature single crystals: $BiYbO_3$-$PbTiO_3$; $Bi(Sc_{0.5}, Yb_{0.5})$-$PbTiO_3$ and $BiAlO_3$-$PbTiO_3$

5.1 Crystal growth and characterization of $BiAlO_3$-$PbTiO_3$ single crystals

5.1.1 Experimental Procedure

Powder mixtures of xBiAlO$_3$-(1-x)PbTiO$_3$ with x = 0.2, 0.3, and 0.4 were prepared by grinding together Pb_3O_4, Bi_2O_3, TiO_2 and Al_2O_3 in an agate mortar. Flux materials are Pb_3O_4 and Bi_2O_3 with the ratio of 7 : 3. Then they were mixed thoroughly and were added into the alumina crucible for crystal growth in the muffle furnace. With heating rate of 120 ^{o}C/h, the temperature raised rapidly up to 1100 ^{o}C and was subsequently hold constant for 7 h to obtain a homogenous solution. The

materials cooled from 1100-750 ^oC at a rate of 1-6 ^oC/h. Then the furnace was turned off for cooling to room temperature. Only single crystals of $0.3BiAlO_3$-$0.7PbTiO_3$ (BAPT03) were successfully grown. The as-grown BAPT03 crystals were yellow in color, rectangular in shape, and almost 1mm in size, as shown in Fig. 5.1.

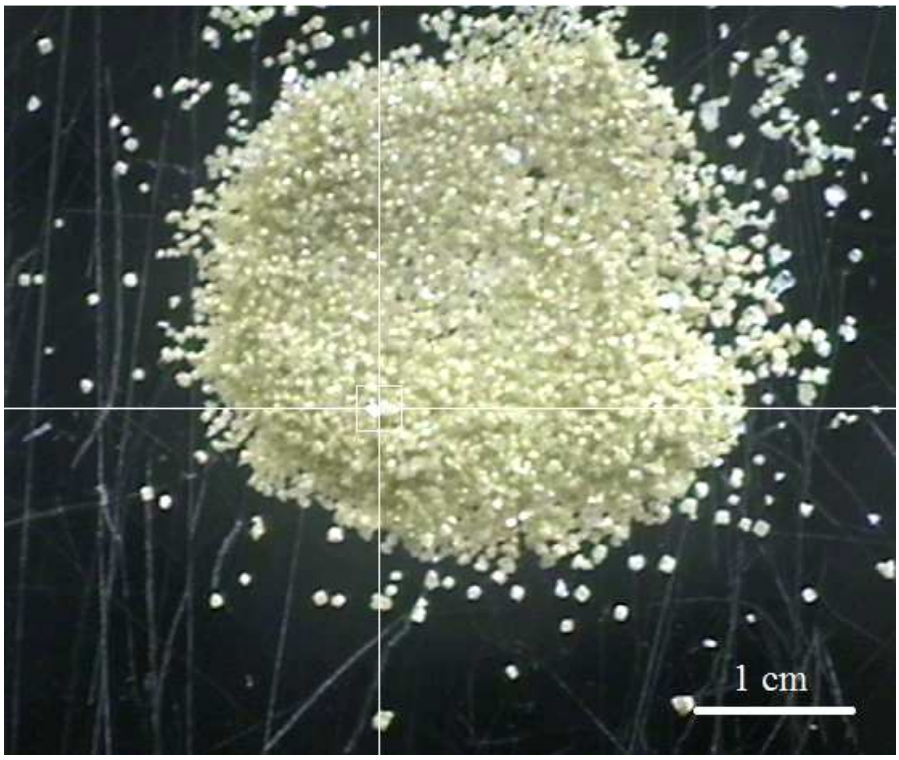

Fig. 5.1 Single crystals of $0.3BiAlO_3$-$PbTiO_3$.

Structural characterization of BAPT03 was performed on the Bruker D8 Advance X-ray diffractometer (XRD) with Cu K_α radiation in a 2θ range of 10-135° at a scanning step of 0.01^o. The XRD powder pattern was analyzed by the Rievteld method with GSAS 2000. The chemical composition of the material was verified using X-ray fluorescence spectroscopy (HITACHI, SEA6000VX-Hsfinder). Thermal properties were measured from the differential scanning calorimetry (DSC) curves, recorded on a Perkin Elmer STA 6000 under nitrogen flow in a temperature range from 50 to 800 ^oC at a heating rate of 5 ^oC/min using 17.370 mg of the sample BAPT03.

5.1.2 Results and discussion

X-ray fluorescence spectroscopy (XRF) was used to determine the chemical composition of BAPT03. Fig. 5.2(a) shows the spectrum of BAPT03 in air, while for lower energy measurement, the spectrum of BAPT03 was acquired in helium and is shown in Fig. 5.2 (b). The results show that BAPT03 single crystals contain Pb, Bi, Ti and Al elements.

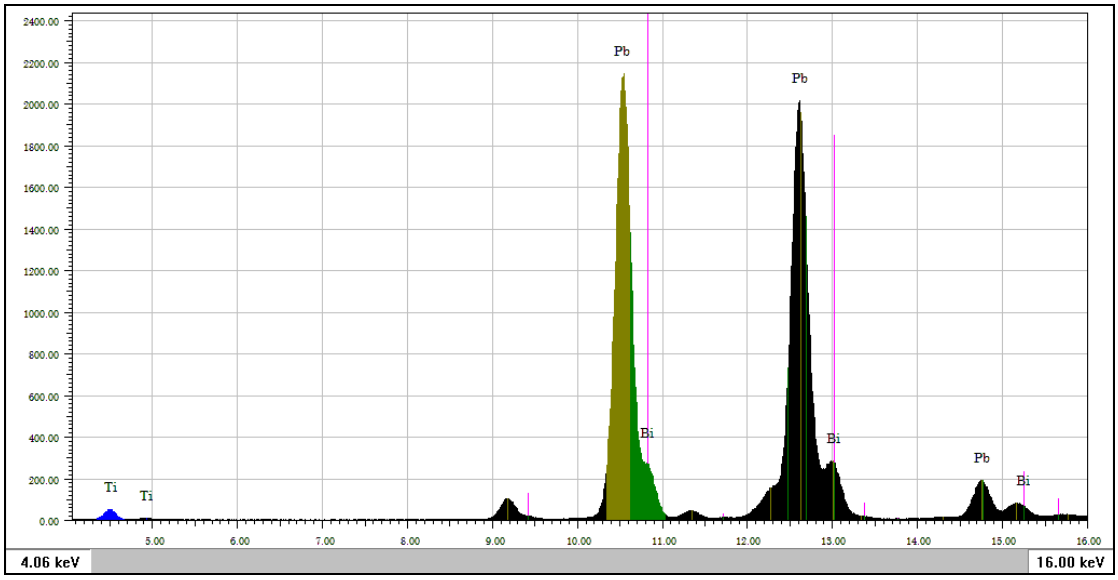

(a)

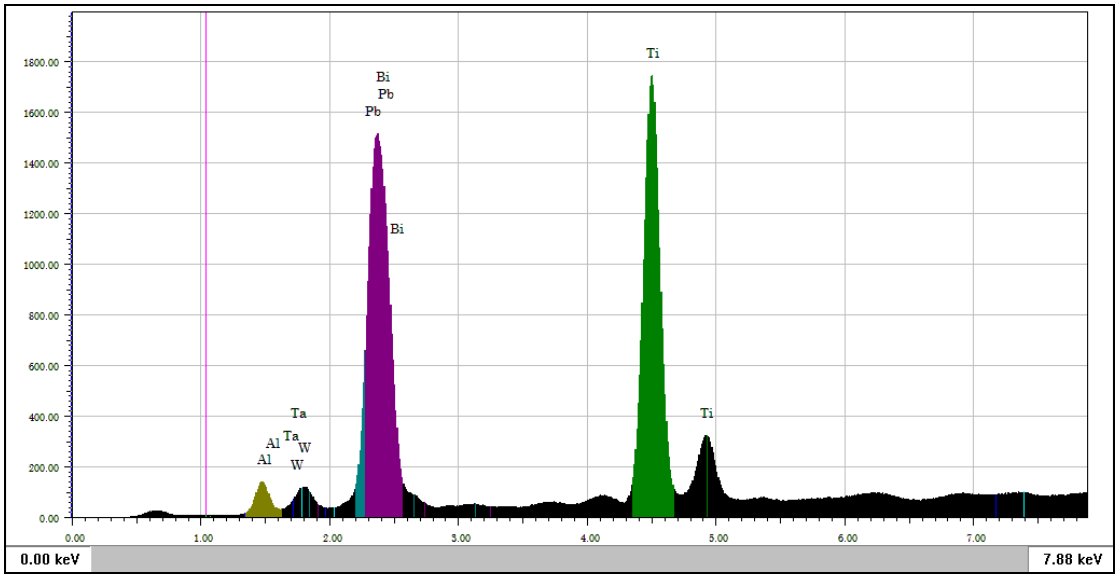

(b)

Fig. 5.2 The spectrum of BAPT03 in air (a) and in He (b) measured by XRF.

Fig. 5.3 shows the XRD pattern of BAPT03 single crystals measured at room temperature. It shows that BAPT03 single crystals have tetragonal perovskite structure with space group *P*4*mm* (No. 99) without additional detectable secondary phases. It is also observed that there is a little shift to the low-angle side in the peak positions of substituted compounds, which reflects the corresponding minor change in the structural parameters. In order to determine the structure variation of BAPT03 due to Bi^{3+} and Al^{3+} doping, the structure of BAPT03 was refined by the Rietveld method using GSAS 2000, based on the structural data of ICSD-61168. The experimental and fitted XRD patterns of BAPT03 are shown in Fig. 5.4, and the fitting residuals R_{wp} and R_p for BAPT03 are 12.80% and 9.77%. It shows that the calculated peak positions and intensities reasonably match the observed peaks. The lattice parameters are summarized in Table 5.1, while atom coordinates (x, y and z) and isotropic temperature factor U_{iso} are given in Table 5.2. As Bi^{3+} partially substitutes Pb^{2+} and Al^{3+} partially substitutes Ti^{4+}, the bond lengths and angles of BAPT03 have changed (Table 5.3). The refined structural model of BAPT03 single crystals is shown in Fig. 5.5. The deformation angle ϕ is 96.511 in BAPT03.

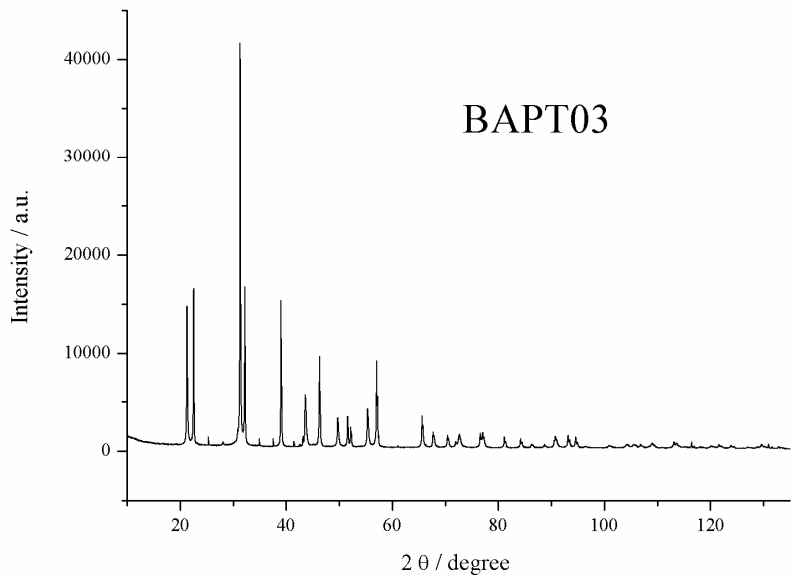

Fig. 5.3 The X-ray powder diffraction patterns of BAPT03.

Table 5.1 Lattice parameters of BAPT03

	a and *b* (Å)	*c* (Å)	*α*, *β* and *γ* (°)	Cell volume ($\times 10^6$ pm^3)	density (gm/cm^3)
BAPT03	3.904475(32)	4.12850 (6)	90	62.9390(10)	7.845

Table 5.2 Fractional coordinates (*x*, *y* and *z*), U_{iso} of all atoms of BAPT03 with space group *P*4*mm* and occupancy of atom site, obtained from Rietveld refining.

BAPT03	Atom (Wyckoff site, symmetry)	(*x*, *y*, *z*)	U_{iso}	Occupancy
R_{wp}=12.80%	Pb/Bi (1*a*, 4*mm*)	(0.0, 0.0, 0.0085)	0.02823	0.69713 /0.29721
R_p=9.77%	Ti/Al (1*b*, 4*mm*)	(0.5, 0.5, 0.55119)	0.00191	0.71325 /0.31935
	O1 (1*b*, 4*mm*)	(0.5, 0.5, 0.10043)	0.00322	1.0
	O2 (2*c*, 2*mm*)	(0.0, 0.5, 0.60515)	0.01530	1.0

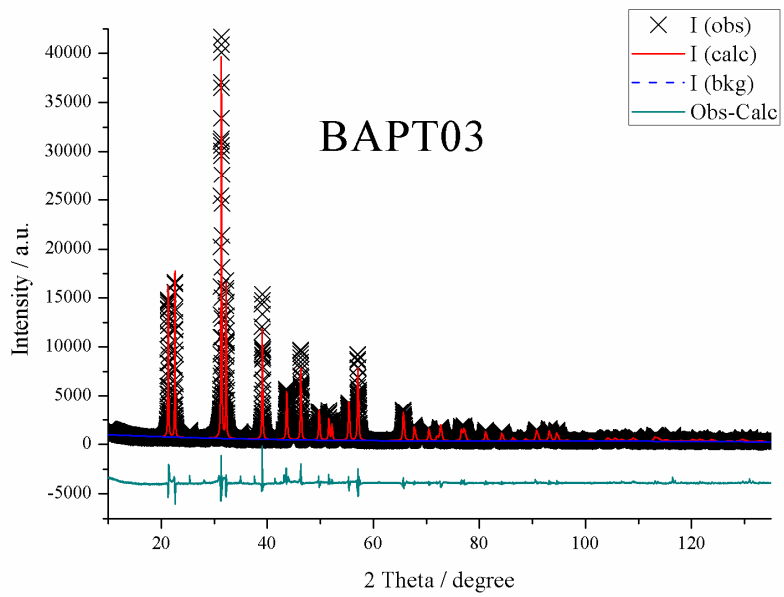

Fig. 5.4 Experimental, calculated curves of XRD of BAPT03 crystalline powder are shown by crosses and solid curves, respectively. The bottom curve is the difference between experimental and fitting values.

Table 5.3 Bond lengths and angles of framework geometry in BAPT03.

Bond Lengths		Angles(°)	
Pb/Bi-O1 (Å)	2.786840(20)	O2 – Pb/Bi - O2	99.0728(9) 65.0925(5)
Pb/Bi-O2 (Å)	2.565970(20)	O1 – Ti/Al - O2 (ϕ)	96.51070(10)
Ti/Al-O1 (Å)	1.860960(30) 2.267550(30)	O2 –Ti/Al - O2	166.97861(20) 89.2633
Ti/Al-O2 (Å)	1.964910(20)		

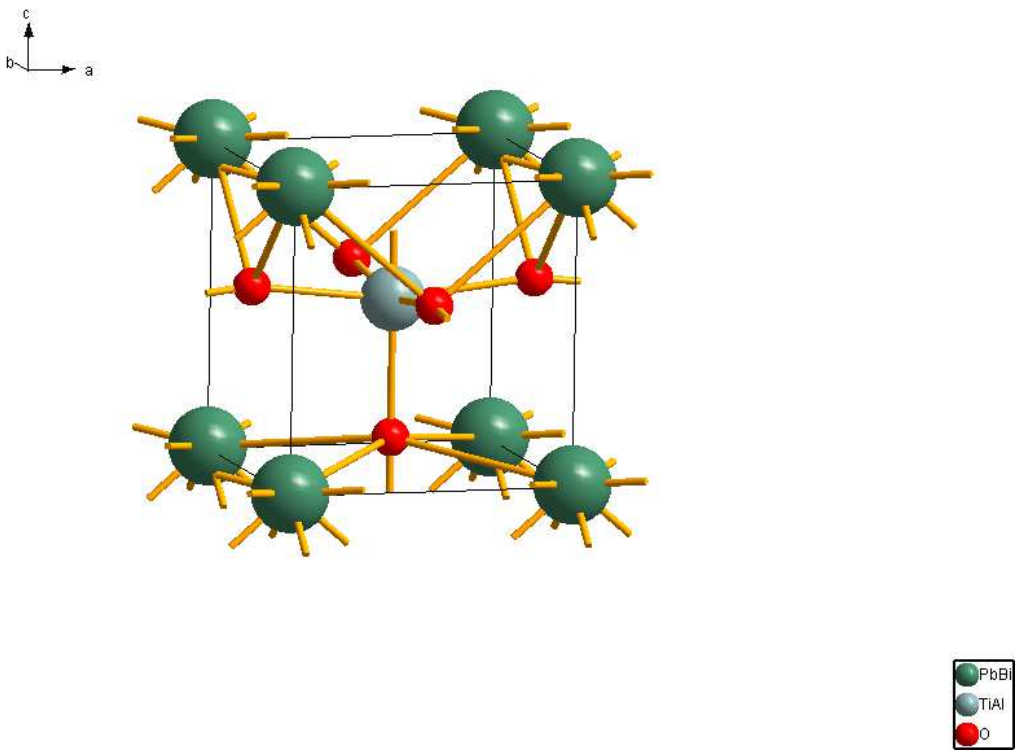

Fig. 5.5 Refined structural model of BAPT03.

Fig. 5.6 shows the temperature variations of heat flow of BAPT03 single crystals, and Fig. 5.7 shows there is no significant weight loss at high temperature. One endothermic peak was observed in the DSC curve, which is caused by the ferroelectric phase transition. The onset of endothermic peaks at 466 °C is associated

with the Curie temperature and the enthalpy change ΔH of the endothermic peak is 2.7518 J/g.

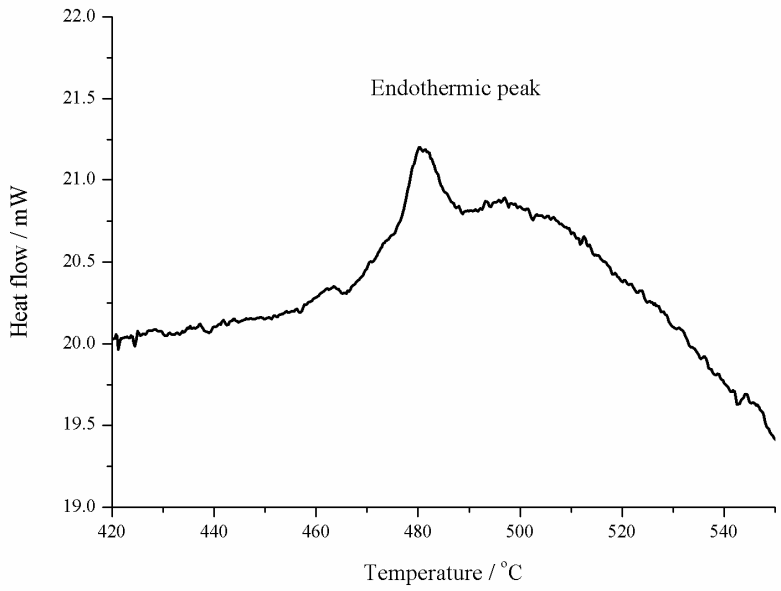

Fig. 5.6 The heat flow vs temperature (DSC trace) for BAPT03.

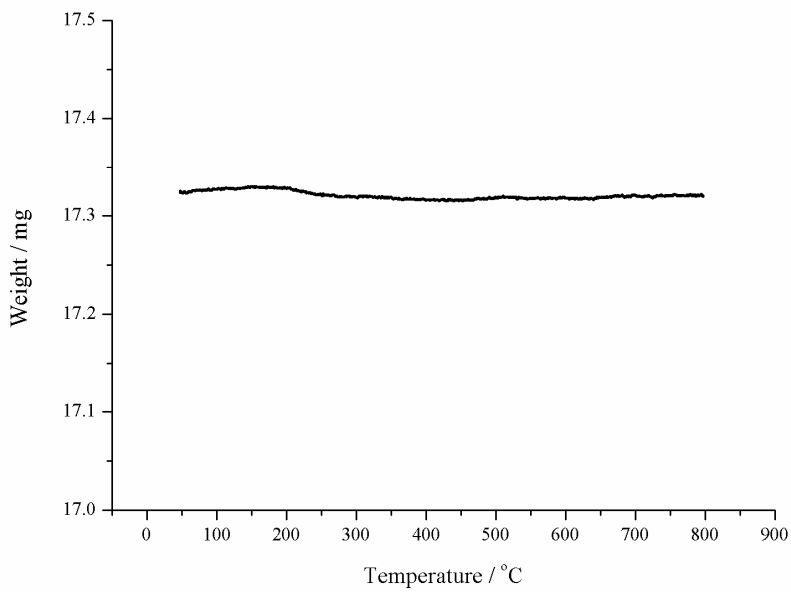

Fig. 5.7 The change of weight of BAPT03 in the heating cycle.

5.2 Attempt to grow single crystal $BiYbO_3$-$PbTiO_3$ and $Bi(Sc_{0.5}, Yb_{0.5})$-$PbTiO_3$

5.2.1 Experimental Procedure

In order to grow $0.2BiYbO_3$-$0.8PbTiO_3$ (BYPT02) single crystals, the starting materials Pb_3O_4, Bi_2O_3, Yb_2O_3, and TiO_2 were weighted according to this chemical formula, homogenized and milled in an agate mortar. To solve the problem of poor structural stability, we introduced ScO_2 as an additive into $BiYbO_3$-$PbTiO_3$ system to synthesize $Bi(Sc_{0.5},Yb_{0.5})O_3$-$PbTiO_3$ single crystals. Sc_2O_3, Bi_2O_3, TiO_2 and Yb_2O_3 were used as starting materials to obtain the $0.37Bi(Sc_{0.5}Yb_{0.5})O_3$-$0.63PbTiO_3$ (BSYPT) single crystals. Pb_3O_4 and Bi_2O_3 with suitable ratios were selected as the flux. The starting materials and flux materials were mixed and were added into the alumina crucible for crystal growth in the muffle furnace. A temperature of 1100 ^oC was maintained for 7 h to obtain a homogenous solution which was a slowly cooled from 950 to 650 ^oC at a rate of 1-6 ^oC/h. The as-grown crystals of BYPT02_1 were light yellow transparent in color, rectangular in shape, and 2 ~ 3 mm in size, shown in Fig. 5.8 (a). The as-grown crystals of BSYPT1 are shown in Fig. 5.8 (b), with light yellow color, polyhedral shape, and 1 mm in size.

The new phases were analyzed by X-ray diffraction (XRD). Structural studies of the materials were carried out using a Bruker D8 Advance X-ray diffractometer with Cu K_α radiation in a 2θ range of 10-90° with a scanning step of 0.02^o. The HITACHI, SEA6000VX-Hsfinder X-ray fluorescence spectroscopy were used to verify the chemical composition of the material. Thermal characterization was performed with a Perkin Elmer STA 6000 differential scanning calorimetry in the temperature range from 50 to 800 ^oC, under nitrogen at a flow rate of 20 ml/min. Data were collected upon heating with a constant rate of 5 ^oC/min with a sample of 11.595 mg of mass.

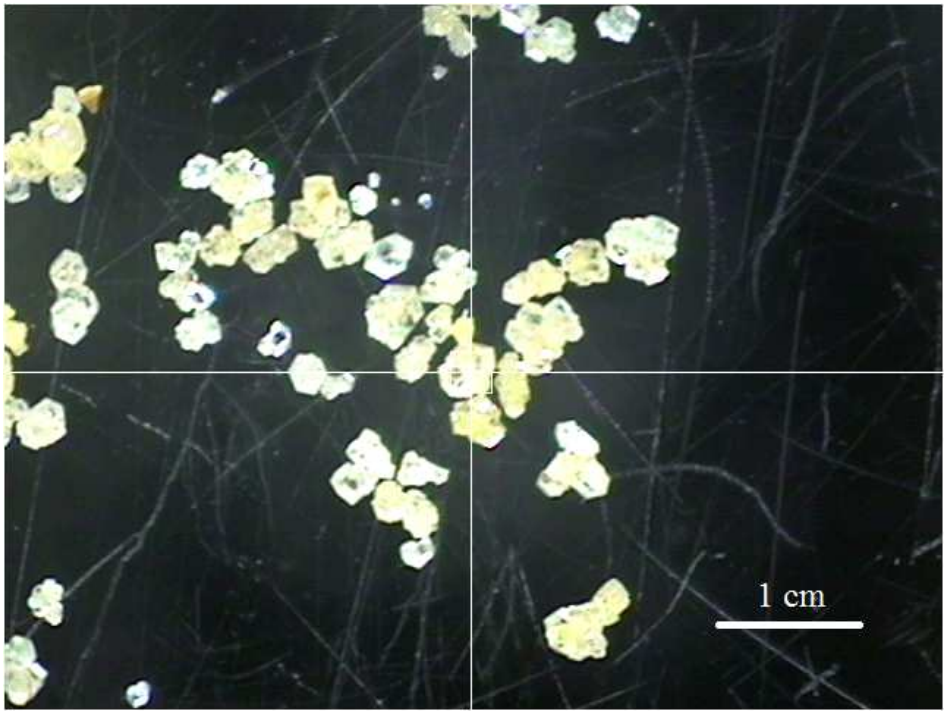

(a)

(b)

Fig. 5.8 (a) Crystals of BYPT02_1 and (b) crystals of BSYPT1 in a 1 mm grid.

5.2.2 Results and discussion

In order to determine the chemical composition of as grown single crystals of BYPT02_1, they were examined by XRF. The Fig. 5.9 (a) shows the spectrum in air, while for lower energy measurement, the spectrum was also acquired in helium and is shown in Fig. 5.9 (b). The results show that the as-grown single crystals of BYPT02_1 contain Pb, Bi, Ti and Yb elements.

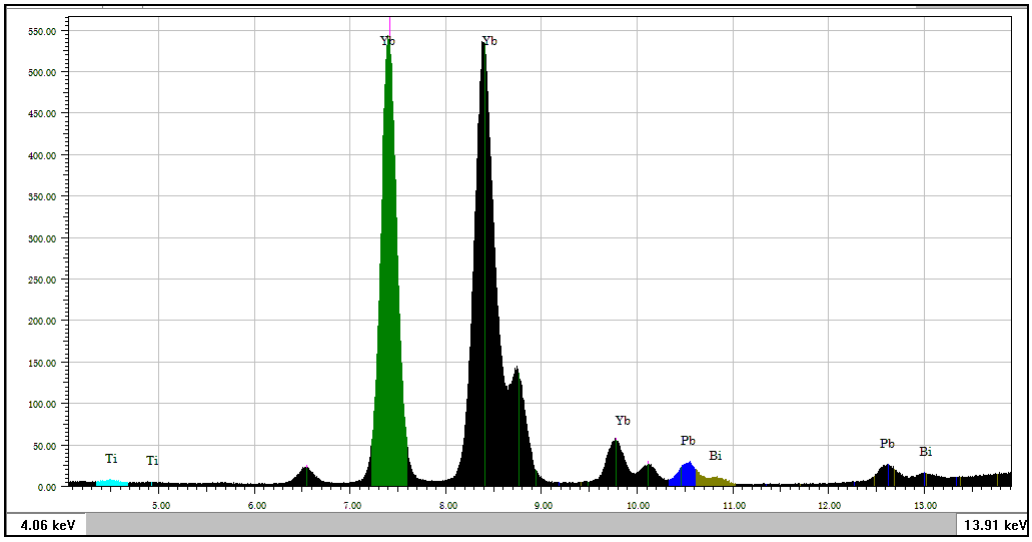

(a)

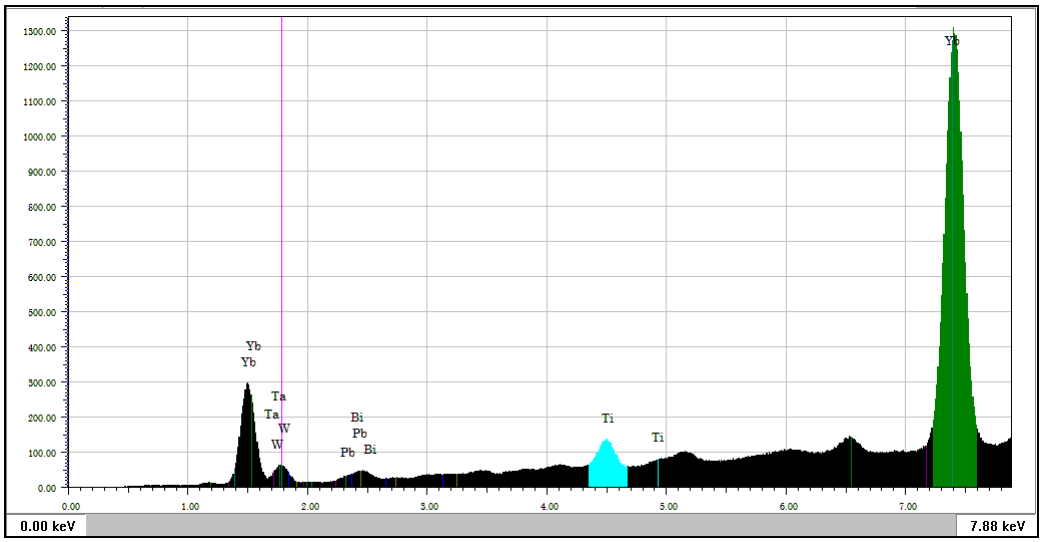

(b)

Fig. 5.9 The spectrum of BYPT02_1 in air (a) and in Helium (b) measured by XRF.

Fig. 5.10 shows the XRD pattern of as-grown of BYPT02_1, together with the possible isomorphic garnet structure of $Y_3Al_5O_{12}$. Thus, as-grown single crystals of BYPT02_1 are likely to have cubic structure (Pb_xBi_{3-x}) (Ti_yYb_{5-y}) O_{12} with space group $Ia\bar{3}d$ (space group 230). When growing the single crystals, flux materials Bi_2O_3 or Pb_3O_4 substitute the constituent elements of the desired material and crystals with the garnet structure are easier to crystallize. The XRD pattern of BSYPT1 is depicted in Fig. 5.11, showing the presence of Bi_2O_3 and of an unknown impurity phase.

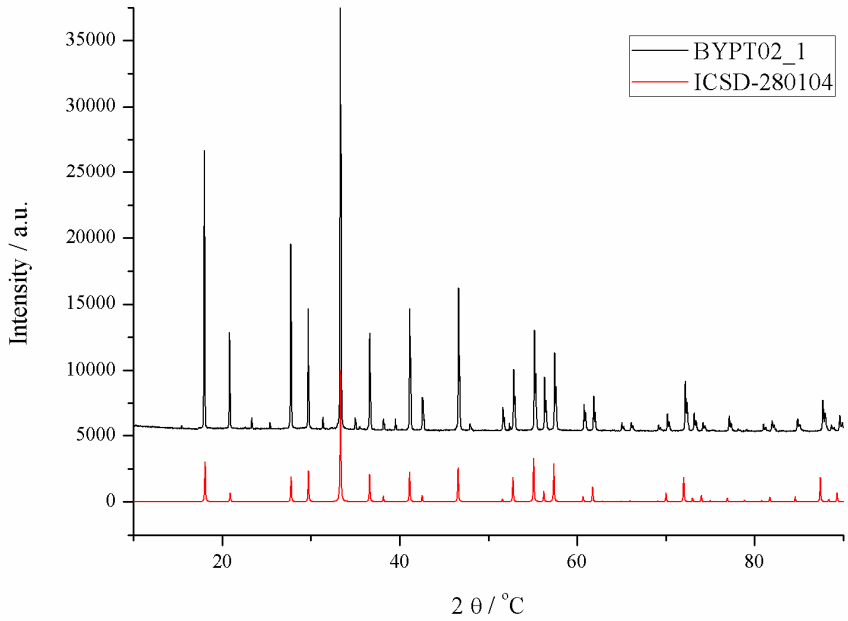

Fig. 5.10 The X-ray powder diffraction patterns of BYPT02_1 compared with the ICSD-280104 material $Y_3Al_5O_{12}$.

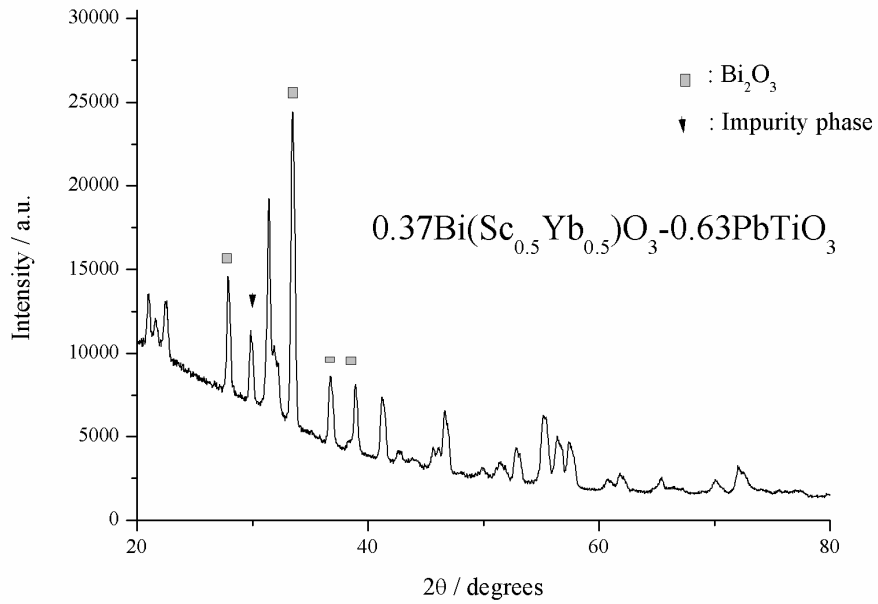

Fig. 5.11 The X-ray powder diffraction patterns of BSYPT1 materials.

5.3 Conclusion

Single crystals $0.3BiAlO_3$-$0.7PbTiO_3$ systems were successfully grown from the Pb_3O_4 and Bi_2O_3 solutions by the flux method. The chemical compositions were checked by X-ray fluorescence spectroscopy. The structure of BAPT03 single crystals with tetragonal symmetry, space group of *P*4*mm*, was determined by Rietveld refinement of X-ray powder diffraction data. The endothermic peak in the DSC curve reveals the Curie temperature at 466 ^{o}C, which is associated with the ferroelectric phase transition. Even if the Curie temperature is relatively high, the small size of the BAPT03 single crystals restricts further performance measurements and its potential application. An improvement of the growth method is needed to grow bigger single crystals.

We tried to grow single-crystals of $0.2BiYbO_3$-$0.8PbTiO_3$ and $0.37Bi(Sc_{0.5}Yb_{0.5})O_3$-$0.63PbTiO_3$, but unfortunately, the pure BYPT02 and BSYPT were not obtained. Single crystals of (Pb_xBi_{3-x}) (Ti_yYb_{5-y}) O_{12} with cubic structure and space group $Ia\bar{3}d$ (space group 230) were grown. BSYPT with an impurity phase was obtained. Due to the instability of BYPT02 materials, it is necessary to further improve the experiment conditions and optimize growth parameters for the flux crystal growth. (Pb_xBi_{3-x}) (Ti_yYb_{5-y}) O_{12} single crystals have the same structure as the yttrium aluminium garnet, and as garnets are a common host material of solid-state lasers it may also find use in solid state lasers.

Chapter 6

Conclusion

This major contribution of this dissertation was the growth of high Curie temperature single crystals of $BiInO_3$-$PbTiO_3$ and $BiAlO_3$-$PbTiO_3$ by the flux method. The physical behavior of BIPT system was studied including its structural characterization, morphology of the crystallites and microstructure, thermodynamics, domain structures and local switching characteristics.

The structure of the single crystals of BIPT with the tetragonal perovskite structure and space group *P*4*mm*, was confirmed by Rietveld refinement of XRD data. The analysis of the doping effect was made based on hybridization between the oxygen 2*p* state and the electronic states of cations. Ti-O and Pb-O stretching vibration modes in BIPT were observed by FTIR. The high Curie temperature of BIPT single crystals above 550 ^{o}C was confirmed, a value suitable for high temperature applications such as space exploration and automotive smart brakes. There is temperature hysteresis in the BIPT03 crystals, which is indicative of occurrence of a first order ferroelectric phase transition. The phase transition temperature increased with the increase of the tetragonal distortion (*c*/*a*). The morphology and microstructure of BIPT were investigated from SEM and SAED. Growth striation was observed and rocking curve measurements were used to check the single crystals quality.

The domain structures and local switching characteristics of BIPT04 single crystals with (010) orientation and BIPT03 single crystals with (110) orientation were investigated in detail. The labyrinth domain patterns on the (010) surface of BIPT04 single crystals and the (110) surface of BIPT03 single crystals were observed similarly to other reported relaxor ferroelectric single crystals. An analysis of (010)

face BIPT04 single crystals at different d_c voltages suggests that domain direction tends to comply with the direction of the applied field and bias voltage can effectively control the domain orientation. Comparing with an analysis of the (110) face BIPT03 single crystals, the angle of polarization orientation and respect to the single crystal face is important for the domain reversal at different d_c voltages. The measurement of piezoresponse-voltage hysteresis loops on the (110) face of single crystals before and after poling the sample shows that the coercive voltage is smaller before poling the sample than after poling. The domain area grows with the decreasing thickness and the coercive voltages get smaller with decreasing thickness.

The polarization-voltage hysteresis loops and capacitance-voltage characteristics were investigated; a fatigue free behaviour was observed up to 2×10^9 switching cycles at room temperature. The piezoelectric constant d_{33} was measured on a plate of BIPT04 single crystals and found to be ~ 10 pC/N.

Single crystals of BAPT03 with Curie temperature of 466 ^oC were also successfully grown from the Pb_3O_4 and Bi_2O_3 solutions by the flux method and their structure has tetragonal symmetry with space group of *P*4*mm*, determined by the Rietveld refinement of X-ray powder diffraction data. However, BAPT03 single crystals were very small and no further characterization was pursued. Further development of the growth method is needed.

The $0.2BiYbO_3$-$0.8PbTiO_3$ and $0.37Bi(Sc_{0.5}Yb_{0.5})O_3$-$0.63PbTiO_3$ single crystals could not be obtained. Single crystals of (Pb_xBi_{3-x}) (Ti_yYb_{5-y}) O_{12} with cubic structure and space group $Ia\bar{3}d$ were grown and BSYPT with an impurity phase was obtained.

Bibliography

[1] Seung-Eek Park and Thomas R. Shrout, *Ultrahigh strain and piezoelectric behavior in relaxor based ferroelectric single crystals*, J. Appl. Phys. **82** (1997) 1804.

[2] R. C. Turner, P. A. Fuierer, R. E. Newnham and T.R. Shrout, *Materials for high temperature acoustic and vibration sensors: A review*, Appl. Acoust. **41** (1994) 299.

[3] Richard E. Eiter, Clive A. Randall, Thomas R. Shrout, Paul W. Rehrig, Wes Hackenbrger and Seung-Eek Park, *New High Temperature Morphotropic Phase Boundary Piezoelectrics Based on Bi(Me)O_3 –$PbTiO_3$ Ceramics*, Jpn. J. Appl. Phys. **40** (2001) 5999.

[4] R Eitel, S J Zhang, T R Shrout, C A Randall, I Levin, *Phase Diagram of the Perovskite System (1-x)$BiScO_3$-x$PbTiO_3$*, J.Appl. Phy. **96** (2004) 2828.

[5] C A Randall, R Eitel, T R Shrout, D I Woodward and I M Reaney, *Transmission Electron Microscopy Investigation of the High Temperature $BiScO_3$-$PbTiO_3$ Piezoelectric Ceramic System*, J.Appl. Phys. **93** (2003) 9271.

[6] V Porokhonskyy, S Kamba, A Pashkin, M Savinov and J. Perzelt, *Broadband Dielectric Spectroscopy of (1-x)$BiScO_3$-x$PbTiO_3$ Piezoelectrics*, Appl. Phys. Lett. **83** (2003) 1605.

[7] Y Feng, Z Xu, Z R Li, X Yao, *High Temperature Piezoelectric Ceramics (1-x)$BiScO_3$-x$PbTiO_3$ Near the Morphotropic Phase Boundary*, J. Inorg. Mater. **21** (2006) 1127.

[8] S J Zhang, C A Randall, T R Shrout, *Characterization of Perovskite Piezoelectric Single Crystals of 0.43$BiScO_3$-0.57$PbTiO_3$ with High Curie Temperature*, J. Appl. Phy. **95** (2004) 4291.

[9] Jun Chen, Xiaoli Tan, Wook Jo, and Jürgen Gödel, *Temperature dependence of piezoelectric properties of high-Tc* $Bi(Mg_{1/2}Ti_{1/2})O_3$*-*$PbTiO_3$, J. Appl. Phys. **106** (2009) 034109.

[10] Guanghe Wu, Hong Zhou, Xiaoye Zhou, Ni Qin, and Dinghua Bao, *Strucatral, dielectric and ferroelectric properties of* $BiAlO_3$*-*$PbTiO_3$ *solid solution thin films on indium tin oxide-coated glass substrates*, J. Am. Ceram. Soc. **93** (2010) 925.

[11] Runrun Duan, Robert F. Speyer, Edward Albera, and Thomas R. shrout, *High Curie temperature perovskite* $BiInO_3$*–*$PbTiO_3$ *ceramics*, J. Mater.Res. **19**, (2004) 2185.

[12] Gao Feng, Hong Rongzi, Liu Jiaji, Li Zhen, Cheng Lihong, and Tian Changsheng, *Phase formation and characterization of high Curie temperature x* $BiYbO_3$*-(1-x)* $PbTiO_3$ *piezoelectric ceramics*, Journal of the European Ceramic Society **29** (2009) 1687.

[13] Joel Zylberberg, Alexei A. Belik, Eiji Takayama-Muromachi, and Zuo-Guang Ye, *Bismuth Aluminate: A new high-Tc lead-free piezo-/ferroelectric*, Chem. Mater. **19** (2007) 6385.

[14] Rajeev Ranjan, Ajay Kumar kalyani, Rohini Garg, and P.S.R.Krishna, *Structure and phase transition of the (1-x)*$PbTiO_3$*-(x)*$BiAlO_3$ *system*, Solid state communications **149** (2009) 2098.

[15] Guanghe Wu, Hong Zhou, Xiaoye Zhou, Ni Qin, and Dinghua Bao, *Structural, dielectric and ferroelectric properties of* $BiAlO_3$*-*$PbTiO_3$ *solid solution thin films on indium tin oxide-coated glass substrates*, J. Am. Ceram. Soc. **93** (2010) 925.

[16] Alexei A. Belik, Sergey Yu Stefanovich, Bogdan I. Lazoryak, and Eiji Takayama-Muromachi, **$BiInO_3$*: A Polar Oxide with* $GdFeO_3$*-Type Perovskite Structure*, Chem. Mater. **18** (2006) 1964.

[17] Shujun Zhang, Ru Xia, Clive A. Randall, Thomas R. Shrout, Runrun Duan and Robert F. Speyer, *Dielectric and Piezoelectric Properties of Niobium-modified $BiInO_3$–$PbTiO_3$ Perovskite Ceramics with High Curie Temperatures*, J. Mater. Res. **20** (2005) 2067.

[18] S. W. Ko, H. G. Yeo, and S. Trolier-McKinstry, *Growth and properties of chemical solution deposited $BiInO_3$–$PbTiO_3$ films*, Appl. Phys. Lett. **95** (2009) 162901.

[19] Gao Feng, Hong Rongzi, Liu Jiaji, Li Zhen, Cheng Lihong, and Tian Changsheng, *Phase structure and piezoelectric properties of high Curie temperature $BiYbO_3$-$PbTiO_3$-$BaTiO_3$ ceramics*, Journal of Alloys and Compounds **475** (2009) 619.

[20] I. Grinberg, M. R. Suchomel, and P. K. Davies, *Predicting morphotropic phase boundary locations and transition temperatures in Pb- and Bi-based perovskite solid solutions from crystal chemical data and first-principles calculations*, J. Appl. Phys. **98** (2005) 094111.

[21] Shujun Zhang, Clive A. Randall. and Thomas R. Shrout, *High Curie temperature piezocrystals in the $BiScO_3$-$PbTiO_3$ perovskite system*, Applied Physics Letters, **83** (2003) 3150.

[22] Vera V. Daniel, *Dielectric Relaxation*. Academic Press, London and New York (1967) pp234.

[23] ANSI/IEEE, IEEE standard on piezoelectricity. IEEE Standard 176-1987 (1987).

[24] S. O. Reza Moheimani and Andrew J. Fleming, *Piezoelectric Transducers for vibration control and damping*, Springer-Verlag London Limited (2006) pp13.

[25] Dahiya Ravinder S., Maurizio Valle, *Robotic tactile sensing*, Springer Netherlands (2013) pp204

[26] Walter Heywang, Karl Lubitz and Wolfram Wersing, *Piezoelectricity*, Springer

(2008) pp 37.

[27] Perambur S. Neelakanta, *Handbook of electromagnetic materials: monolithic and composite versions and their applications*, CRC Press (1995) pp292.

[28] H. Megaw, *Crystal structure of barium titanium oxide and other double oxides of the perovskite type*, Trans. Faraday Soc. **42** (1946) A224.

[29] P.M.Woodward, *Octahedral Tilting in Perovskites. I. Geometrical Considerations*, Acta Crystallographica B **53** (1997) 32.

[30] V. M. Goldschmidt: Shrifter Norske Videnskop-Adad. Oslo: Matermot. Naturuid Klasse (Nov.1926).

[31] R. D. Shannon, *Revised effective ionic radii and systematic studies of interatomic distances in halides and chalcogenides*, Acta Cryst. **A32** (1976) 751.

[32] J. Rodel, W. Jo, K.T.P. Seifert, E. Anton, T. Granzow and D. Damjanovic, *Perspective on the development of lead-free piezoceramics*, J. Am. Ceram. Soc. **92** (2009) 1153.

[33] Matthew R. Suchomel and Peter K. Davies, *Predicting the position of the morphotropic phase boundary in high temperature* $PbTiO_3$*-Bi(B'B")*O_3 *based dielectric ceramics*, J. Appl. Phys. **96** (2004) 4405.

[34] S.M. Gupta and D. Viehland, *Tetragonal to rhombohedral transformation in the lead zirconium titanate lead magnesium niobate lead titanate crystalline solution*, J. Appl. Phys. **83**,(1998) 407.

[35] M. E. Lines, A. M. Glass, *Principles and applications of ferroelectrics and related materials*, Clarendon press Oxford (1977) pp71.

[36] Govindhan Dhanarai, Kullaiah Byrappa, Visshwanath Prasad, Michael Dudley, *Handbook of crystal growth*, Springer Heidelberg Dordrecht London New York (2010) pp 567.

[37] Safa Kasap, Peter Capper, *Handbook of electronic and photonic materials*, Springer Science+Business Media, Inc. (2006) pp 238.

[38] Govindhan Dhanarai, Kullaiah Byrappa, Visshwanath Prasad, Michael Dudley, *Handbook of crystal growth*, Springer Heidelberg Dordrecht London New York (2010) pp 4.

[39] D. Elwell and H. J. Scheel, *Crystal Growth from High-Temperature Solutions*, Academic Press, London and New York (1975) pp 279.

[40] D. F. Bliss, *Evolution and Application of the Kyropoulos Crystal Growth Method*, in: R.S.Feigelson (Ed.), *50 Years Progress in Crystal Growth: A Reprint Collection*, Elserver. B.V,Amsterdam (2004).

[41] D. Elwell and H. J. Scheel, *Crystal Growth from High-Temperature Solutions*, Academic Press, London and New York (1975) pp 294

[42] Skoog, D.A., Holler, F.J., Crouch, S.R., *Principles of Instrumental Analysis, Six edition*, Thomson Brooks/Cole, USA (2007) pp309.

[43] T. Hatakeyama and F.X. Quinn, *Thermal Analysis: Fundamentals and Applications to Polymer Science*, 2nd Edition, Wiley, Chichester, (1999) pp1.

[44] Höhne, G. W. H., Hemm inger, W. F. Flammersheim, H. J., *Differential Scanning Calorimetry*, Springer Verlag Heidelberg, New York. (2003) pp1.

[45] Pungor, Erno, *A Practical Guide to Instrumental Analysis*, Florida: Boca Raton. (1995) pp181.

[46] Myer Kutz, *Handbook of materials selection*, John Wiley & Sons, Inc. (2001) pp607.

[47] Peter R. Griffiths, James A. de Haseth, *Fourier transform infrared spectrometry, Second edition*, John Wiley & Sons, Inc. (2007) pp19.

[48] Barbara Stuart, *Infrared spectroscopy: Fundamentals and applications*, John

Wiley & Sons, Ltd (2004) pp23.

[49] C. T. K.-H. Stadtländer, *Scanning electron microscopy and transmission electron microscopy of mollicutes: challenges and opportunities*, in 'Modern Research and Educational Topics in Microscopy' (2007) pp122.

[50] Nelson Durán, Silvia S. Guterres, Oswaldo L. Alves, *Nanotoxicology: Materials, methodologies, and assessments*, Springer New York Heidelberg Dordrecht London (2004) pp37.

[51] David B. Williams, C. Barry Carter, *Transmission electron microscopy: A textbook for materials science*, Springer (2009) pp7.

[52] Ludwig Reimer, *Transmission electron microscopy*, Spring-Verlag Berlin Heidelberg GnbH (1984) pp3.

[53] Weilie Zhou and Zhong Lin Wang, *Scanning microscopy for nanotechnology: Techniques and applications*, Springer-Verlag New York (2007) pp1.

[54] Gerhard Dehm, James M. Howe and Josef Zweck, *In-situ electron microscopy: Applications in physics, chemistry and materials science*, Wiley-VCH Verlag GmbH & Co. KGaA (2012) pp5.

[55] KD Vernon-Parry, AC Wright, *TEM: An introduction – part 2*, III-Vs Review, 14 (2001) 48.

[56] Ludwig Reimer, *Transmission electron microscopy*, Spring-Verlag Berlin Heidelberg GnbH (1984) pp3.

[57] Nan Yao, Zhong Lin Wang, *Handbook of microscopy for nanotechnology*, Kluwer Academic Publishers (2005) pp569.

[58] John J Bozzola, "*Electron microscopy*" in: Encyclopedia of life science, John Wiley & Sons, Ltd (2002).

[59] Sergei V Kalinin, Anna N Morozovska, Long Qing Chen and Brian J Rodriguez,

Local polarization dynamics in ferroelectric materials, Rep. Prog. Phys. **73** (2010) 056502.

[60] P. Güthner and K. Dransfeld, *Local poling of ferroelectric polymers by scanning force microscopy*, Appl. Phys. Lett. **61** (1992) 1137.

[61] Sergei V. Kalinin, Edgar Karapetian and Mark Kachanov, *Nanoelectromechanics of piezoresponse force microscopy*, Physical review B **70** (2004) 184101.

[62] I. K. Bdikin, V.V. Shvartsman, and A. L. Kholkin, *Nanoscale domains and local piezoelectric hysteresis in* $Pb(Zn_{1/3}Nb_{2/3})O_3$*-4.5%*$PbTiO_3$ *single crystals*, Applied Physics Letters **83** (2003) 4232.

[63] H. R. Zeng, K. Shimamura, E. A. G. Villora, S. Takekawa, K. Kitamura, J. Y. Xu and Q. R. Yin, *Piezoresponse imaging and local characterization of ferroelectric domains in* $Pb(Zn_{1/3}Nb_{2/3})O_3$*-7%*$PbTiO_3$ *single crystals*, Physica status solidi (RRL) – Rapid Research Letters **1** (2007) R62.

[64] Qian Li, Yun Liu, Ray L. Withers, Yuhui Wan, Zhenrong Li and Zhuo Xu, *Piezoresponse force microscopy studies on the domain structures and local switching behavior of* $Pb(In_{1/2}Nb_{1/2})O_3$*-*$Pb(Mg_{1/3}Nb_{2/3})O_3$*-*$PbTiO_3$ *single crystals*, Journal of Applied Physics **112** (2012) 052006.

[65] Elisabeth Soergel, *Piezoresponse force microscopy (PFM)*, J. Phys. D: Appl. Phys. **44** (2011) 464003.

[66] Jungk T, Hoffmann Á and Soergel E, *Contrast mechanisms for the detection of ferroelectric domains with scanning force microscopy*, New J. Phys. **11** (2009) 033029.

[67] A.C. Larson, R.B. Von Dreele, General Structure Analysis System (GSAS), Los Alamos National Laboratory Report LAUR 86-748, 2004.

[68] R.J. Nelmes and W.F. Kuhs, *The crystal structure of tetragonal* $PbTiO_3$ *at room*

temperature and at 700 K, Solid State Communications **54** (1985) 721.

[69] J. G. Bergman, G. R. Crane, and E. H. Turner, *The tetragonal deformation of the TiO_6 octahedron in ferroelectric $PbTiO_3$*, Journal of solid state chemistry **21** (1977) 127.

[70] Ronald E. Cohen, *Origin of ferroelectricity in perovskite oxides*, Nature **358** (1992) 136.

[71] J. T. Last, *Infrared-absorption studies on barium titanate and related materials*, Phy. Rev. **105** (1957) 1740.

[72] Chunlei Wang, Ferroelectrics, "*Theories and Methods of First Order Ferroelectric Phase transitions*", Chapter 16 (2010) pp275.

[73] Weilie Zhong, *Ferroelectric physics*, Science Press, Beijing (1996) pp 78.

[74] Nai-Ben Ming, Jing-Fen Hong and Duan Feng, *The growth striations and ferroelectric domain structures in Czochralski-grown $LiNbO_3$ single crystals*, Journal of Materials Science **17** (1982) 1663.

[75] T Jungk, Á Hoffmann and E Doergel, *Impact of the tip radius on the lateral resolution in piezoresponse force microscopy*, New journal of physics **10** (2008) 013019.

[76] P. Heremans, G. H. Gelinck, R. Müller, K.-J. Baeg, D.-Y.Kin, Y.-Y. Noh, *Polymer and Organic Nonvolatile Memory Devices*, Chem. Mater. **23** (2011) 341.

[77] KCF Technologies, Inc., Piezo d_{33} Meter (PM-3001): User manual.

[78] Zhaofeng Li, *Phase structure and electrical properties of La_2O_3-doped $BiInO_3$-$PbTiO_3$ ceramics with high Curie temperature*, Journal of Wuhan University of Technology-mater. Sci. Ed., **23** (2008) 859.